iScience

CellPress
OPEN ACCESS

Article

Trans-omic analysis reveals obesity-associated dysregulation of inter-organ metabolic cycles between the liver and skeletal muscle

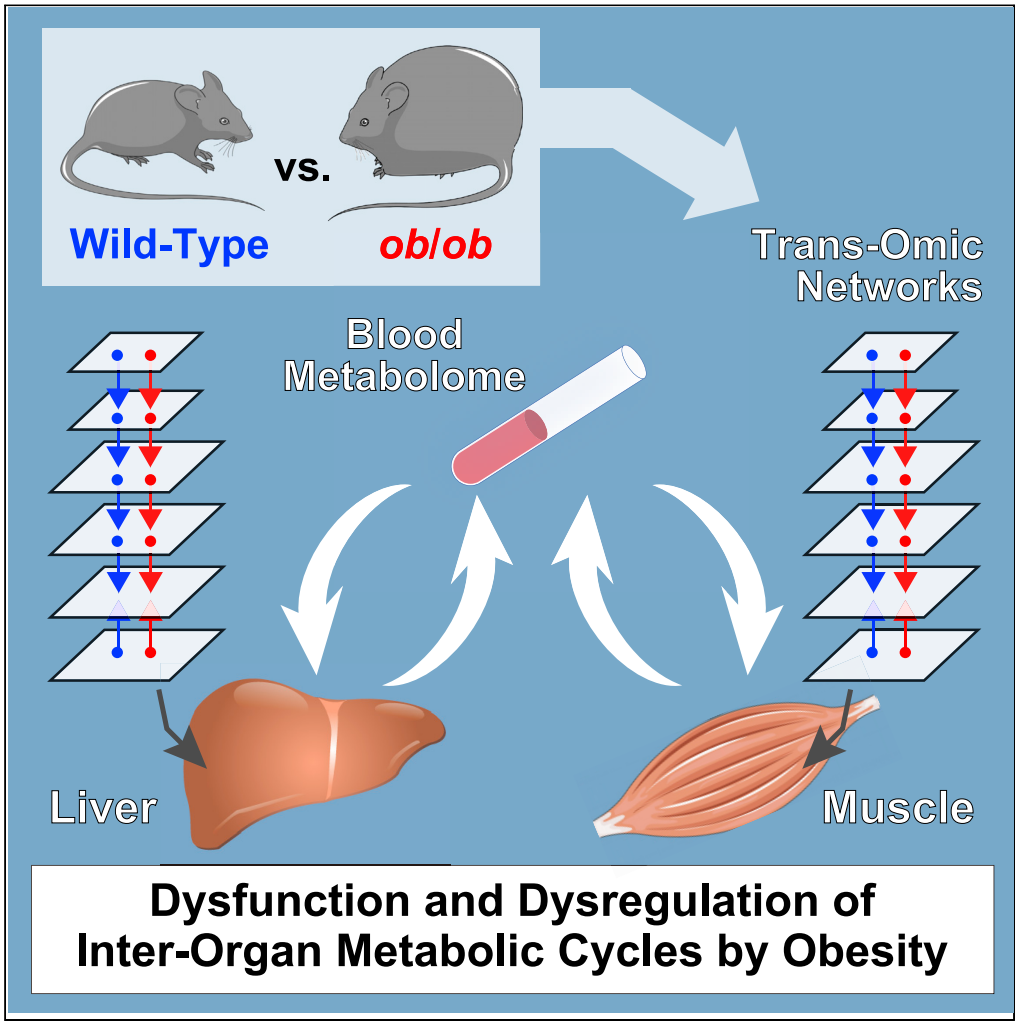

Riku Egami, Toshiya Kokaji, Atsushi Hatano, ..., Akiyoshi Hirayama, Tomoyoshi Soga, Shinya Kuroda

skuroda@bs.s.u-tokyo.ac.jp

HIGHLIGHTS

Multi-omic data in liver and skeletal muscle of WT and *ob/ob* mice were measured

We developed the trans-omic network of differentially regulated metabolic reactions

Dysregulation of inter-organ metabolic cycles associated with obesity was revealed

Egami et al., iScience *24*, 102217
March 19, 2021
https://doi.org/10.1016/j.isci.2021.102217

iScience

CellPress
OPEN ACCESS

Article

Trans-omic analysis reveals obesity-associated dysregulation of inter-organ metabolic cycles between the liver and skeletal muscle

Riku Egami,[1,16] Toshiya Kokaji,[2,16] Atsushi Hatano,[2,3,4,16] Katsuyuki Yugi,[2,3,5,6] Miki Eto,[2] Keigo Morita,[2] Satoshi Ohno,[2,7] Masashi Fujii,[2,7,8] Ken-ichi Hironaka,[2] Saori Uematsu,[1] Akira Terakawa,[2] Yunfan Bai,[1] Yifei Pan,[1] Takaho Tsuchiya,[9,10] Haruka Ozaki,[9,10] Hiroshi Inoue,[11] Shinsuke Uda,[12] Hiroyuki Kubota,[12] Yutaka Suzuki,[1] Masaki Matsumoto,[4] Keiichi I. Nakayama,[13] Akiyoshi Hirayama,[14] Tomoyoshi Soga,[14] and Shinya Kuroda[1,2,15,17,*]

SUMMARY

Systemic metabolic homeostasis is regulated by inter-organ metabolic cycles involving multiple organs. Obesity impairs inter-organ metabolic cycles, resulting in metabolic diseases. The systemic landscape of dysregulated inter-organ metabolic cycles in obesity has yet to be explored. Here, we measured the transcriptome, proteome, and metabolome in the liver and skeletal muscle and the metabolome in blood of fasted wild-type and leptin-deficient obese (*ob/ob*) mice, identifying components with differential abundance and differential regulation in *ob/ob* mice. By constructing and evaluating the trans-omic network controlling the differences in metabolic reactions between fasted wild-type and *ob/ob* mice, we provided potential mechanisms of the obesity-associated dysfunctions of metabolic cycles between liver and skeletal muscle involving glucose-alanine, glucose-lactate, and ketone bodies. Our study revealed obesity-associated systemic pathological mechanisms of dysfunction of inter-organ metabolic cycles.

INTRODUCTION

Systemic metabolic homeostasis is regulated not only by metabolism in each organ alone but also by inter-organ metabolic cycles, such as those between the liver and skeletal muscle, in mammals (Castillo-Armengol et al., 2019; Gancheva et al., 2018). Various metabolites produced by these organs are released into the circulation and affect the metabolism of other organs. Especially, during the fasting period, glucose and ketone bodies generated in the liver serve as essential energy sources for extrahepatic organs (Lehninger et al., 2005). On the other hand, lactate and alanine from the extrahepatic organs, like the skeletal muscle, work as substrates of glucose generation (gluconeogenesis) in the liver, which are known as Cori's cycle and glucose-alanine cycle, respectively (Cori and Cori, 1929; Felig, 1973). However, the detailed regulatory mechanisms controlling these inter-organ metabolic cycles are not fully understood.

Obesity impairs metabolic regulation of multiple organs, including the liver and skeletal muscle, leading to the dysfunction of the inter-organ metabolic cycle and subsequently to metabolic disorders, such as type 2 diabetes mellitus (Gancheva et al., 2018; Samuel and Shulman, 2016). Obesity perturbs metabolic regulation through changes in hormones, metabolites, and metabolic enzymes in the liver and skeletal muscle, leading to systemic metabolic dysfunction. Insulin resistance that is associated with obesity represents a well-characterized factor contributing to metabolic dysfunction (Kahn et al., 2006; Roden and Shulman, 2019); however, the effect of obesity on inter-organ metabolic cycles—the glucose-alanine cycle, the glucose-lactate cycle, and ketone body metabolism—have yet to be explored.

The metabolic network is complex, involving many diverse substrates, products, and intermediates in the chemical reactions of metabolism, denoted here as metabolic reactions, and the metabolic enzymes that mediate the reactions. Many metabolic enzymes are regulated not only through availability of substrates but also through feedback regulation by the products or through allosteric mechanisms. In addition, metabolic enzymes are regulated at the level of gene expression and through posttranslational modifications. Thus, obesity-associated dysregulation of metabolic networks in various organs is due to changes in

[1]Department of Computational Biology and Medical Sciences, Graduate School of Frontier Sciences, University of Tokyo, 5-1-5 Kashiwanoha, Kashiwa, Chiba 277-8562, Japan

[2]Department of Biological Sciences, Graduate School of Science, University of Tokyo, 7-3-1 Hongo, Bunkyo-ku, Tokyo 113-0033, Japan

[3]Laboratory for Integrated Cellular Systems, RIKEN Center for Integrative Medical Sciences, 1-7-22 Suehiro-cho, Tsurumi-ku, Yokohama, Kanagawa 230-0045, Japan

[4]Department of Omics and Systems Biology, Graduate School of Medical and Dental Sciences, Niigata University, 757 Ichibancho, Asahimachi-dori, Chuo-ku, Niigata City, Niigata 951-8510, Japan

[5]Institute for Advanced Biosciences, Keio University, Fujisawa, 252-8520, Japan

[6]PRESTO, Japan Science and Technology Agency, 1-7-22 Suehiro-cho, Tsurumi-ku, Yokohama, Kanagawa 230-0045, Japan

[7]Molecular Genetics Research Laboratory, Graduate School of Science, University of Tokyo, 7-3-1 Hongo, Bunkyo-ku, Tokyo 113-0033, Japan

[8]Department of Mathematical and Life Sciences, Graduate School of Integrated Sciences for Life, Hiroshima University, 1-3-1 Kagamiyama, Higashi-hiroshima City, Hiroshima, 739-8526, Japan

[9]Bioinformatics Laboratory, Faculty of Medicine, University of Tsukuba, 1-1-1

Continued

complex networks with many forms of regulation (Lusis et al., 2008; Muoio and Newgard, 2008; Roden and Shulman, 2019). Hence, to comprehensively evaluate the effects of obesity on intracellular regulatory mechanisms requires investigation and integration of omic data of multiple types (transcriptomic, proteomic, and metabolomic) and from multiple organs. Few, if any, studies have taken such an integrated, multi-organ approach.

To effectively model regulation of metabolism requires not only integration of transcriptomic, proteomic, and metabolomic data but also using bioinformatics to link these datasets together through regulation. Transcriptional changes need to be connected to transcription factors (TFs) and posttranslational changes need to be connected to the enzymes mediating those modifications, such as connecting kinases to phosphorylation events. Metabolite regulation of metabolic enzymes requires linking such metabolites to relevant enzymes. Hence, metabolic reactions are regulated by an integrated network consisting of metabolites as substrates and products as well as allosteric regulators and their activation status, metabolic enzymes and their activation status, TFs and their activation status, and signaling molecules, such as kinases. Previously, we investigated the regulatory network controlling metabolic reactions by integrating simultaneous measurements of the amounts of metabolites, the expression of and the activation status of metabolic enzymes, and the amount and the activation status of signaling molecules into a multi-layered trans-omic network that also includes inferred TFs and metabolite-mediated regulation of metabolic reactions (Kawata et al., 2018; Kokaji et al., 2020; Yugi and Kuroda, 2017, 2018; Yugi et al., 2014, 2019). To date, we have used analysis of trans-omic network to establish a regulatory network of metabolic reactions changed by insulin stimulation in cultured cells and that of metabolic reactions responded to glucose administration in the livers of healthy and obese mice (Kokaji et al., 2020). Soltis et al. reported a molecular interaction network from molecules changed by high-fat-diet-associated obesity in multiple omic data but only of the liver (Soltis et al., 2017). Thus, the available studies have only evaluated either cultured cells or a single organ.

Because obesity impairs metabolic homeostasis in various organs, such as the liver and skeletal muscle, and inter-organ metabolic cycles between them through the blood, it is necessary to generate a trans-omic network that includes multi-omic data from the relevant organs and data from blood samples. The leptin-deficient obese (*ob*/*ob*) mice are a widely used model of obesity and insulin resistance, because these mice become profoundly obese by overeating because of deficiency of the anorexigenic hormone leptin (Ingalls et al., 1950; Lindström, 2007). Here, we constructed trans-omic networks for the liver and skeletal muscle by comparing data obtained from fasted wild-type (WT) and *ob*/*ob* mice. Using these trans-omic networks, we provided potential mechanisms of the dysfunctions of the glucose-alanine, glucose-lactate, and ketone body cycles between the liver and skeletal muscle, which characterize the dysfunctional systemic metabolism in *ob*/*ob* mice.

RESULTS

Overview of the approach for constructing trans-omic networks from WT and *ob*/*ob* mice

We constructed trans-omic networks for differentially regulated metabolic reactions in liver and skeletal muscle between WT and *ob*/*ob* mice. We measured the amount and phosphorylation status of signaling molecules, global gene expression, global protein expression, and the amounts of metabolites and lipids in liver and skeletal muscle, along with the amounts of metabolites in the blood, of WT and *ob*/*ob* mice. We then selected the data relevant to metabolic reactions from the transcriptomic and proteomic datasets. By integrating these data, we constructed trans-omic networks for differentially regulated metabolic reactions in liver and skeletal muscle of *ob*/*ob* mice compared with WT mice (Figure 1).

We used 10-week-old WT and *ob*/*ob* mice that had fasted for 16 h. We collected liver, skeletal (gastrocnemius) muscle, and blood from the mice. Some of the liver and blood data were those reported in our previous study (Kokaji et al., 2020). The skeletal muscle data were obtained in this study and were from the same mice that were used to obtain the liver and blood data (Kokaji et al., 2020). Fasting glucose and insulin concentrations in the blood of *ob*/*ob* mice were significantly higher than those of WT mice, indicating that *ob*/*ob* mice exhibit the expected hyperglycemia and hyperinsulinemia (Figure S1).

To identify molecules (phosphorylated proteins, transcripts, proteins, metabolites, and lipids) that were differentially abundant between WT and *ob*/*ob* mice, we set the FDR-adjusted p value (q value) of less than 0.1 (Figure 1: Step1). We classified the differentially expressed molecules as either increased or decreased in *ob*/*ob* mice relative to their abundance in WT mice. We identified the regulatory connections

Tennodai, Tsukuba, Ibaraki, 305-8575, Japan

[10]Center for Artificial Intelligence Research, University of Tsukuba, 1-1-1 Tennodai, Tsukuba, Ibaraki, 305-8577, Japan

[11]Metabolism and Nutrition Research Unit, Institute for Frontier Science Initiative, Kanazawa University, 13-1 Takaramachi, Kanazawa, Ishikawa, 920-8641, Japan

[12]Division of Integrated Omics, Research Center for Transomics Medicine, Medical Institute of Bioregulation, Kyushu University, 3-1-1 Maidashi, Higashi-ku, Fukuoka 812-8582, Japan

[13]Department of Molecular and Cellular Biology, Medical Institute of Bioregulation, Kyushu University, 3-1-1 Maidashi, Higashi-ku, Fukuoka 812-8582, Japan

[14]Institute for Advanced Biosciences, Keio University, 246-2 Mizukami, Kakuganji, Tsuruoka, Yamagata, 997-0052, Japan

[15]Core Research for Evolutional Science and Technology (CREST), Japan Science and Technology Agency, Bunkyo-ku, Tokyo 113-0033, Japan

[16]These authors contributed equally

[17]Lead contact

*Correspondence: skuroda@bs.s.u-tokyo.ac.jp

https://doi.org/10.1016/j.isci.2021.102217

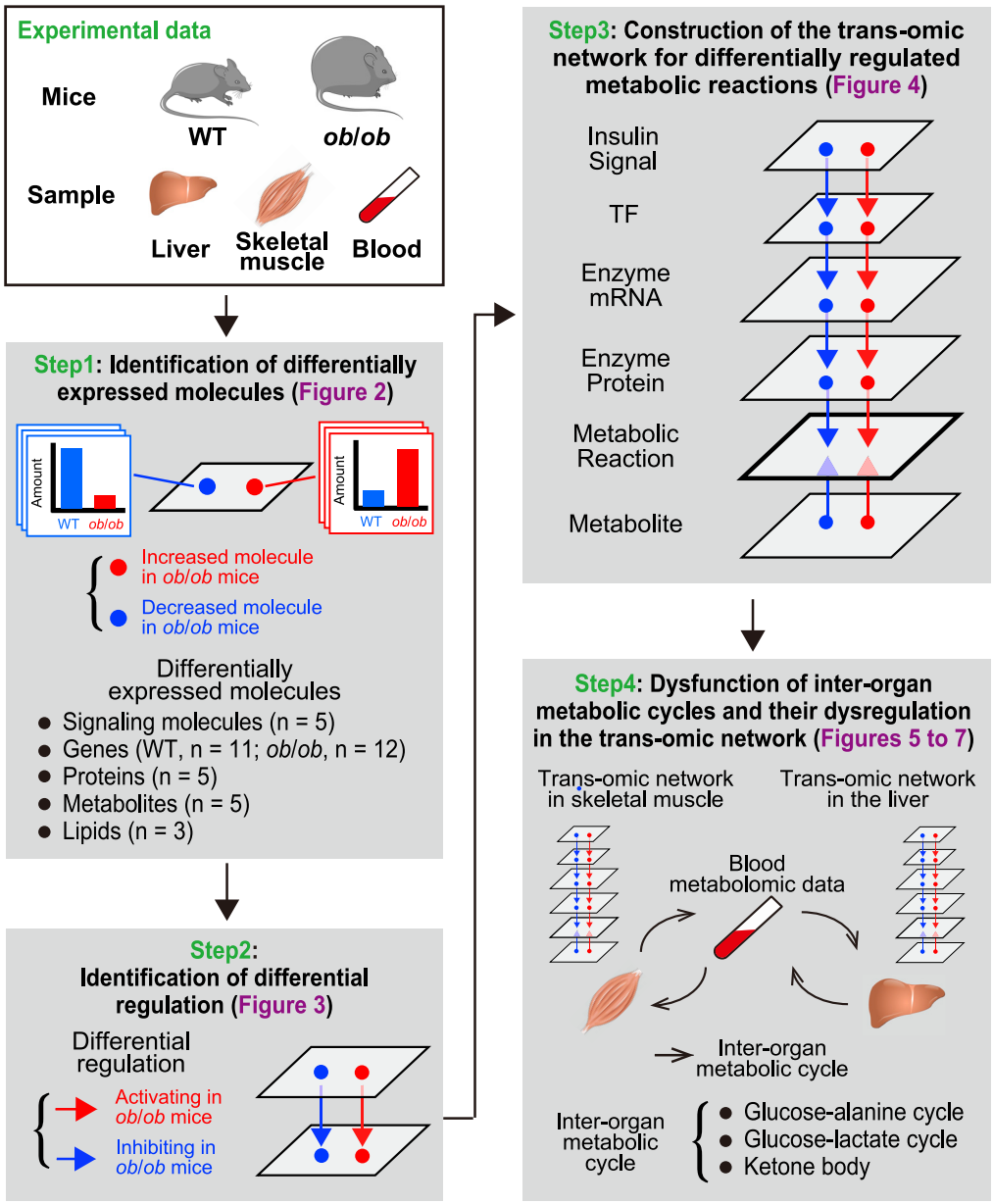

Figure 1. Overview of the approach for constructing trans-omic networks from WT and *ob/ob* mice

We used WT and *ob/ob* mice and collected the liver, skeletal muscle, and the blood from 16-h-fasted mice. We measured signaling molecules, genes, proteins, metabolites, and lipids in the liver and skeletal muscle and identified differentially expressed molecules that significantly increased or decreased in *ob/ob* mice compared with WT mice in each omic layer (Step 1). We also measured metabolites in the blood. We identified the regulations connecting regulating differentially expressed molecules with regulated differentially expressed molecules using bioinformatic methods and multiple databases and defined those as "differential regulations" (Step 2). The differential regulations are classified into either activating regulation in *ob/ob* mice compared with WT mice (red arrow) or inhibiting regulation in *ob/ob* mice compared with WT mice (blue arrow). By integrating differentially expressed molecules and differential regulations that are involved in "metabolic reactions," we constructed the trans-omic network for differentially regulated metabolic reactions in the liver and skeletal muscle (Step 3). Together with the blood metabolomic data, we examined dysfunction of inter-organ metabolic cycles and their dysregulation in the trans-omic network in the liver and skeletal muscle of *ob/ob* mice (Step 4). We used the following number of mouse replicates for each analysis: n = 5 both in WT and *ob/ob* mice for the identification of phosphorylated molecules, n = 11 (WT mice) and n = 12 (*ob/ob* mice) for transcriptomics, n = 5 both in WT and *ob/ob* mice for proteomics, n = 5 both in WT and *ob/ob* mice for metabolomics, and n = 3 both in WT and *ob/ob* mice for lipidomics.

for differentially expressed molecules using multiple databases and defined those as "differential regulations" (Figure 1: Step2). We classified the differential regulations as either activating or inhibiting in *ob*/*ob* mice compared with WT mice. By integrating the differentially expressed molecules and the differential regulations that are involved in "metabolic reaction," we constructed a liver trans-omic network and a skeletal muscle trans-omic network for differentially regulated metabolic reactions (Figure 1: Step3). We grouped differentially expressed molecules from each type of data into layers connected by the differential regulations. The top layer represented signaling input from insulin (Insulin Signal) connected to a TF layer connected to layer representing the differentially expressed genes encoding metabolic enzymes (Enzyme mRNA) connected to layer representing the differentially expressed metabolic enzymes (Enzyme Protein) connected to a metabolic reactions layer (Metabolic Reaction). The Metabolic Reaction layer included regulatory input from both the Enzyme Protein layer and a metabolites (Metabolite) layer through allosteric regulation by metabolites and by changes in the amounts of substrates or products. Together with the blood metabolomic data, we used the trans-omic networks to identify dysfunction and dysregulation of inter-organ metabolic cycles between liver and skeletal muscle of *ob*/*ob* mice (Figure 1: Step4).

Identification of differentially expressed molecules in liver and skeletal muscle of *ob*/*ob* mice

Using livers and skeletal muscle from fasted WT and *ob*/*ob* mice, we measured the total amount and phosphorylation of 29 proteins involved in insulin signaling by western blotting (Figure S2; Table S1). We also calculated the ratio of phosphorylated to total protein for 14 paired molecules and identified those with a ratio of phosphorylated to total that was significantly different between WT and *ob*/*ob* mice as the differentially phosphorylated proteins (DPPs) (Figure 2A). The only increased DPP in both the liver and skeletal muscle of *ob*/*ob* mice was the beta subunit of the insulin receptor (Irβ), which is consistent with the hyperinsulinemia observed in *ob*/*ob* mice (Figure S1). The only decreased DPP was the energy-sensing kinase Ampkα in the liver, which is consistent with increased ATP and decreased AMP in *ob*/*ob* mice (see Figures 2D and S10A) (Hardie, 2011). Akt and Foxo1 were liver-specific increased DPPs in the liver, whereas Erk, S6, and As160 were skeletal-muscle-specific increased DPPs.

We measured the expression of 13,795 genes in the liver and 14,301 genes in skeletal muscle from fasted WT and *ob*/*ob* mice using RNA sequencing (RNA-seq) (Figure 2B; Table S2). We defined genes that were significantly different in *ob*/*ob* mice compared with WT mice as differentially expressed genes (DEGs). We identified 4,253 upregulated DEGs and 3,611 downregulated DEGs in liver of *ob*/*ob* mice and 3,721 upregulated DEGs and 3,869 downregulated DEGs in skeletal muscle (Figure 2B). In both the liver and skeletal muscle, we observed the upregulation of genes involved in lipid metabolism (*Acaca*). In contrast, the DEGs encoding proteins involved in glycolysis and gluconeogenesis (*Gck*, *Gapdh*, *Pgk1*, *Pklr*) were upregulated in the liver, whereas the DEG encoding proteins involved in glycolysis and gluconeogenesis (*Gapdh*) were downregulated in skeletal muscle.

Using iBAQ mass spectrometry (iBAQ-MS), we measured the expression of proteins in the liver and skeletal muscle from fasted WT and *ob*/*ob* mice. We defined the significantly different proteins in *ob*/*ob* mice compared with WT mice as differentially expressed proteins (DEPs) (Figure 2C; Table S3). Out of 2,373 proteins detected in liver, we identified 665 increased DEPs and 770 decreased DEPs in *ob*/*ob* mice; out of 1,078 proteins detected in skeletal muscle, we identified 52 increased DEPs and 21 decreased DEPs in *ob*/*ob* mice (Figure 2C). The increased DEPs in the liver of *ob*/*ob* mice included the metabolic enzymes in glycolysis/gluconeogenesis (Gck, Gapdh, Pgk1, Pklr), whereas the decreased DEPs in skeletal muscle of *ob*/*ob* mice included those in the glycolysis/gluconeogenesis (Gapdh, Pgk1).

Using capillary electrophoresis mass spectrometry (CE-MS), we measured the amounts of polar metabolites, including carbohydrates, amino acids, polar lipids, and nucleic acids, in the liver and skeletal muscle from fasted WT and *ob*/*ob* mice, and defined polar metabolites that significantly changed in *ob*/*ob* mice compared with WT mice as the differentially expressed metabolites (DEMs) (Figure 2D; Table S4). We detected 167 polar metabolites in liver and identified 63 increased and 39 decreased DEMs in *ob*/*ob* mice (Figure 2D). In the skeletal muscle, we detected 102 polar metabolites with only 1 that increased, pantothenate, and 10 that decreased in *ob*/*ob* mice (Figure 2D). The increased DEMs in the liver of *ob*/*ob* mice included the cofactors ATP and glutathione (GSH), intermediate metabolites of the glycolysis/gluconeogenesis (glucose-6-phosphate (G6P), fructose-6-phosphate (F6P), and fructose-1,6-bisphosphate (F1,6P)), and the branched-chain amino acids (BCAAs) (Val, Leu, and Ile), and the decreased DEMs included AMP. The decreased DEMs in skeletal muscle from *ob*/*ob* mice included several that are particularly

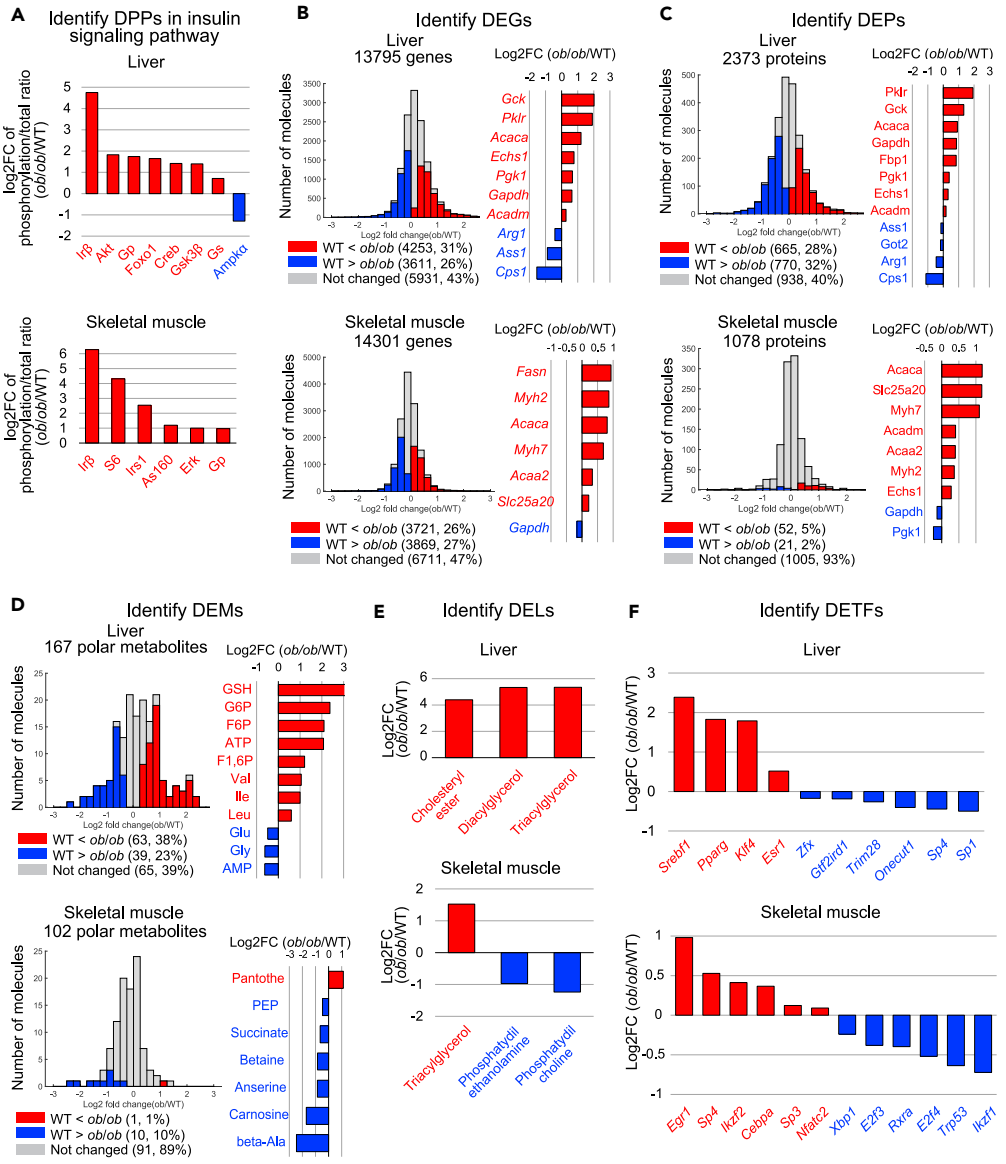

Figure 2. Identification of differentially expressed molecules in liver and skeletal muscle of *ob/ob* mice

(A) The $\log_2$ fold changes of differentially phosphorylated proteins (DPPs) whose ratio significantly changed between WT and *ob/ob* mice. Red, the increased DPPs; blue, the decreased DPPs. See also Figure S2 and Table S1.

(B) Histogram of $\log_2$ fold changes of the expression of genes between WT and *ob/ob* mice (left). Red, the increased differentially expressed genes (DEGs); blue, the decreased DEGs. The $\log_2$ fold changes of the indicated DEGs (right). See also Table S2.

(C) Histogram of $\log_2$ fold changes of the expression of proteins between WT and *ob/ob* mice (left). Red, the increased differentially expressed proteins (DEPs); blue, the decreased DEPs. The $\log_2$ fold changes of the indicated DEPs (right). See also Table S3.

(D) Histogram of $\log_2$ fold changes of the amounts of polar metabolites between WT and *ob/ob* mice (left). Red, the increased differentially expressed metabolites (DEMs); blue, the decreased DEMs. The $\log_2$ fold changes of the indicated DEMs (Right). See also Table S4.

(E) The $\log_2$ fold changes of the amounts of the increased differentially expressed lipids (DELs) in the liver between WT and *ob/ob* mice. See also Table S5. (F) The $\log_2$ fold changes of gene expression of inferred TFs, which are the DETFs. Data are shown as the mean of mice replicate (number indicated in transparent methods). See also Figure S13 and Table S6.

See Table S1 for the unabbreviated names of the phosphorylated molecules. Metabolites are abbreviated as follows: ATP, Adenosine triphosphate; GSH, Glutathione; G6P, Glucose-1-phosphate; F6P, Fructose-6-phosphate; F1,6P, Fructose-1,6-bisphosphate; PEP, Phosphoenolpyruvate; Pantothe, Pantothenate; beta-Ala, beta-alanine. Note that error bars are not provided because the fold change of averaged values of WT and *ob/ob* mice were used.

abundant in muscle: succinate, phosphoenolpyruvate (PEP), some amino acids such as beta-alanine and betaine, and the antioxidants anserine and carnosine, which are abundant in muscle compared with other organs (Kohen et al., 1988; Boldyrev et al., 2013).

Using liquid chromatography mass spectrometry (LC-MS), we measured the amount of 14 lipids in liver and skeletal muscle of fasted WT and *ob*/*ob* mice and defined lipids that significantly changed in *ob*/*ob* mice compared with WT mice as the differentially expressed lipids (DELs) (Figure 2E and Table S5). We identified three increased DELs in the liver and no decreased DELs. In contrast, skeletal muscle had one increased DEL and ten decreased DELs. Triacylglycerol (TAG) increased in both liver and skeletal muscle of fasted *ob*/*ob* mice. The skeletal-muscle-specific decreased DELs included phosphatidyl ethanolamine (PE) and phosphatidyl choline (PC) in skeletal muscle (Figure 2E).

Gene expression is regulated by the TF. Here, we inferred the TFs that regulate the DEGs by the TF motif enrichment analysis using the TF binding motif database, TRANSFAC (Matys et al., 2006; Kel et al., 2003). In liver, we identified 7 TF motifs for the increased DEGs and 14 TF motifs for the decreased DEGs in *ob*/*ob* mice; in skeletal muscle, we identified 17 TF motifs for the increased DEGs and 16 TF motifs for the decreased DEGs (Table S6). Of the TFs corresponding to inferred TF motifs, we identified those included in the DEGs and defined them as the differentially expressed TFs (DETFs). In liver, the increased DETFs included *Srebf1*, *Pparg*, *Klf4*, and *Esr1*, whereas the decreased DETFs included *Sp1* and *Trim28* (Figure 2F; see also Figure S13). In skeletal muscle, the increased DETFs included *Cebpa*, *Sp4*, and *Egr1*, whereas the decreased DETFs included *Xbp1* and *Trp53* (Figure 2F). We identified the Foxo1 motif for the decreased DEGs (Table S6) and identified the pFoxo1 as an increased DPP (Figure 2A). We defined pFoxo1 as a differentially phosphorylated TF (DPTF). Together with the fact that transcriptional activity of Foxo1 decreased by phosphorylation-mediated nuclear export (Barthel et al., 2005), the transcriptional activity of Foxo1 is likely to be decreased in *ob*/*ob* mice. Hereafter, we defined the DETFs and the DPTF as differentially regulated TFs (DRTFs). The skeletal-muscle-specific increased DRTFs included *Egr1*. Given that Foxo1 and *Egr1* are downstream molecules of Akt (Barthel et al., 2005) and Erk (Thiel and Cibelli, 2002), respectively, these identified DRTFs are consistent with the liver-specific increased phosphorylation of Akt and skeletal-muscle-specific increased phosphorylation of Erk (Figure 2A).

Identification of differential regulation in liver and skeletal muscle of *ob*/*ob* mice

We identified the differential regulations connecting regulating differentially expressed molecules with regulated differentially expressed molecules. To identify differential regulations linking DPPs in the insulin signaling molecules to DRTFs, we searched KEGG (Kanehisa et al., 2017) for kinase-substrate relationships between the DPPs and DRTFs. The only differential regulations we found was from Akt, an increased DPP in liver, to Foxo1, an increased DRTF in liver (Figure 2A). The differential regulations between DRTFs and DEGs were determined based on the relationship between the DRTF and the change in expression of the DEG. To identify differential regulations from DEGs to DEPs, we examined the DEP and DEG datasets for protein-encoding gene pairs that showed consistent changes in gene expression and protein expression in *ob*/*ob* mice (Figure 3A; see also Figure S3 and Table S7). In liver, 394 increased DEPs (60% of the total 565 increased DEPs) had upregulated DEGs, and 296 decreased DEPs (40% of the total 743 decreased DEPs) had downregulated DEGs. In skeletal muscle, 29 increased DEPs (59% of total 49 increased DEPs) had correspondingly increased DEGs, whereas 7 decreased DEPs (37% of total 19 decreased DEPs) had decreased DEGs. These data suggested that, although more DEPs were regulated in liver than in skeletal muscle, similar proportions of DEPs were regulated at the level of gene expression in both liver and skeletal muscle in *ob*/*ob* mice.

To examine the expression of metabolic enzymes responsible for metabolic reactions, we identified metabolic enzymes among the DEPs and defined them as the differentially expressed metabolic enzymes (DEMEs). We identified 246 increased and 175 decreased DEMEs in the liver of *ob*/*ob* mice and 21 increased and 6 decreased DEMEs in skeletal muscle of *ob*/*ob* mice (Figure 3B).

The activity of metabolic reactions is regulated not only by the expression of metabolic enzymes but also through allosteric regulation by metabolites and by changes in the amounts of substrates or products. We identified allosteric regulations connecting DEMs to metabolic reactions using the database BRENDA (Jeske et al., 2019) (Figures 3C and S4A). The differential regulations from DEMs were classified as either activating or inhibiting and were determined by combining the direction of the change in a DEM (increased

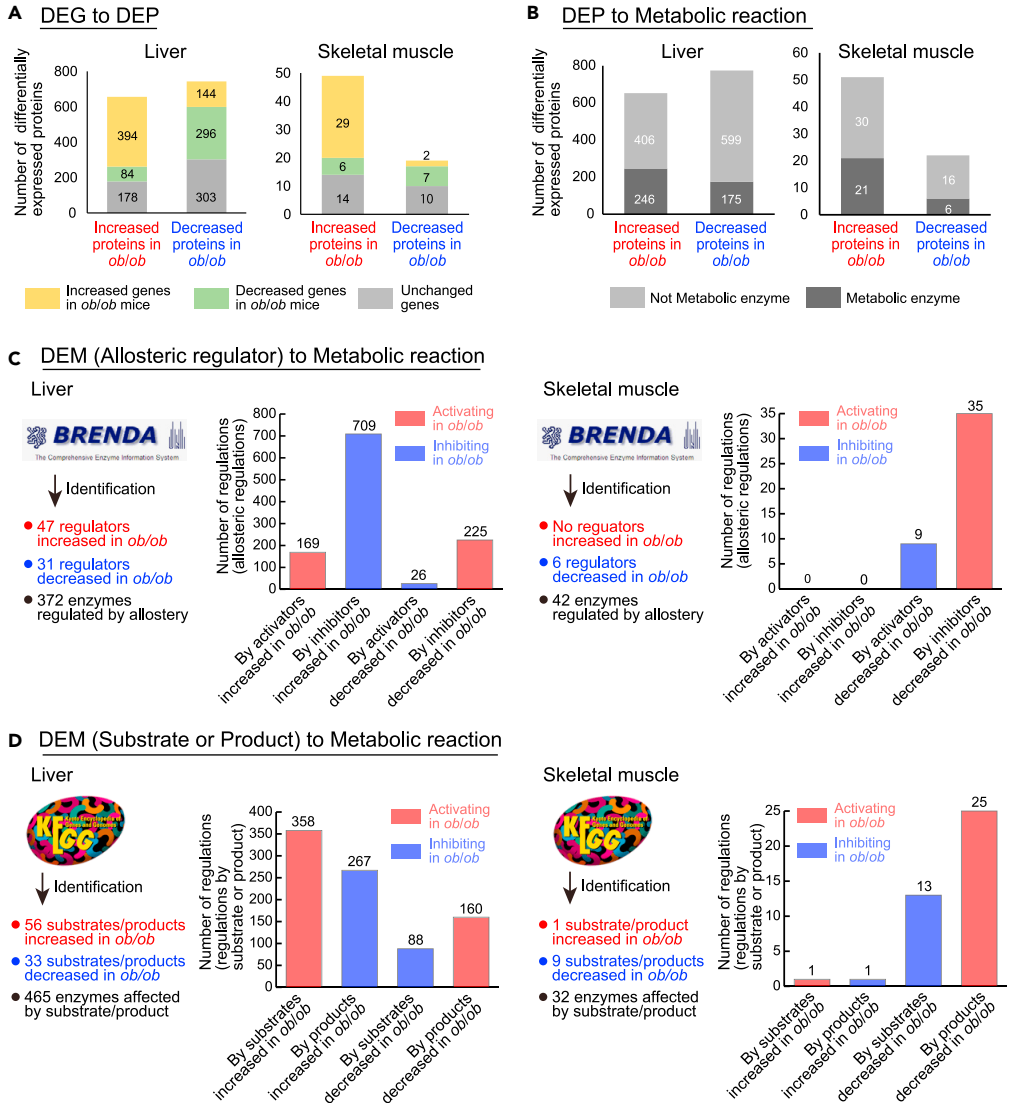

Figure 3. Identification of differential regulation in liver and skeletal muscle of *ob/ob* mice

(A) The number of DEPs encoded by DEGs in the liver and skeletal muscle. The IDs of proteins and genes were unified based on Ensembl protein ID. See also Figure S3 and Table S7.

(B) The number of metabolic enzymes among the DEPs in the liver and skeletal muscle. The IDs of proteins were unified based on Entrez.

(C) The number of allosteric regulators of DEMs and metabolic enzymes regulated by those identified by the analysis using BRENDA and the number of allosteric regulations for metabolic enzymes. See also Figure S4.

(D) The number of substrate or product of DEMs and metabolic enzymes regulated by those identified by the analysis using KEGG and the number of regulations by substrate or product for metabolic enzymes. See also Figure S4.

or decreased) and the direction of its regulatory effect on the reaction (activator or inhibitor) (Figure S4A). In liver, we identified 372 metabolic enzymes that were controlled by DEMs that are allosteric regulators and total 1,129 allosteric regulations to metabolic reactions, with AMP contributing most of the activating allosteric regulation and ATP and ADP inhibiting many reactions through allostery (Figures 3C and S4B). In skeletal muscle, we identified 42 metabolic enzymes that were controlled by DEMs, and both activating and inhibiting allosteric regulations were mediated by DEMs that decreased in *ob/ob* mice (Figures 3C and S4D). Among the DEMs, we also identified the substrates and products that can affect metabolic reactions using the database KEGG (Kanehisa et al., 2017) (Figures 3D and S4A). In liver, we identified 465 metabolic enzymes affected by DEMs that are substrates or products and 873 regulations between those

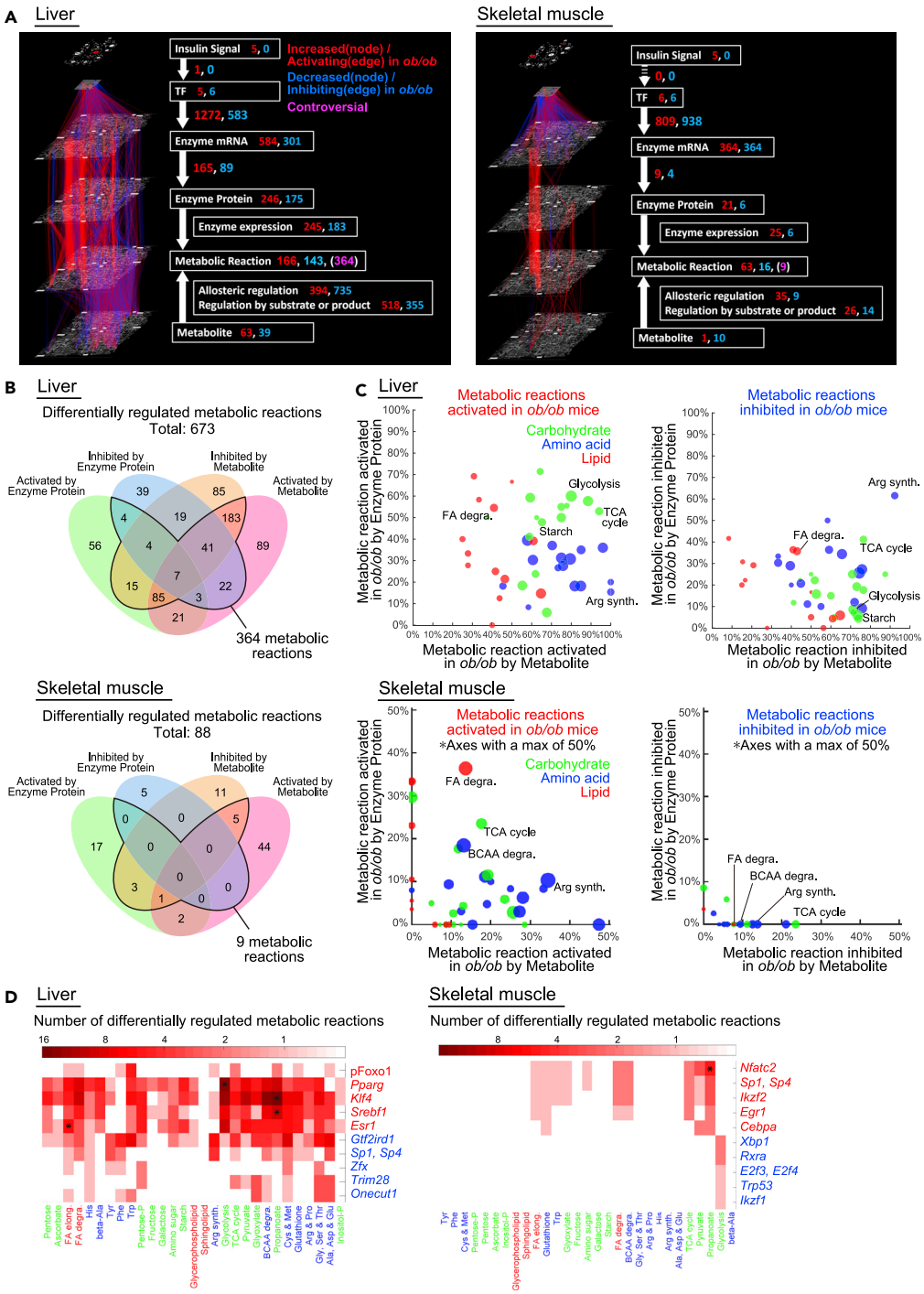

Figure 4. Construction of trans-omic networks for differentially regulated metabolic reactions in liver and skeletal muscle of *ob/ob* mice

(A) The trans-omic network for differentially regulated metabolic reactions in the liver and skeletal muscle. Nodes and edges indicate differentially expressed molecules and differential regulations involved in metabolic reactions, respectively. Red, increased (nodes) or activating (edges) in *ob/ob* mice; blue, decreased (nodes) or inhibiting (edges) in *ob/ob* mice; magenta, controversial metabolic reactions had opposing regulatory input from Enzyme Protein layer and Metabolite layer. The numbers of differentially expressed molecules (nodes) and differential regulations (edges) are shown.

Figure 4. *Continued*

(B) The number of differentially regulated metabolic reactions controlled by differentially expressed molecules in the Enzyme Protein layer or the Metabolite layer or both in the liver and skeletal muscle.

(C) For each metabolic pathway in the liver and skeletal muscle, the percentage of activated (upper) or inhibited (lower) metabolic reactions by Metabolite (*x* axis) and by Enzyme Protein (*y* axis) are plotted. The size of the dots indicates the number of differentially regulated metabolic reactions in each metabolic pathway regulated either by Metabolite, Enzyme Protein, or both in each organ. The colors of the dots indicate the classes of metabolic pathway according to the KEGG database: carbohydrate (green), amino acid (blue), and lipid (red).

(D) The number of differentially regulated metabolic reactions in each metabolic pathway (rows) regulated by each differentially regulated transcription factor (DRTF) (columns) in the liver and skeletal muscle. The sign * indicates the significant associations (q value <0.01) between differentially regulated metabolic reactions in the metabolic pathway node and those regulated by the DRTF. The q value was calculated by one-tailed Fisher's exact test.

See also Figures S5–S10.

enzymes and the DEMs that are substrates or products (Figures 3D and S4C). Some DEMs, including ATP, ADP, and NAD^+, were involved in both allosteric regulations and regulations by substrate or product in the liver of *ob*/*ob* mice. In skeletal muscle, we identified 32 metabolic enzymes affected by changes of the substrates or products and 40 differential regulations by substrate or product DEMs (Figures 3D and S4E).

Construction of trans-omic networks for differentially regulated metabolic reactions in liver and skeletal muscle of *ob*/*ob* mice

To elucidate the regulatory networks controlling the differences in metabolic reactions in liver and skeletal muscle between fasted WT and *ob*/*ob* mice, we constructed trans-omic networks for differentially regulated metabolic reactions in both organs (Figure 4A). The trans-omic networks consisted of two parts, the differentially expressed molecules, which are the nodes in each layer (Figure S5, upper left), and the differential regulations, which are edges connecting nodes in different layers (Figure S5, upper right). The Enzyme mRNA layer contained DEGs for all metabolic enzymes in the pathways in "Metabolism" from the KEGG database (Kanehisa et al., 2017). The Enzyme Protein layer contained the DEMEs. The Metabolic Reaction layer contained the metabolic reactions directly regulated by the DEMEs or DEMs and defined them as the differentially regulated metabolic reactions. Some metabolic enzymes mediate more than one reaction; thus, the number of reactions exceeds the number of enzyme proteins. The final trans-omic networks contained the differentially expressed molecules organized in six layers: insulin signaling molecules in DPPs in the Insulin Signal layer, DRTFs in the TF layer, DEGs encoding metabolic enzymes in the Enzyme mRNA layer, DEMEs in the Enzyme Protein layer, differentially regulated metabolic reactions in the Metabolic Reaction layer, and DEMs in the Metabolite layer, with the differential regulations connecting the layers. We classified the differential regulations as either activating or inhibiting the downstream molecules or reactions in *ob*/*ob* mice by combining the direction of changes of differentially expressed molecules (increased or decreased) and the direction of regulation (activation or inhibition) (Figure S5 lower table). The trans-omic network included the differential regulations for various metabolic pathways: glycogen metabolism (Figure S6A), TCA cycle (Figure S6B), glycolysis/gluconeogenesis (see Figures 6A and 6B), fatty acid synthesis (Figure S7), fatty acid degradation (see Figures 7A and 7B), arginine synthesis (Figure S8), BCAA degradation (Figure S9), purine metabolism (Figure S10A), and pyrimidine metabolism (Figure S10B).

For liver, the resulting network included 673 metabolic reactions that were differentially regulated in fasted *ob*/*ob* mice and that had regulatory inputs from the Enzyme Protein layer and the Metabolite layer (Figure 4A, left). Of these 673 metabolic reactions, 364 reactions had opposing regulatory input from those two layers, thus we classified these as "controversial" (Figure 4B, upper). For all differential regulations except those involving allosteric regulation, the number of activating regulations exceeded the number of inhibiting regulations and the number of differentially expressed molecules that increased exceeded those that decreased except in the TF layer, which had equivalent numbers of DRTFs with increased and decreased activity.

For skeletal muscle, the trans-omic network was smaller with only 88 metabolic reactions that were differentially regulated in fasted *ob*/*ob* mice (Figure 4A, right). In contrast to the liver trans-omic network, there was no phosphorylation-mediated regulation from the Insulin Signal layer to the TF layer in skeletal muscle. The number of increased DEMEs was larger than that of decreased DEMEs in the Enzyme Protein layer, whereas the number of the increased DEMs was smaller than that of the decreased DEMs in the Metabolite

layer. For all three types of regulation of enzyme activity—enzyme expression, allosteric regulation, and regulation by substrate or product—the number of activating regulations was larger than that of the inhibiting regulations in skeletal muscle of *ob*/*ob* mice (Figure 4A, right). We calculated the number of differentially regulated metabolic reactions regulated by changes in the Enzyme Protein or Metabolite layers (Figure 4B, lower). In contrast to liver with ~54% of reactions having controversial opposing regulation, skeletal muscle metabolic reactions were more consistently regulated with only 9 of 88 (~10%) reactions regulated in an opposing manner by changes in the Enzyme Protein and Metabolite layers in skeletal muscle.

To elucidate key mechanisms involved in the differences of metabolic reaction between WT mice and *ob*/*ob* mice in liver and skeletal muscle, we grouped metabolic reactions belonging to the same metabolic pathway and calculated the percentage of activated or inhibited metabolic reactions by Metabolite and by Enzyme Protein layers (Figure 4C). We focused on pathways representing carbohydrate, amino acid, and lipid metabolism. Nucleotide metabolism is separately described in supplemental information (see Figures S10A and S10B). In liver, several carbohydrate metabolic pathways, including glycolysis/gluconeogenesis, the starch (glycogen) metabolism, and TCA cycle, and several lipid metabolic pathways, including fatty acid degradation, had more activating regulations than inhibiting regulations by DEMEs (Figures 4C, S7A, and S7B; see also Figures 6A and 7A). This result suggests that these metabolic pathways are activated at the level of protein expression of metabolic enzymes in fasted *ob*/*ob* mice. In skeletal muscle, some metabolic pathways were activated by DEMEs, such as fatty acid degradation and BCAA degradation (Figures 4C and S9 lower; see also Figure 7B). In addition, in both organs, most amino acid metabolic pathways were regulated by DEMs in *ob*/*ob* mice. An exception was inhibition of arginine synthesis pathway in the liver, which involved a high percentage of metabolic reactions controlled by both DEMs and DEMEs (Figures 4C and S8 upper).

We also evaluated the number of metabolic reactions regulated by the increased and decreased DRTFs in the trans-omic networks for liver and skeletal muscle from *ob*/*ob* mice (Figure 4D). This analysis showed that increased DRTFs had a greater impact on the networks than decreased DRTFs. It also showed that across carbohydrate, lipid, and amino acid metabolism, liver showed more complex effects of changes in gene expression with many metabolic pathways having both input from increased and decreased DRTFs. In addition, in liver *Esr1* (*Estrogen receptor 1*) was significantly associated with fatty acid elongation, *Srebf1* (*Sterol regulatory element-binding protein 1*) and *Klf4* (*Kruppel-like factor 4*) were significantly associated with metabolism of the short fatty acid propanoate, and *Pparg* (*Peroxisome proliferator-activated receptor gamma*) was significantly associated with glycolysis/gluconeogenesis. In skeletal muscle, only *Nfatc2* (*Nuclear factor of activated T cells 2*) was significantly associated with any pathway and the association was with propanoate metabolism.

Identification of differentially expressed metabolites in blood from *ob*/*ob* mice

The blood communicates changes in metabolism and metabolic requirements between organs through circulating metabolites. Through such circulation-mediated communication, the liver and skeletal muscle contribute to systemic metabolic homeostasis. Therefore, we analyzed polar metabolites in the blood of fasted WT and *ob*/*ob* mice and compared them with the changes in liver and skeletal muscle of *ob*/*ob* mice (Figures 5 and S11). We measured the amounts of 108 polar metabolites in the blood of WT and *ob*/*ob* mice, using CE-MS, and identified 26 increased and 31 decreased DEMs in the blood of *ob*/*ob* mice (Figure 5A; Table S8). The increased DEMs in the blood included glutathione disulfide (GSSG) and pantothenate. However, most of the decreased DEMs in the blood were amino acids (Ala, Gly, Arg, and His) and their derivatives (betaine, beta-alanine, anserine, and carnosine) (Figure 5B).

We compared the DEMs in the blood with those in the liver and those in skeletal muscle. We identified 11 increased and 11 decreased DEMs common in both blood and liver (Figure S11B) with a modest correlation (Pearson's correlation coefficient = 0.33) detected for these changes between fasted WT and *ob*/*ob* mice. Pantothenate, a core component of coenzyme A (CoA), was the only increased DEM in common between blood and skeletal muscle, and 6 decreased DEMs were common to blood and skeletal muscle (Figure S11B) with a modest correlation (Pearson's correlation coefficients = 0.43) detected for them. We examined the changes of metabolites across the three compartments—liver, skeletal muscle, and blood—between fasted WT and *ob*/*ob* mice (Figure 5C). This analysis revealed 4 metabolites—betaine, beta-alanine, hydroxyproline, and 2-aminobutanoate—significantly decreased in *ob*/*ob* mice across all three compartments. This analysis also revealed metabolites that selectively changed in each

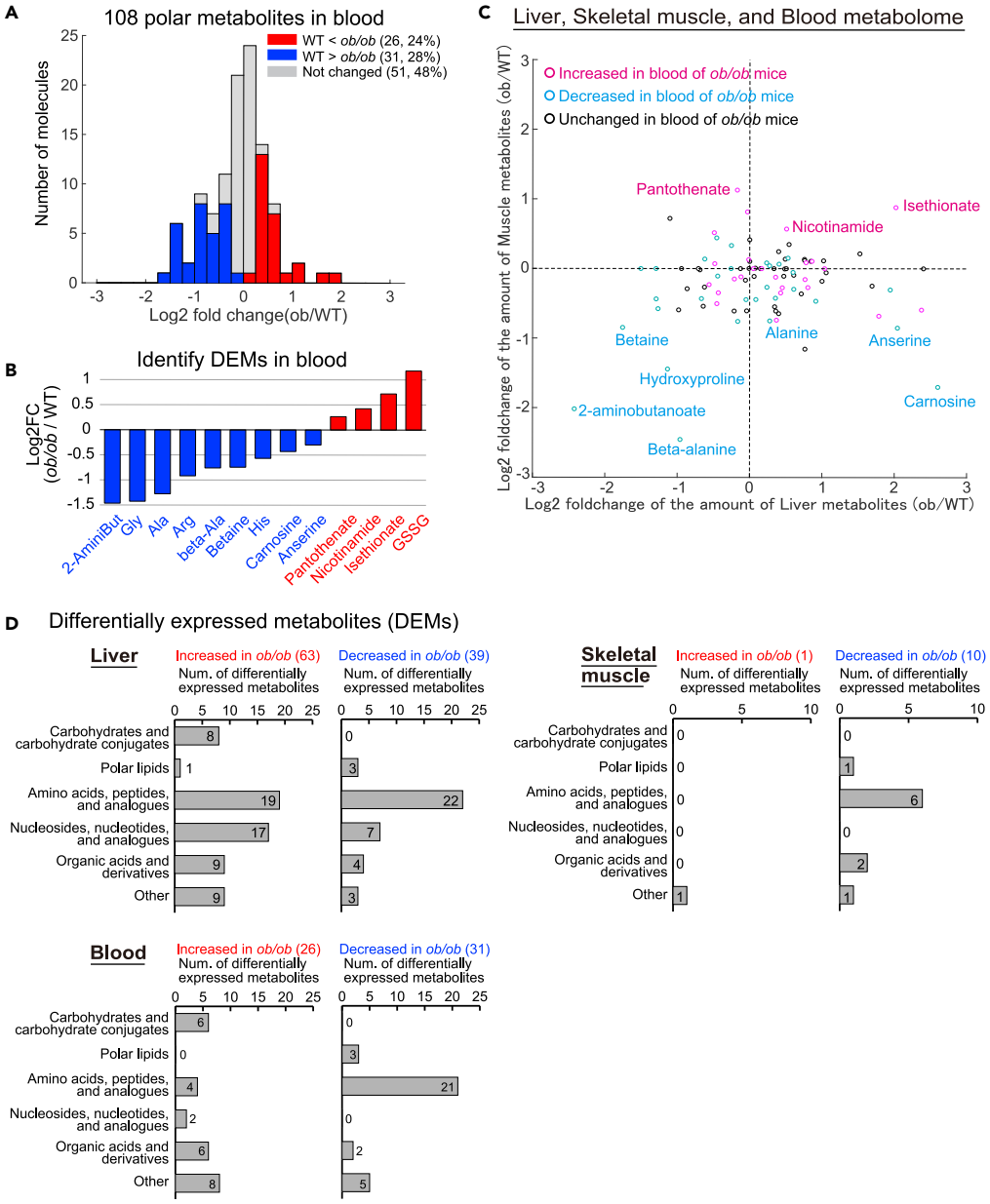

Figure 5. Identification of differentially expressed metabolites in blood from *ob/ob* mice

(A and B) Metabolomic analysis using CE-MS in the blood of WT and *ob/ob* mice. Histogram showing distribution of $\log_2$ fold changes of the amount of blood polar metabolites between WT and *ob/ob* mice (A). The $\log_2$ fold changes of the amounts of the indicated DEMs in the blood between WT and *ob/ob* mice (B). Metabolites are abbreviated as follows: 2-AminoBut, 2-aminobutanoate; beta-Ala, beta-alanine; GSSG, Glutathione disulfide. Note that error bars are not provided because the fold change of averaged values of WT and *ob/ob* mice were used. See also Table S8.

(C) The $\log_2$ fold changes of polar metabolites measured in the liver, skeletal muscle, and the blood between WT and *ob/ob* mice. The value of $\log_2$ fold changes of polar metabolites in the liver (*x* axis) and skeletal muscle (*y* axis) between WT and *ob/ob* mice are shown in scatterplot. The color of each node indicates whether the metabolite is increased DEMs (Magenta) or decreased DEMs (Cyan) in the blood of *ob/ob* mice.

(D) The number of the DEMs classified by metabolite class of KEGG database in the liver, skeletal muscle, and blood. Note that we did not measure lipidome in blood. See also Figure S11.

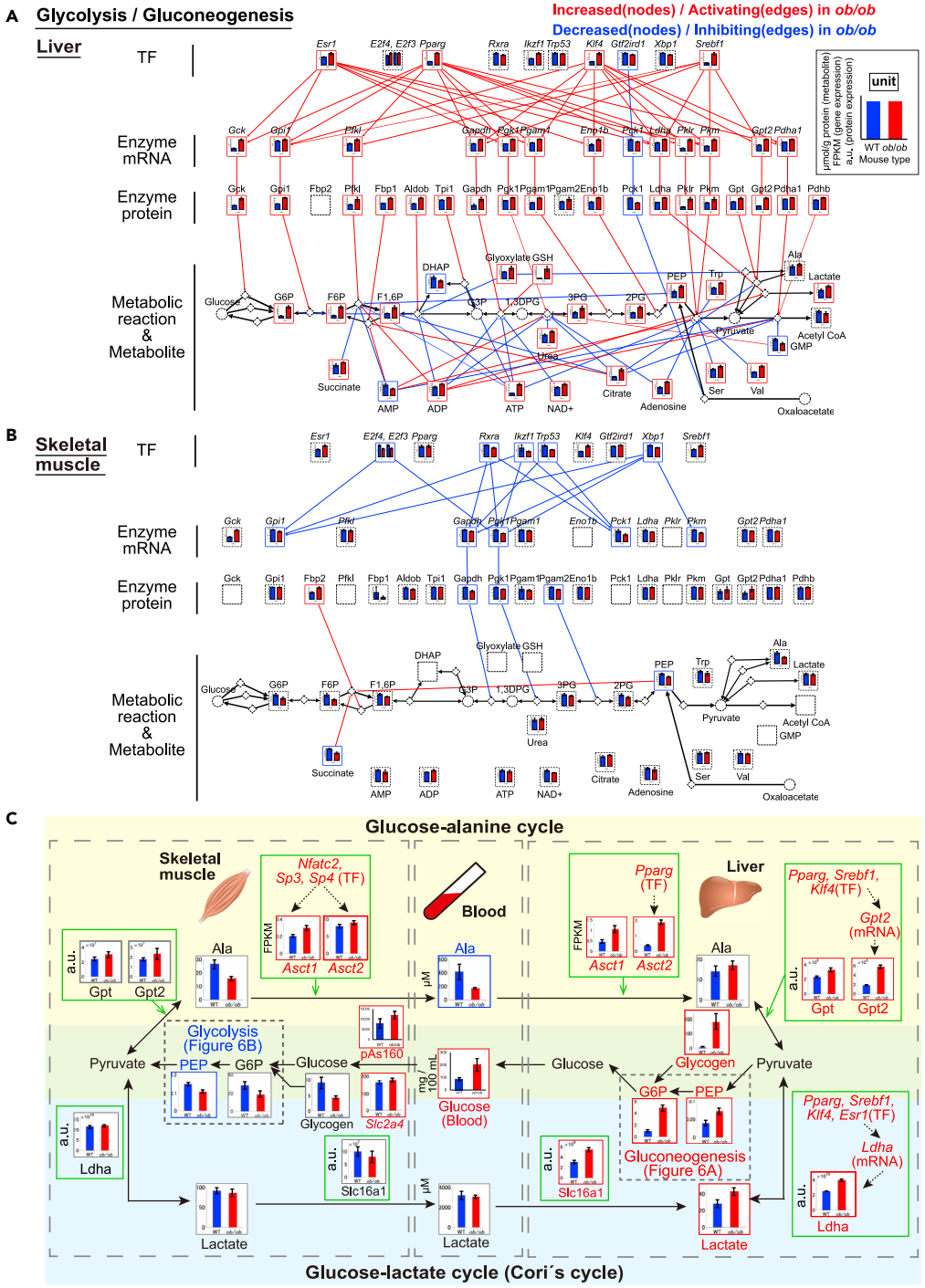

Figure 6. Potential mechanisms of dysfunction of inter-organ metabolic cycles of glucose-alanine and glucose-lactate and their dysregulation in trans-omic network in liver and skeletal muscle of *ob/ob* mice

(A and B) The trans-omic subnetwork for differentially regulated metabolic reactions in glycolysis/gluconeogenesis in the liver (A) and skeletal muscle (B). The information for glycolysis/gluconeogenesis were obtained from "glycolysis/gluconeogenesis" (mmu00010) in the KEGG database, respectively (Kanehisa et al., 2017). The colors of the frames indicate differentially expressed molecules increased in *ob/ob* mice (red) and those decreased in *ob/ob* mice (blue). The significance of differences was tested by two-tailed Welch's t test for each measured protein and polar metabolite and by the edgeR package with default parameters for each measured gene (see also transparent methods). Differentially expressed molecules were molecules with a q value less than 0.1 and were classified as increased or decreased

Figure 6. *Continued*

differentially expressed molecules. The q values were calculated by Storey's procedure for gene expression, protein expression, and polar metabolite. The dashed black frames showed molecules that were not differentially expressed molecules or undetected molecules in the indicated organ. Diamond nodes indicate metabolic reactions. The inter-layered red and blue edges indicate differential regulations: activating regulation in *ob*/*ob* mice (red) and inhibiting regulation in *ob*/*ob* mice (blue). We classified the differential regulations as either activating or inhibiting the downstream molecules in *ob*/*ob* mice by combining the direction of changes of regulating differentially expressed molecules (increased or decreased) and the direction of regulation (activation or inhibition). When the regulation between regulating upstream differentially expressed molecules and regulated downstream differentially expressed molecules is consistent, these regulations are displayed in the network as differential regulations. From Metabolite to Metabolic reaction, only allosteric regulations are colored. Black edges indicate the relationship between metabolic reactions and its substrate/product. The reversibility of metabolic reactions was obtained from the KEGG database. See also Figures S12A and S12B.

(C) A summarized diagram of glucose-alanine (yellow highlighted) and glucose-lactate (light blue highlighted) cycles between liver and skeletal muscle via the blood of WT and *ob*/*ob* mice. The black edges represent the flow of metabolites. Green frames represent the regulation of the expression of indicated metabolic enzymes or transporters in the liver and skeletal muscle. The dotted arrows in the green frames are differential regulations in each organ. Red and blue frames indicate the increased differentially expressed molecules in *ob*/*ob* mice (red) and the decreased those in *ob*/*ob* mice (blue), respectively. Molecules with gray frames did not show the significant differences between WT and *ob*/*ob* mice. The significance of the differences in indicated molecules was determined in the same statistical methods described in Figures 6A and 6B. Bar plots of measured molecules in WT and *ob*/*ob* mice are shown for corresponding nodes as the means and standard error of the means (SEMs) of mice replicate (number indicated in transparent methods).

compartment. For example, alanine, the key factor in the glucose-alanine cycle, slightly increased in the liver but decreased in skeletal muscle and blood.

We also evaluated the DEMs by type of metabolite among the liver, skeletal muscle, and blood (Figure 5D). This comparison showed that amino acids, peptides, and related molecules showed predominantly decreases in blood and skeletal muscle but showed both increases and decreases in liver.

Potential mechanisms of dysfunction of inter-organ metabolic cycles of glucose-alanine and glucose-lactate and their dysregulation in the trans-omic network in liver and skeletal muscle of *ob*/*ob* mice

Because there is limited understanding of how obesity affects the main cycles between liver and skeletal muscle metabolism through the blood, we generated inter-organ metabolic networks for three cycles: the glucose-alanine cycle, the glucose-lactate cycle, and the ketone body cycle. Liver provides gluconeogenesis activity, whereas skeletal muscle consumes glucose through glycolysis. These processes are linked through two cycles (Dashty, 2013; Sarabhai and Roden, 2019). Alanine is transported to the liver and converted into glucose, which is then released into the circulation and taken up by skeletal muscle. This cycle is the glucose-alanine cycle (Felig, 1973). Skeletal muscle converts glucose to lactate, which is then transported to the liver for conversion to glucose. This cycle is called the glucose-lactate cycle (Cori's cycle) (Cori and Cori, 1929). When glucose is limiting, ketone bodies provide a source of energy from fatty acid degradation (Cahill et al., 1966). Therefore, we explored potential mechanisms of how dysregulation of the liver and skeletal muscle trans-omic subnetworks of glycolysis and gluconeogenesis for glucose-alanine and glucose-lactate cycles (Figure 6) and of fatty acid degradation for ketone body cycle (Figure 7) in fasted *ob*/*ob* mice affected these three metabolic cycles.

To investigate glucose-alanine and glucose-lactate cycles between liver and skeletal muscle, we extracted the trans-omic subnetwork of glycolysis/gluconeogenesis pathway from the trans-omic networks in the liver and skeletal muscle according to information of "glycolysis/gluconeogenesis" (mmu00010) in the KEGG database (Kanehisa et al., 2017). Most of the intermediate metabolites in the glycolysis/gluconeogenesis pathway in the liver, such as G6P, F6P, F1,6P, 3-phosphoglycerate (3PG), 2-phosphoglycerate (2PG), and PEP, were the increased DEMs in *ob*/*ob* mice except dihydroxyacetone phosphate (DHAP) (Figure 6A). Many metabolic enzymes were increased DEMEs in *ob*/*ob* mice (17 proteins: 94% of total 18 DEMEs), whereas the only decreased DEME was Pck1 (Figures 6A and S12A). The expression of metabolic enzymes specific to glycolysis, including rate-limiting enzymes, such as Gck and Pfkl, increased in *ob*/*ob* mice, whose genes were also upregulated by the increased DRTFs *Srebf1*, *Pparg*, and *Esr1*. The expression of metabolic enzymes specific to gluconeogenesis, including a rate-limiting enzyme Fbp1, increased in *ob*/*ob* mice. The

expression of metabolic enzymes for overall glycolysis and gluconeogenesis pathways, including Gpi1, Gapdh, and Pgk1, increased in *ob*/*ob* mice. However, these enzymes are not rate-limiting enzymes and may not have large contributions to the regulation of glycolysis and gluconeogenesis. Taken together, these results suggest that both glycolysis and gluconeogenesis pathways are activated by the DEMEs in liver of *ob*/*ob* mice. Because it has been shown that gluconeogenesis is activated in liver of fasted obese human, *ob*/*ob* mice, and high-fat diet-fed mice (Turner et al., 2005; Basu et al., 2005; Satapati et al., 2012), gluconeogenesis is likely to be relatively more dominant than glycolysis in liver of fasted *ob*/*ob* mice. Besides, it has been reported to increase the blood glucose level in fasted *db*/*db* mice, a leptin receptor-deficient mice (Clementi et al., 2011; Liu et al., 2012), and high-fat diet-fed mice more than in wild-type mice and standard-chow-diet-fed mice (Soto et al., 2018), respectively, by intraperitoneal pyruvate administration. These results also support our interpretation that gluconeogenesis is more dominant than glycolysis. In contrast to activating regulation by the DEMEs, majority of allosteric regulation were inhibiting regulation in *ob*/*ob* mice (glycolysis specific: 3 activating and 13 inhibiting regulations, gluconeogenesis specific: 2 activating regulations, common for glycolysis and gluconeogenesis: 4 activating and 21 inhibiting regulations), most of which are mediated by the increased DEMs (Figures 6A and S12A). The activating regulations by the DEMEs and the inhibiting allosteric regulations by the increased DEMs counteract in liver of *ob*/*ob* mice, suggesting that in *ob*/*ob* mice, the DEMEs activate their targets, whereas the DEMs inhibit their targets.

In skeletal muscle of *ob*/*ob* mice, PEP was the only decreased DEM (Figure 6B). Although there were no significant changes in other metabolites in glycolysis/gluconeogenesis pathway, metabolites in the upstream of this pathway, such as G6P [FC (*ob*/*ob*/WT) = 0.66, q value = 0.13], F6P [FC (*ob*/*ob*/WT) = 0.53, q value = 0.12], and F1,6P [FC (*ob*/*ob*/WT) = 0.79, q value = 0.14], slightly decreased in skeletal muscle of *ob*/*ob* mice, unlike in liver. Gapdh, Pgk1, and Pgam2 (phosphoglycerate mutase 2) were identified as decreased DEMEs in skeletal muscle of *ob*/*ob* mice (Figures 6B and S12B), and the gene expression of *Pgk1* and *Gapdh* was regulated at the transcript level by the decreased DRTFs such as *Rxra*, *Trp53*, and *Xbp1* (Figure 6B). Fbp2 was the only increased DEME in this pathway in skeletal muscle of *ob*/*ob* mice. The increase of Fbp2 in skeletal muscle may be involved in glycogenesis but not in gluconeogenesis because G6P is not converted to glucose because of lack of G6Pase expression (Gamberucci et al., 1996; Schaftingen and Gerin, 2002), unlike in liver. The expression of Gapdh and Pgk1 increased in liver of *ob*/*ob* mice, but decreased in skeletal muscle of *ob*/*ob* mice (Figures 6A and 6B), suggesting the possibility that the glycolysis pathway is potentially inhibited by decreased expression of some metabolic enzymes in skeletal muscle of *ob*/*ob* mice. Furthermore, succinate and PEP contributed inhibiting allosteric regulations in liver but activating regulations in skeletal muscle.

To construct the inter-organ metabolic cycles, we not only used the data from the two trans-omic subnetworks (Figures 6A and 6B) but also added data regarding the expression of genes encoding relevant transporters and DRTFs that regulate those genes from our transcriptomic analyses. We also used the proteomic data to identify relevant transporters in liver and skeletal muscle. For the glucose-alanine cycle, we added the *Asct1* and *Asct2* encoding amino acid transporters to both skeletal muscle and liver (Figure 6C) (Freidman et al., 2020; Kandasamy et al., 2018). Although both genes were increased in expression in both organs, the DRTFs responsible for their regulation differed and neither of those transporters were detected in our proteomic data. For the glucose-lactate cycle, we added the monocarboxylate transporter Slc16a1, a major transporter of lactate (Figure 6C) (Halestrap, 2013). Slc16a1 was a DEP that increased in liver but was unchanged in skeletal muscle.

The changes in alanine were not sufficient in liver or skeletal muscle for this metabolite to be a DEM (Figure 6C); although in skeletal muscle alanine was slightly decreased [FC (*ob*/*ob*/WT) = 0.59, q value = 0.10] and in liver alanine was slightly increased [FC (*ob*/*ob*/WT) = 1.21, q value = 0.20)]. Despite these limited changes in alanine in the organs, alanine decreased in the blood of *ob*/*ob* mice, suggesting either decreased release from skeletal muscle or increased uptake by liver. We found increased expression of the alanine transporter genes *Asct1* and *Asct2* in both liver and skeletal muscle, suggesting enhanced uptake in liver. The limited increase in alanine in liver was consistent with increased Gpt and Gpt2, which catalyzes at the conversion of alanine to pyruvate. In the glucose-lactate cycle, lactate was unchanged in skeletal muscle and the blood of *ob*/*ob* mice. However, in liver of *ob*/*ob* mice, lactate and its transporter, Slc16a1, increased (Figure 6C), suggesting the increased uptake of lactate from the blood to the liver. Ldha, which catalyzes lactate to pyruvate, also increased in liver of *ob*/*ob* mice (Figure 6C), consistent with the

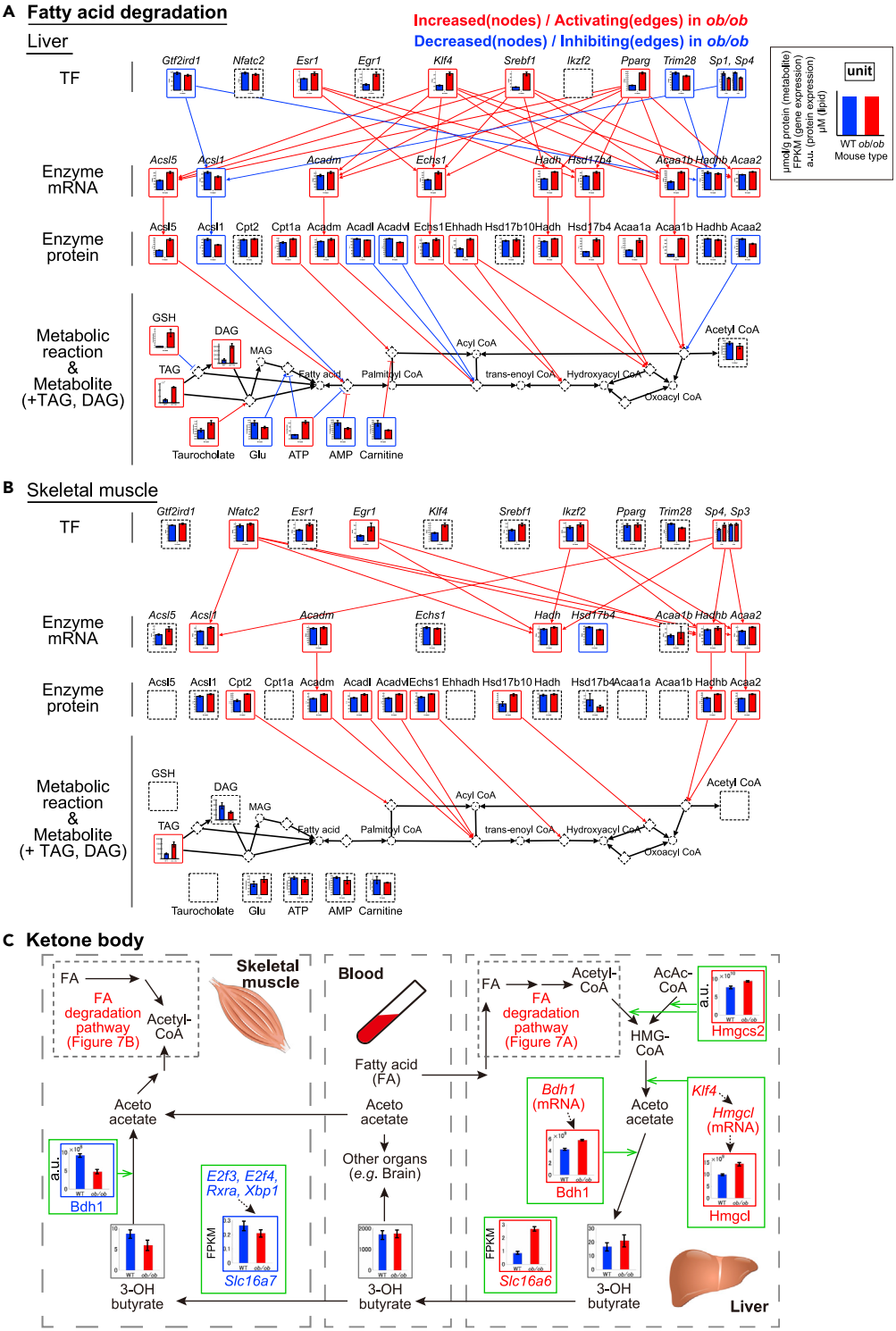

Figure 7. Potential mechanisms of dysfunction of inter-organ metabolic cycles of ketone body and their dysregulation in trans-omic network in liver and skeletal muscle of *ob/ob* mice

(A and B) The trans-omic subnetwork for differentially regulated metabolic reactions in fatty acid degradation in the liver (A) and skeletal muscle (B). The information for fatty acid degradation were obtained from "fatty acid degradation" (mmu00071) and "glycerolipid metabolism" (mmu00561) in the KEGG database. Bar plots of measured molecules in WT and *ob/ob* mice are shown for corresponding nodes as the means and standard error of the means (SEMs) of mice

Figure 7. *Continued*

replicate (number indicated in transparent methods). The definitions of color, edges, arrows, and frames in Figures 7A and 7B are the same as in Figures 6A and 6B, except lipidome data. In the lipidomic analysis, the significance of differences was tested by a two-tailed Welch's t test for each measured lipid (see also transparent methods). TAG and DAG in the liver and TAG in the skeletal muscle were differentially expressed lipids (DELs) with a q value less than 0.1 and were identified as the increased DELs. The q values for lipid were calculated by Benjamini–Hochberg procedure. See also Figures S12C and S12D.

(C) A summarized diagram of ketone body cycle between the liver and skeletal muscle via the blood of WT and *ob*/*ob* mice. The definitions of color, edges, arrows, and frames in Figure 7C are the same as in Figure 6C. Bar plots of measured molecules in WT and *ob*/*ob* mice are shown for corresponding nodes as the means and SEMs of mice replicate (number indicated in transparent methods).

previous finding (Nesteruk et al., 2014). An increase of Gpt2 of the glucose-alanine cycle and Ldha of the glucose-lactate cycle in liver of *ob*/*ob* mice may increase the amount of pyruvate. Although we did not measure the amount of pyruvate, it has been reported that the hepatic pyruvate is actually increased in liver of overnight-fasted *ob*/*ob* mice (Shannon et al., 2021). Therefore, the increased Ldha and Gpt2 can contribute to the activation of gluconeogenesis through the conversion of lactate and alanine to pyruvate. Furthermore, expression of *Gpt2*, *Ldha*, and *Asct2* were upregulated by the DRTF *Pparg* (Figure 6C), suggesting that both glucose-alanine and glucose-lactate cycles in the liver are coordinately regulated at the transcriptional level. Collectively, these results suggested that increased hepatic glucose production occurs from both lactate and alanine in fasted *ob*/*ob* mice.

In addition to increased glucose in the blood in *ob*/*ob* mice, we found an increase in phosphorylation of As160 in skeletal muscle of *ob*/*ob* mice (Figures 2A and 6C). Given that As160 is a GTPase-activating protein (GAP) for Rab GTPases and its phosphorylation inhibits its GTPase activity, resulting in promoting Glut4 translocation into the plasma membrane via Rab GTPases, and consequently enhancing glucose transport (Huang and Czech, 2007), this result suggested the enhancement of glucose transport through Glut4 translocation. In addition, expression of *Slc2a4*/*Glut4* was slightly upregulated in *ob*/*ob* mice (Figure 6C). By contrast, we found reduced glycolysis in skeletal muscle as suggested by slightly decrease in glycolytic metabolites from G6P to PEP together with decreased glycolytic enzymes Gapdh, Pgk1, and Pgam2 and increased gluconeogenesis in liver as suggested by increased Gpt, Gpt2, and Ldha (Figures 6B and 6C). The two facts that increased blood glucose and phosphorylation of As160 and that decreased downstream glycolytic metabolites (G6P to PEP) are contradictory, implying an existence of dysregulation of glucose transport in skeletal muscle. Consistently, it has been shown that glucose uptake is reduced in skeletal muscle of *ob*/*ob* mice (Ohshima et al., 1984). These results suggest the possibility that Glut4 translocation to plasma membrane, which is downstream of As160, is impaired in *ob*/*ob* mice, leading to the opposite changes of blood glucose and glycolytic metabolites in skeletal muscle in *ob*/*ob* mice. Taken together, blood glucose and blood alanine showed the similar changes to those in the releasing organs (the liver for glucose, skeletal muscle for alanine and lactate) and the opposite changes to glucose, alanine, and lactate in the uptaking organs (skeletal muscle for glucose, the liver for alanine and lactate). This result suggests that abnormal changes of blood glucose, blood alanine, and blood lactate resulted from the imbalance of metabolic pathways in releasing and uptaking organs.

Thus, the trans-omic analysis of inter-organ metabolic cycles provided the potential mechanisms of obesity-associated dysfunction in cycles between liver and skeletal muscle in glucose-alanine and glucose-lactate and its potential dysregulation.

Potential mechanisms of dysfunction of inter-organ metabolic cycles of ketone body and their dysregulation in the trans-omic network in liver and skeletal muscle of *ob*/*ob* mice

We investigated potential mechanisms of dysfunction of ketone body cycle in liver and skeletal muscle. We extracted the trans-omic subnetwork of fatty acid degradation pathway from the trans-omic networks in the liver and skeletal muscle according to information of "fatty acid degradation" (mmu00071) and "glycerolipid metabolism" (mmu00561) in the KEGG database (Kanehisa et al., 2017). TAG and DAG, which are intermediate lipids in the fatty acid degradation pathway, increased in the liver of *ob*/*ob* mice (Figure 7A), consistent with the previous findings (Yu et al., 2004; Perfield et al., 2013). Nine enzymes were increased DEMEs in the liver of *ob*/*ob* mice, whereas 4 enzymes were the decreased DEMEs. Among the increased DEMEs, Acsl5, Acadm, Ecsh1, Hadh, Hsd17b4, and Acaa1b showed the increased expression at the transcript level by the increased DRTFs, *Pparg*, *Srebf1*, *Esr1*, and *Klf4* (Figure 7A). Taken together, these results

imply that fatty acid degradation pathway is potentially activated at enzyme level in the liver of *ob*/*ob* mice. In addition, there was some allosteric regulations by the DEMs such as ATP and GSH in the liver of *ob*/*ob* mice (3 activating and 4 inhibiting regulations) (Figure S12C). In skeletal muscle of *ob*/*ob* mice, TAG was also identified as the increased DEM (Figure 7B), consistent with the previous finding (Mastrocola et al., 2015). All eight DEMEs increased in skeletal muscle of *ob*/*ob* mice (Figures 7B and S12D), and of these increased DEMEs, Cpt2, Acadm, Acadl, Acadvl, and Ecsh1 have been previously reported to increase (Schönke et al., 2018). Expression of Hadhb and Acaa2 was regulated at the transcript level by the increased DRTFs such as *Nfatc2* and *Egr1* (Figure 7B). Acadm and Echs1 were identified as the increased DEMEs common both in the liver and skeletal muscle (Figures 7A and 7B). These results suggest that the fatty acid degradation pathway is potentially activated at enzyme expression level both in liver and skeletal muscle.

To explore ketone body cycle in *ob*/*ob* mice, we added the genes for the monocarboxylate transporters *Slc16a7* to skeletal muscle and *Slc16a6* to liver (Figure 7C) (Newman and Verdin, 2014). *Slc16a7* expression decreased in skeletal muscle, suggesting reduced capacity for ketone body transport. In contrast, *Slc16a6* expression increased in liver, consistent with the previous report using overnight-fasted *db*/*db* mice (Kim et al., 2016), suggesting an increased capacity for ketone body transport. We found that the DEMEs responsible for fatty acid degradation (Figure 7A) and ketone bodies (acetoacetate and 3-OH butyrate) production, such as Hmgcl (3-hydroxy-3-methylglutaryl-CoA lyase), Bdh1 (D-beta-hydroxybutyrate dehydrogenase), and a rate-limiting enzyme of ketone body synthesis Hmgcs2 (3-hydroxy-3-methylglutaryl-CoA synthase 2), increased in liver of *ob*/*ob* mice (Figure 7C). This result suggests that the synthesis of 3-OH butyrate is potentially activated in liver of *ob*/*ob* mice, although the metabolites for ketone body production, such as acetyl-CoA and 3-OH butyrate, did not significantly change. Further study is necessary to address whether the synthesis rate of 3-OH butyrate is activated in liver of *ob*/*ob* mice. Skeletal muscle exhibited reduced capacity for ketone body uptake (decreased *Slc16a7* expression) and ketone body metabolism as suggested by decreased Bdh1 (Figure 7C). Despite this increased capacity to produce and release the ketone body 3-OH butyrate by the liver and the decreased use of this ketone body by skeletal muscle from *ob*/*ob* mice, blood concentrations of 3-OH butyrate were unchanged from WT mice.

DISCUSSION

We measured multiple omic data—transcriptomic, proteomic, and metabolomic—in liver and skeletal muscle of WT and *ob*/*ob* mice during a fasting state and identified differentially expressed molecules that significantly changed in *ob*/*ob* mice relative to WT in each omic layer and connected these layers with differential regulations. From this large set of data, we extracted differentially expressed molecules and differential regulations that are involved in metabolic reactions and constructed a trans-omic network for liver and a network for skeletal muscle of the differentially regulated metabolic reactions. By integrating the trans-omic networks in liver and skeletal muscle with metabolomic data from blood, we explored the potential mechanisms of dysfunction of three inter-organ metabolic cycles: glucose-alanine, glucose-lactate, and ketone bodies.

We provided the potential mechanisms of obesity-associated dysfunctions and dysregulations of inter-organ metabolic cycles of glucose-alanine and glucose-lactate: (1) activation of the gluconeogenesis pathway both from alanine and lactate by increased enzyme expression in the liver and (2) impaired glycolysis by decreased enzyme expression in skeletal muscle. In the activation of gluconeogenesis pathway in liver of *ob*/*ob* mice, expression of *Gpt2* and *Ldha*, encoding enzymes that catalyze alanine and lactate to pyruvate, respectively, and of *Asct2*, encoding an alanine transporter, were upregulated by the common DRTF, *Pparg*, suggesting a mechanism for coordinated activation of these dysregulated processes in liver. Taken together, the data suggested that dysregulations of the glucose-alanine and glucose-lactate cycles involve activation of gluconeogenesis in liver and inhibition of glycolysis in skeletal muscle, which may contribute to hyperglycemia of *ob*/*ob* mice. However, further studies are required to elucidate the causal relationship between obesity-associated changes of the activation status of pathways and dysregulation of the inter-organ metabolic cycles. Moreover, we found that blood glucose and phosphorylation of As160 in skeletal muscle increased, whereas downstream glycolytic metabolites (G6P to PEP) decreased, suggesting that Glut4 translocation to plasma membrane, which is downstream of As160, may be impaired in *ob*/*ob* mice. This may be the key mechanism of insulin resistance in skeletal muscle of *ob*/*ob* mice.

We provided the potential mechanisms of dysregulations of the inter-organ metabolic cycle of ketone body; both the production of a ketone body, 3-OH butyrate, in liver and its release from the liver into

the blood increased in *ob*/*ob* mice, suggesting that excess lipids are converted into this ketone body in the liver of *ob*/*ob* mice. In addition, the expression of the gene encoding the 3-OH butyrate transporter in skeletal muscle of *ob*/*ob* mice decreased. However, the amount of 3-OH butyrate in the blood was similar between WT and *ob*/*ob* mice, suggesting that organs other than skeletal muscle take up this ketone body, preventing its accumulation in the blood despite increased production and release by the liver. In skeletal muscle of *ob*/*ob* mice, the expression of ketone body transporter and metabolic enzyme and the amount of 3-OH butyrate decreased, despite activation of enzymes involved in fatty acid degradation in skeletal muscle. These results suggest that fatty acids instead of ketone bodies were metabolized to produce acetyl-CoA in skeletal muscle. In skeletal muscle from *ob*/*ob* mice, 5 of the 8 increased DEMEs involved in fatty acid degradation were not upregulated at the transcript level (see Figure 7B), suggesting that the increased abundance of these enzymes may be controlled by the modulation of protein turnover.

The increased DRTF *Klf4* regulated the expression of the increased DEGs encoding metabolic enzymes involved in fatty acid degradation (*Ascl5*, *Acadm*, *Echs1*, and *Acaa1b*) and of *Hmgcl* (encoding HMG-CoA lyase involved in ketone body synthesis) in liver of *ob*/*ob* mice. Klf4 is a crucial regulator of mitochondrial homeostasis in cardiac muscle (Liao et al., 2015), but its role in organismal or liver metabolism is still largely unknown. Klf4 may be an important regulator contributing to ketone body production in liver of *ob*/*ob* mice.

In the trans-omic network in the liver, the activating regulation by DEMEs and the inhibiting allosteric regulation by the DEMs counteract each other, implying that the liver may adapt to obesity-induced changes in metabolites with compensatory increases in metabolic enzymes induced by increased gene expression. Expression of many of the increased DEMEs were also regulated at the gene expression level by *Pparg*, *Srebf1*, *Klf4*, and *Esr1*. Both Pparg and Srebp1 are key regulators of hepatic lipid metabolism, and those TFs are highly expressed in liver of obese individuals (Bedoucha et al., 2001; Shimomura et al., 1999; Jeon and Osborne, 2012). Consistent with the earlier observations, we also identified increased expression of *Pparg* and *Srebf1* in liver of *ob*/*ob* mice and increased activation of lipid metabolic pathways regulated by their target genes. *Pparg* and *Srebf1* also activated genes involved in carbohydrate metabolism, including those in the glycogen, TCA cycle, and glycolysis and gluconeogenesis pathways, in the *ob*/*ob* mice, suggesting that these DRTFs coordinate altered lipid and carbohydrate metabolism in obesity. These results provide a potential transcriptional mechanism for the increased expression of genes encoding metabolic enzymes involved in carbohydrate metabolism that is associated with insulin resistance in obesity (Guo, 2014; Roden and Shulman, 2019).

Changes in DEMs in liver and skeletal muscle of *ob*/*ob* mice, as well as in the blood, suggested higher oxidative stress in the *ob*/*ob* mice. In skeletal muscle, we identified anserine and carnosine, which are dipeptides composed of beta-alanine and histidine, as decreased DEMs in skeletal muscle of *ob*/*ob* mice. Anserine and carnosine are antioxidant factors involved in the degradation of lipid peroxide and are abundant in skeletal muscle (Kohen et al., 1988; Boldyrev et al., 2013). The decrease in these metabolites in *ob*/*ob* mice suggested that lipid peroxide may accumulate in skeletal muscle cells of *ob*/*ob* mice. In addition, both glutathione (GSH) and GSSG increased in the liver, and GSSG increased in the blood of *ob*/*ob* mice, which may reflect the oxidative stress associated with higher energy production in *ob*/*ob* mice (Tangvarasittichai, 2015).

To comprehensively elucidate potential regulatory mechanisms of systemic metabolic homeostasis, inter-organ metabolic cycles for additional key metabolic organs should be evaluated. Adipose tissue is an obvious choice. We analyzed the trans-omic network of insulin signaling in differentiated 3T3 adipocytes (Krycer et al., 2017; Quek et al., 2020; Ohno et al., 2020). We intend to apply our trans-omic approach to investigating inter-organ metabolic cycles between adipose tissue and other organs *in vivo* in the future.

Several multi-omic studies, including our previous trans-omic works, examined the effects of obesity on metabolism in human or animal models (Kokaji et al., 2020; Parks et al., 2015; Soltis et al., 2017; Williams et al., 2016). Soltis et al. performed epigenomic, transcriptomic, proteomic, and metabolomic analyses of liver from mice fed a normal or high-fat diet. Some of the differentially expressed molecules associated with high-fat diet in their study were consistent with our results from *ob*/*ob* mice in previous study (Kokaji et al., 2020) and the present study. In the amount of metabolite, GSH and lactate increased, and Gly decreased in the liver of both obese mice (Kokaji et al., 2020; Soltis et al., 2017). In the expression of genes, the increased DEGs in both obese mice were enriched in glycolysis/gluconeogenesis and steroid synthesis,

whereas the decreased DEGs in both obese mice were enriched in 4 amino acid metabolic pathways such as Ala, Asp, and Glu metabolism and Gly, Ser, and Thr metabolism (Kokaji et al., 2020; Soltis et al., 2017). Besides, we compared our DETFs with TFs in liver of high-fat diet-induced obese mice (Soltis et al., 2017) (Figures 2F and S13). We found that more than half of the DETF were similarly regulated in the high-fat diet-induced mice (3 out of 4 increased DETFs and 3 out of 6 decreased DETFs). In particular, the increases of *Pparg*, *Srebf1*, and *Esr1* and the decreases of *Zfx*, *Gtf2ird1*, and *Trim28* consistently occurred both in their high-fat-diet-fed mice and in our *ob*/*ob* mice fed with normal diet. Because these changes occurred in response to both high-fat diet and the absence of leptin (*ob*/*ob*), this result indicates that these DETFs are associated with obesity, not with leptin deficiency nor with the content of diet. The present study extends the previous multi-omic and trans-omic studies by including skeletal muscle and evaluating inter-organ metabolic cycles, thereby providing distinct insights into dysregulated metabolism in obesity.

The analysis of trans-omic networks for differentially regulated metabolic reactions can be applied to elucidate trans-omic network using pathological models other than obesity and potentially contribute to the discovery of novel therapeutic targets. In the future, assembling larger-scale trans-omic networks for differentially regulated metabolic reactions between healthy and obese individuals by adding to multi-omic datasets will uncover the whole picture of the effects of obesity on systemic metabolic homeostasis.

Limitations of the study

The potential mechanisms of the dysregulation of the inter-organ metabolic cycles in this study may not reflect direct causal relationship and should be validated by further experiments in the future. Limitations of our study include that we evaluated only liver and skeletal muscle and only at a single time point of fasting. More detailed investigation of the effects of obesity on metabolite exchange across each organ will require the acquisition of metabolite time series data using isotope tracers (Fernández-García et al., 2020), along with acquisition of transcriptomic and proteomic data at multiple time points. The sample size of lipidome (n = 3) is relatively small compared with other omic analyses, and the statistical power is low for lipidomic analysis. For this reason, we did not include the lipidomic data in the trans-omic networks (Figure 4). In addition, we focused on metabolic reactions. However, perturbations in liver and skeletal muscle of *ob*/*ob* mice are not limited to metabolism. These mice also exhibit increased chronic inflammation or disrupted organ architecture (Cohen et al., 2011). We need to analyze other perturbed cellular functions than metabolism for comprehensive understanding of systemic changes in *ob*/*ob* mice. For example, skeletal muscle is primarily a contractile organ. Thus, these cells may adapt to obesity through changes in non-metabolic cellular functions, such as muscle contraction. Indeed, we found pathways involved in contractile function, such as the regulation of actin cytoskeleton, from pathway enrichment analysis in DEGs in skeletal muscle (Table S2) and identified increased DEPs associated with muscle contraction, such as Myh2 and Myh7 (see Figure 2D). There are two types of regulation of TFs: regulation by expression change and regulation by posttranslational modifications including, phosphorylation (differentially phosphorylated TFs (DPTFs)). In this study, we identified DETFs using RNA-seq and included only pFoxo1 as a DPTF based on the literature. In the future, the phosphoproteomic measurement will allow us to comprehensively identify DPTFs according to our methods (Yugi et al., 2014; Kawata et al., 2019). Identification of both DETFs and DPTFs will enable us to examine how much of gene expression is controlled by DETFs and DPTFs in *ob*/*ob* mice. Thus, large-scale measurements of phosphorylation levels of metabolic molecules by the phosphoproteomics are required (Yugi et al., 2014; Kawata et al., 2019; Humphrey et al., 2013). We also only evaluated TFs as upstream regulators of the gene expression network. Yet, considerations of epigenomic controls, such as histone modifications and DNA methylation, will provide us with further insight into the organ-specific traits of gene expression regulatory network (Ahrens et al., 2013; Kirchner et al., 2016). RNA-mediated regulation, such as through miRNA or lncRNA, is also likely and will need to be added to the regulatory network to enable comprehensive analyses.

Resource availability

Lead contact

Further information and requests for resources and reagents should be directed to and will be fulfilled by the lead contact, Shinya Kuroda (skuroda@bs.s.u-tokyo.ac.jp).

Materials availability

This study did not generate any new material.

Data and code availability

The accession number for the sequencing data of the liver and skeleltal muscle reported in this paper is the DNA DataBank of Japan Sequence Read Archive (DRA) (www.ddbj.nig.ac.jp/): DRA008416, DRA010972. The accession number for the data of proteome analysis reported in this paper is the ProteomeXchange Consortium (http://proteomecentral.proteomexchange.org) via the JPOST partner repository: PXD020656. All other data are available with the published article. The code used for the analysis in this paper is available upon request.

METHODS

All methods can be found in the accompanying transparent methods supplemental file.

SUPPLEMENTAL INFORMATION

Supplemental information can be found online at https://doi.org/10.1016/j.isci.2021.102217.

ACKNOWLEDGMENTS

We thank Maki Ohishi, Ayano Ueno, Keiko Endo, Sanae Ashitani, Keiko Kato, and Kaori Saitoh (Keio University) for their technical assistance with metabolomic analysis using CE-MS and our laboratory members for critically reading this manuscript and for their technical assistance with the experiments. The computational analysis of this work was performed in part with support of the super computer system of National Institute of Genetics (NIG), Research Organization of Information and Systems (ROIS). This manuscript was edited by Nancy R. Gough (BioSerendipity, LLC).

This work was supported by the Creation of Fundamental Technologies for Understanding and Control of Biosystem Dynamics, CREST (JPMJCR12W3) from the Japan Science and Technology Agency (JST), by the Japan Society for the Promotion of Science (JSPS) KAKENHI Grant Number JP17H06300, JP17H06299, JP18H03979, and by The Uehara Memorial Foundation. R.E. receives funding from JSPS KAKENHI Grant Number JP19J10234. K.Y. receives funding from JSPS KAKENHI Grant Number JP15H05582, JP18H05431, and ''Creation of Innovative Technology for Medical Applications Based on the Global Analyses and Regulation of Disease-Related Metabolites'', PRESTO (JPMJPR1538) from JST. S.O. receives funding from a Grant-in-Aid for Young Scientists (B) (JP17K14864). M.F. receives funding from JSPS KAKENHI Grant Number JP19K20382 and JP16K12508. T.T. was supported by JSPS KAKENHI Grant Number JP19K24361, JP20K19915. H.O. was supported by JSPS KAKENHI Grant Number JP19H03696, JP19K20394. H. I. was supported by JSPS KAKENHI Grant Number JP18KT0020, JP17H05499, and by Adaptable and Seamless Technology transfer Program through Target-driven R&D (A-STEP) from JST. S.U. was supported by JSPS KAKENHI Grant Number JP18H02431, JP20H04847. H.K. was supported by JSPS KAKENHI Grant Number JP16H06577. Y.S. was supported by the JSPS KAKENHI Grant Number JP17H06306. K.I.N. was supported by the JSPS KAKENHI Grant Number JP17H06301, JP18H05215. A.H. was supported by the JSPS KAKENHI Grant Number JP18H04804. T.S. receives funding from the AMED-CREST from the Japan Agency for Medical Research and Development (AMED) under Grant Number JP18gm0710003.

AUTHORS CONTRIBUTION

R.E., T.K., A. Hatano, M.E., K.M., H.K., M.M., and K.I.N. designed and performed the animal experiments, enzymatic assays, and western blotting measurements; A. Hirayama and T.S. performed metabolomic analysis using CE-MS; Y.S. performed transcriptomic analysis using RNA-seq; R.E., T.K., K.Y., S.O., M.F., K.H., S. Uematsu, A.T., Y.B., Y.P., T.T., H.O., and S. Uda. performed trans-omic analysis; writing group consisted of R.E., T.K., A. Hatano, H.I., and S.K.; and the study was conceived and supervised by R.E. and S.K.

DECLARATION OF INTERESTS

The authors declare no competing interests.

Received: December 2, 2020
Revised: February 1, 2021
Accepted: February 18, 2021
Published: March 19, 2021

REFERENCES

Ahrens, M., Ammerpohl, O., von Schönfels, W., Kolarova, J., Bens, S., Itzel, T., Teufel, A., Herrmann, A., Brosch, M., Hinrichsen, H., et al. (2013). DNA methylation analysis in nonalcoholic fatty liver disease suggests distinct disease-specific and remodeling signatures after bariatric surgery. Cell Metab. *18*, 296–302.

Barthel, A., Schmoll, D., and Unterman, T. (2005). FoxO proteins in insulin action and metabolism. Trends Endocrinol. Metab. *16*, 183–189.

Basu, R., Chandramouli, V., Dicke, B., Landau, B., and Rizza, R. (2005). Obesity and type 2 diabetes impair insulin-induced suppression of glycogenolysis as well as gluconeogenesis. Diabetes *54*, 1942–1948.

Bedoucha, M., Atzpodien, E., and Boelsterli, U.A. (2001). Diabetic KKAy mice exhibit increased hepatic PPARγ1 gene expression and develop hepatic steatosis upon chronic treatment with antidiabetic thiazolidinediones. J. Hepatol. *35*, 17–23.

Boldyrev, A.A., Aldini, G., and Derave, W. (2013). Physiology and pathophysiology of carnosine. Physiol. Rev. *93*, 1803–1845.

Cahill, G.F., Herrera, M.G., Morgan, A.P., Soeldner, J.S., Steinke, J., Levy, P.L., Reichard, G.A., and Kipnis, D.M. (1966). Hormone-fuel interrelationships during fasting. J. Clin. Invest. *45*, 1751–1769.

Castillo-Armengol, J., Fajas, L., and Lopez-Mejia, I.C. (2019). Inter-organ communication: a gatekeeper for metabolic health. EMBO Rep. *20*, e47903.

Clementi, A., Gaudy, A., Zimmers, T., Koniaris, L., and Mooney, R. (2011). Deletion of interleukin-6 improves pyruvate tolerance without altering hepatic insulin signaling in the leptin receptor–deficient mouse. Metabolism *60*, 1610–1619.

Cohen, J.C., Horton, J.D., and Hobbs, H.H. (2011). Human fatty liver disease: old questions and new insights. Science *332*, 1519–1523.

Cori, C.F., and Cori, G.T. (1929). Glycogen formation in the liver from d- and l-lactic acid. J. Biol. Chem. *81*, 389–403.

Dashty, M. (2013). A quick look at biochemistry: carbohydrate metabolism. Clin. Biochem. *46*, 1339–1352.

Felig, P. (1973). The glucose-alanine cycle. Metabolism *22*, 179–207.

Fernández-García, J., Altea-Manzano, P., Pranzini, E., and Fendt, S.-M. (2020). Stable isotopes for tracing mammalian-cell metabolism in vivo. Trends Biochem. Sci. *45*, 185–201.

Freidman, N., Chen, I., Wu, Q., Briot, C., Holst, J., Font, J., Vandenberg, R., and Ryan, R. (2020). Amino acid transporters and exchangers from the SLC1A family: structure, mechanism and roles in physiology and cancer. Neurochem. Res. *45*, 1268–1286.

Gamberucci, A., Marcolongo, P., Fulceri, R., Giunti, R., Watkins, S.L., Waddell, I.D., Burchell, A., and Benedetti, A. (1996). Low levels of glucose-6-phosphate hydrolysis in the sarcoplasmic reticulum of skeletal muscle. Mol. Membr. Biol. *13*, 103–108.

Gancheva, S., Jelenik, T., Álvarez-Hernández, E., and Roden, M. (2018). Interorgan metabolic crosstalk in human insulin resistance. Physiol. Rev. *98*, 1371–1415.

Guo, S. (2014). Insulin signaling, resistance, and metabolic syndrome: insights from mouse models into disease mechanisms. J. Endocrinol. *220*, T1–T23.

Halestrap, A. (2013). The SLC16 gene family – structure, role and regulation in health and disease. Mol. Aspects Med. *34*, 337–349.

Hardie, D.G. (2011). AMP-activated protein kinase—an energy sensor that regulates all aspects of cell function. Genes Dev. *25*, 1895–1908.

Huang, S., and Czech, M.P. (2007). The GLUT4 glucose transporter. Cell Metab. *5*, 237–252.

Humphrey, S.J., Yang, G., Yang, P., Fazakerley, D.J., Stöckli, J., Yang, J.Y., and James, D.E. (2013). Dynamic adipocyte phosphoproteome reveals that Akt directly regulates mTORC2. Cell Metab. *17*, 1009–1020.

Ingalls, A.M., Dickie, M.M., and Snell, G.D. (1950). OBESE, a new mutation in the house mouse. J. Hered. *41*, 317–318.

Jeon, T.-I., and Osborne, T.F. (2012). SREBPs: metabolic integrators in physiology and metabolism. Trends Endocrinol. Metab. *23*, 65–72.

Jeske, L., Placzek, S., Schomburg, I., Chang, A., and Schomburg, D. (2019). BRENDA in 2019: a European ELIXIR core data resource. Nucleic Acids Res. *47*, D542–D549.

Kahn, S.E., Hull, R.L., and Utzschneider, K.M. (2006). Mechanisms linking obesity to insulin resistance and type 2 diabetes. Nature *444*, 840–846.

Kandasamy, P., Gyimesi, G., Kanai, Y., and Hediger, M.A. (2018). Amino acid transporters revisited: new views in health and disease. Trends Biochem. Sci. *43*, 752–789.

Kanehisa, M., Furumichi, M., Tanabe, M., Sato, Y., and Morishima, K. (2017). KEGG: new perspectives on genomes, pathways, diseases and drugs. Nucleic Acids Res. *45*, D353–D361.

Kawata, K., Hatano, A., Yugi, K., Kubota, H., Sano, T., Fujii, M., Tomizawa, Y., Kokaji, T., Tanaka, K.Y., Uda, S., et al. (2018). Trans-omic analysis reveals selective responses to induced and basal insulin across signaling, transcriptional, and metabolic networks. iScience *7*, 212–229.

Kawata, K., Yugi, K., Hatano, A., Kokaji, T., Tomizawa, Y., Fujii, M., Uda, S., Kubota, H., Matsumoto, M., Nakayama, K.I., et al. (2019). Reconstruction of global regulatory network from signaling to cellular functions using phosphoproteomic data. Genes Cells *24*, 82–93.

Kel, A.E., Gößling, E., Reuter, I., Cheremushkin, E., Kel-Margoulis, O.V., and Wingender, E. (2003). MATCHTM: a tool for searching transcription factor binding sites in DNA sequences. Nucleic Acids Res. *31*, 3576–3579.

Kim, K.E., Jung, Y., Min, S., Nam, M., Heo, R.W., Jeon, B.T., Song, D.H., Yi, C., Jeong, E.A., Kim, H., et al. (2016). Caloric restriction of db/db mice reverts hepatic steatosis and body weight with divergent hepatic metabolism. Sci. Rep. *6*, 30111.

Kirchner, H., Sinha, I., Gao, H., Ruby, M.A., Schönke, M., Lindvall, J.M., Barrès, R., Krook, A., Näslund, E., Dahlman-Wright, K., et al. (2016). Altered DNA methylation of glycolytic and lipogenic genes in liver from obese and type 2 diabetic patients. Mol. Metab. *5*, 171–183.

Kohen, R., Yamamoto, Y., Cundy, K.C., and Ames, B.N. (1988). Antioxidant activity of carnosine, homocarnosine, and anserine present in muscle and brain. PNAS *85*, 3175–3179.

Kokaji, T., Hatano, A., Ito, Y., Yugi, K., Eto, M., Morita, K., Ohno, S., Fujii, M., Hironaka, K., Egami, R., et al. (2020). Transomics analysis reveals allosteric and gene regulation axes for altered hepatic glucose-responsive metabolism in obesity. Sci. Signal. *13*, eaaz1236.

Krycer, J.R., Yugi, K., Hirayama, A., Fazakerley, D.J., Quek, L.-E., Scalzo, R., Ohno, S., Hodson, M.P., Ikeda, S., Shoji, F., et al. (2017). Dynamic metabolomics reveals that insulin primes the adipocyte for glucose metabolism. Cell Rep. *21*, 3536–3547.

Lehninger, A.L., Nelson, D.L., and Cox, M.M. (2005). Lehninger Principles of Biochemistry (W.H. Freeman).

Liao, X., Zhang, R., Lu, Y., Prosdocimo, D.A., Sangwung, P., Zhang, L., Zhou, G., Anand, P., Lai, L., Leone, T.C., et al. (2015). Kruppel-like factor 4 is critical for transcriptional control of cardiac mitochondrial homeostasis. J. Clin. Invest. *125*, 3461–3476.

Lindström, P. (2007). The physiology of obese-hyperglycemic mice [ob/ob mice]. ScientificWorldJournal *7*, 666–685.

Liu, S., Liu, Q., Sun, S., Jiang, Q., Peng, J., and Shen, Z. (2012). The application of 2-NBDG as a fluorescent tracer for assessing hepatic glucose production in mice during hyperinsulinemic euglycemic clamp. Acta Pharmaceutica Sinica B *2*, 403–410.

Lusis, A.J., Attie, A.D., and Reue, K. (2008). Metabolic syndrome: from epidemiology to systems biology. Nat. Rev. Genet. *9*, 819–830.

Mastrocola, R., Collino, M., Nigro, D., Chiazza, F., D'Antona, G., Aragno, M., and Minetto, M.A. (2015). Accumulation of advanced glycation end-products and activation of the SCAP/SREBP lipogenetic pathway occur in diet-induced obese mouse skeletal muscle. PLoS One *10*, e0119587.

Matys, V., Kel-Margoulis, O.V., Fricke, E., Liebich, I., Land, S., Barre-Dirrie, A., Reuter, I., Chekmenev, D., Krull, M., Hornischer, K., et al. (2006). TRANSFAC® and its module TRANSCompel®: transcriptional gene regulation in eukaryotes. Nucleic Acids Res. *34*, D108–D110.

Muoio, D.M., and Newgard, C.B. (2008). Molecular and metabolic mechanisms of insulin resistance and β-cell failure in type 2 diabetes. Nat. Rev. Mol. Cell Biol. *9*, 193–205.

Nesteruk, M., Hennig, E.E., Mikula, M., Karczmarski, J., Dzwonek, A., Goryca, K., Rubel, T., Paziewska, A., Woszczynski, M., Ledwon, J., et al. (2014). Mitochondrial-related proteomic changes during obesity and fasting in mice are greater in the liver than skeletal muscles. Funct. Integr. Genomics *14*, 245–259.

Newman, J.C., and Verdin, E. (2014). Ketone bodies as signaling metabolites. Trends Endocrinol. Metab. *25*, 42–52.

Ohno, S., Quek, L.-E., Krycer, J.R., Yugi, K., Hirayama, A., Ikeda, S., Shoji, F., Suzuki, K., Soga, T., James, D.E., et al. (2020). Kinetic trans-omic analysis reveals key regulatory mechanisms for insulin-regulated glucose metabolism in adipocytes. iScience *23*, 101479.

Ohshima, K., Shargill, N.S., Chan, T.M., and Bray, G.A. (1984). Adrenalectomy reverses insulin resistance in muscle from obese (ob/ob) mice. Am. J. Physiol. Endocrinol. Metab. *246*, E193–E197.

Parks, B.W., Sallam, T., Mehrabian, M., Psychogios, N., Hui, S.T., Norheim, F., Castellani, L.W., Rau, C.D., Pan, C., Phun, J., et al. (2015). Genetic architecture of insulin resistance in the mouse. Cell Metab. *21*, 334–347.

Perfield, J.W., Ortinau, L.C., Pickering, R.T., Ruebel, M.L., Meers, G.M., and Rector, R.S. (2013). Altered hepatic lipid metabolism contributes to nonalcoholic fatty liver disease in leptin-deficient ob/ob mice. J. Obes. *2013*, 296537.

Quek, L.-E., Krycer, J.R., Ohno, S., Yugi, K., Fazakerley, D.J., Scalzo, R., Elkington, S.D., Dai, Z., Hirayama, A., Ikeda, S., et al. (2020). Dynamic 13C flux analysis captures the reorganization of adipocyte glucose metabolism in response to insulin. iScience *23*, 100855.

Roden, M., and Shulman, G.I. (2019). The integrative biology of type 2 diabetes. Nature *576*, 51–60.

Samuel, V.T., and Shulman, G.I. (2016). The pathogenesis of insulin resistance: integrating signaling pathways and substrate flux. J. Clin. Invest. *126*, 12–22.

Sarabhai, T., and Roden, M. (2019). Hungry for your alanine: when liver depends on muscle proteolysis. J. Clin. Invest. *129*, 4563–4566.

Satapati, S., Sunny, N.E., Kucejova, B., Fu, X., He, T.T., Méndez-Lucas, A., Shelton, J.M., Perales, J.C., Browning, J.D., and Burgess, S.C. (2012). Elevated TCA cycle function in the pathology of diet-induced hepatic insulin resistance and fatty liver [S]. J. Lipid Res. *53*, 1080–1092.

Schaftingen, E., and Gerin, I. (2002). The glucose-6-phosphatase system. Biochem. J. *362*, 513–532.

Schönke, M., Björnholm, M., Chibalin, A.V., Zierath, J.R., and Deshmukh, A.S. (2018). Proteomics analysis of skeletal muscle from leptin-deficient ob/ob mice reveals adaptive remodeling of metabolic characteristics and fiber type composition. Proteomics *18*, 1700375.

Shannon, C.E., Ragavan, M., Palavicini, J.P., Fourcaudot, M., Bakewell, T.M., Valdez, I.A., Ayala, I., Jin, E.S., Madesh, M., Han, X., et al. (2021). Insulin resistance is mechanistically linked to hepatic mitochondrial remodeling in non-alcoholic fatty liver disease. Mol. Metab. *45*, 101154.

Shimomura, I., Bashmakov, Y., and Horton, J.D. (1999). Increased levels of nuclear SREBP-1c associated with fatty livers in two mouse models of diabetes mellitus. J. Biol. Chem. *274*, 30028–30032.

Soltis, A.R., Kennedy, N.J., Xin, X., Zhou, F., Ficarro, S.B., Yap, Y.S., Matthews, B.J., Lauffenburger, D.A., White, F.M., Marto, J.A., et al. (2017). Hepatic dysfunction caused by consumption of a high-fat diet. Cell Rep. *21*, 3317–3328.

Soto, M., Orliaguet, L., Reyzer, M.L., Manier, M.L., Caprioli, R.M., and Kahn, C.R. (2018). Pyruvate induces torpor in obese mice. PNAS *115*, 810–815.

Tangvarasittichai, S. (2015). Oxidative stress, insulin resistance, dyslipidemia and type 2 diabetes mellitus. World J. Diabetes *6*, 456–480.

Thiel, G., and Cibelli, G. (2002). Regulation of life and death by the zinc finger transcription factor Egr-1. J. Cell Physiol. *193*, 287–292.

Turner, S.M., Linfoot, P.A., Neese, R.A., and Hellerstein, M.K. (2005). Sources of plasma glucose and liver glycogen in fasted ob/ob mice. Acta Diabetol. *42*, 187–193.

Williams, E.G., Wu, Y., Jha, P., Dubuis, S., Blattmann, P., Argmann, C.A., Houten, S.M., Amariuta, T., Wolski, W., Zamboni, N., et al. (2016). Systems proteomics of liver mitochondria function. Science *352*, aad0189.

Yu, X., McCorkle, S., Wang, M., Lee, Y., Li, J., Saha, A.K., Unger, R.H., and Ruderman, N.B. (2004). Leptinomimetic effects of the AMP kinase activator AICAR in leptin-resistant rats: prevention of diabetes and ectopic lipid deposition. Diabetologia *47*, 2012–2021.

Yugi, K., and Kuroda, S. (2017). Metabolism-centric trans-omics. Cell Syst. *4*, 19–20.

Yugi, K., and Kuroda, S. (2018). Metabolism as a signal generator across trans-omic networks at distinct time scales. Curr. Opin. Syst. Biol. *8*, 59–66.

Yugi, K., Kubota, H., Toyoshima, Y., Noguchi, R., Kawata, K., Komori, Y., Uda, S., Kunida, K., Tomizawa, Y., Funato, Y., et al. (2014). Reconstruction of insulin signal flow from phosphoproteome and metabolome data. Cell Rep. *8*, 1171–1183.

Yugi, K., Ohno, S., Krycer, J.R., James, D.E., and Kuroda, S. (2019). Rate-oriented trans-omics: integration of multiple omic data on the basis of reaction kinetics. Curr. Opin. Syst. Biol. *15*, 109–120.

iScience, Volume *24*

Supplemental information

Trans-omic analysis reveals obesity-associated dysregulation of inter-organ metabolic cycles between the liver and skeletal muscle

Riku Egami, Toshiya Kokaji, Atsushi Hatano, Katsuyuki Yugi, Miki Eto, Keigo Morita, Satoshi Ohno, Masashi Fujii, Ken-ichi Hironaka, Saori Uematsu, Akira Terakawa, Yunfan Bai, Yifei Pan, Takaho Tsuchiya, Haruka Ozaki, Hiroshi Inoue, Shinsuke Uda, Hiroyuki Kubota, Yutaka Suzuki, Masaki Matsumoto, Keiichi I. Nakayama, Akiyoshi Hirayama, Tomoyoshi Soga, and Shinya Kuroda

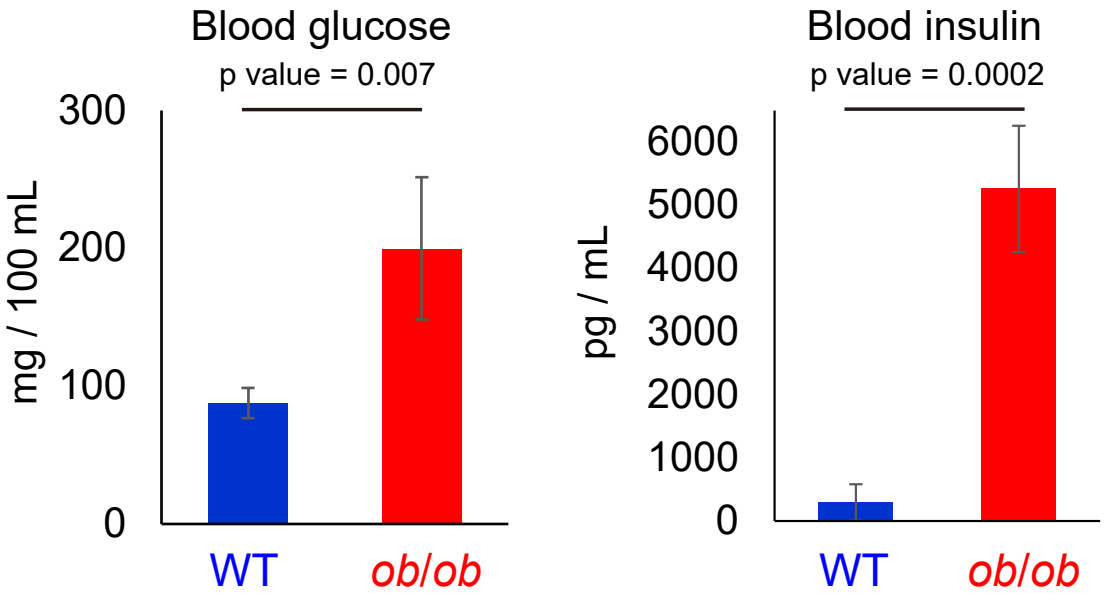

Figure S1. Glucose and Insulin Concentration in the Blood of the Wild-type (WT) and *ob*/*ob* Mice. Related to Figure 1.
The concentrations of glucose (Left) and insulin (Right) in the blood of 16 hours-fasted WT and *ob*/*ob* mice (Kokaji et al., 2020). Blue and red bars represent concentrations in WT and *ob*/*ob* mice, respectively. The means and standard error of the means (SEMs) of 5 mice are shown.

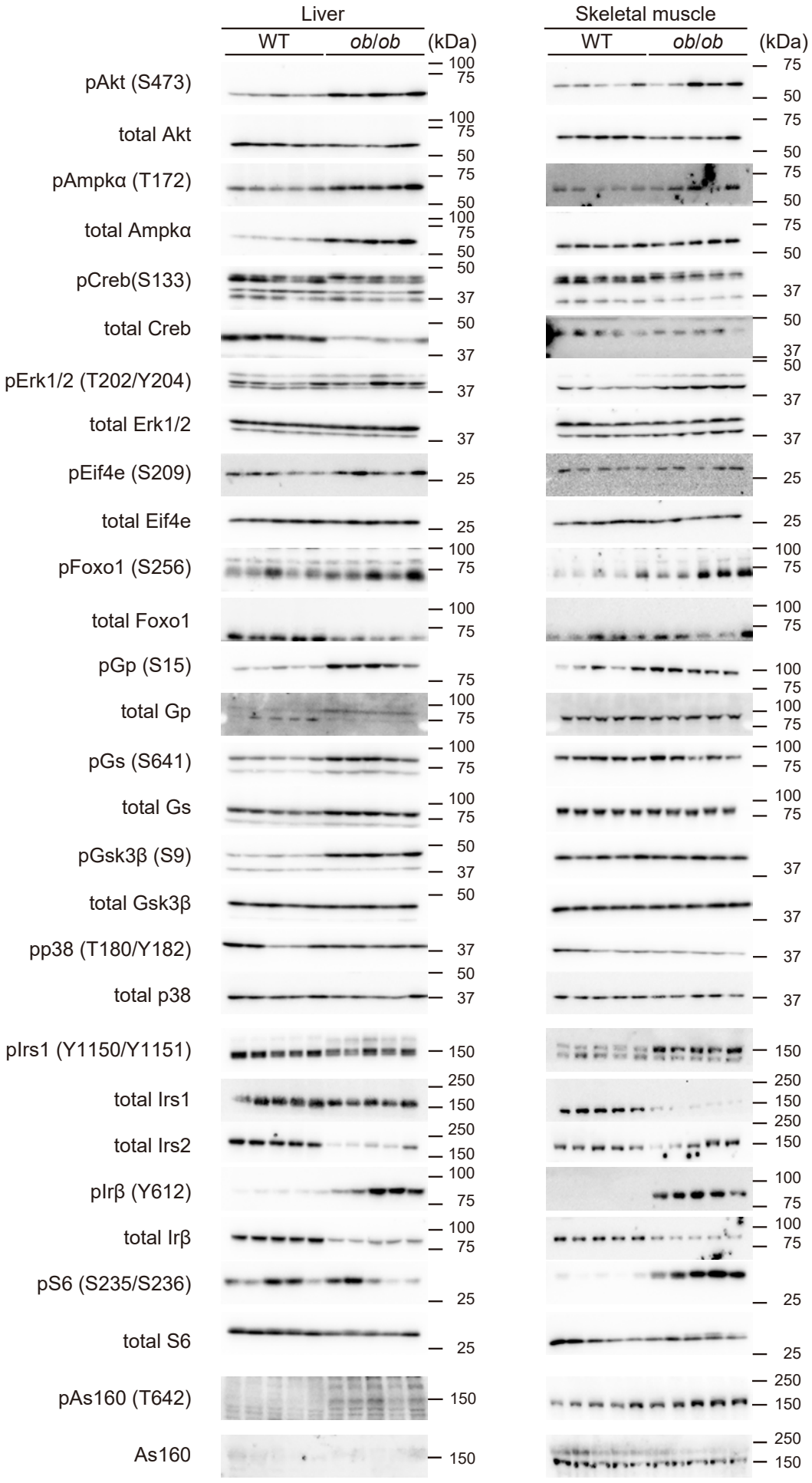

Figure S2. Western Blotting in Liver and Skeletal Muscle. Related to Figure 2.

The amount and phosphorylation of the indicated molecules in the liver and skeletal muscles of WT mice and *ob*/*ob* mice. All western blot data of 5 mice are shown. The unabbreviated name of the molecules can be found in Table S1.

A **Liver**

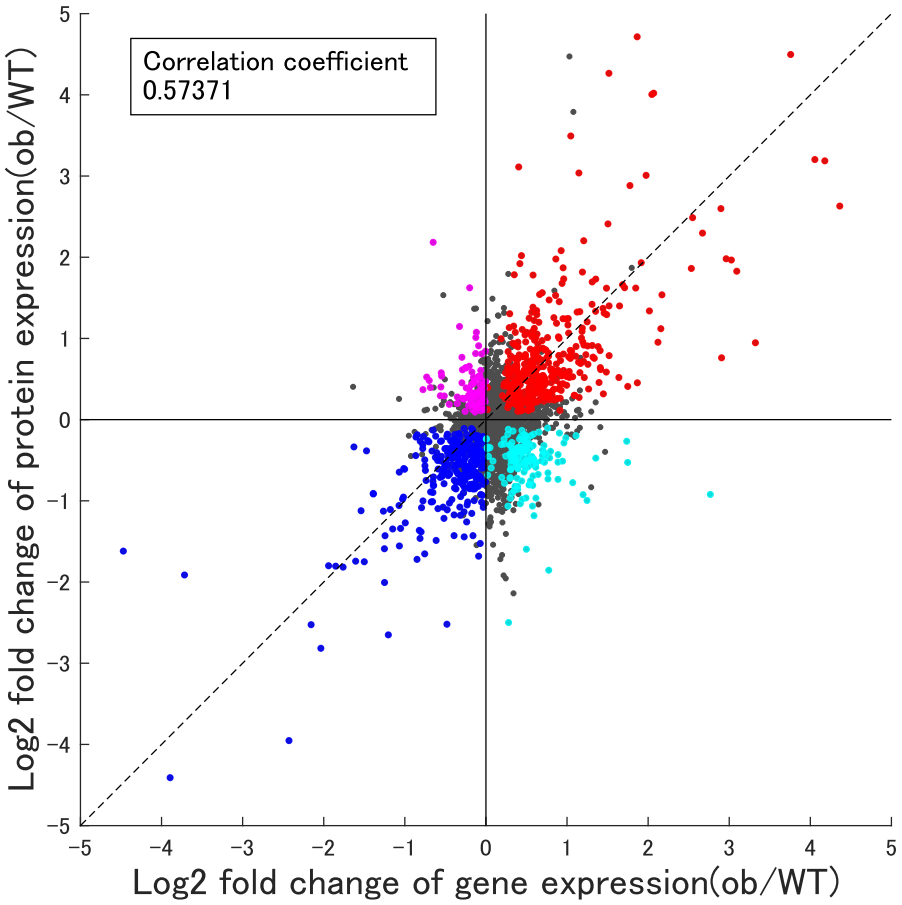

Representative enriched pathways in each category (see also Table S7)

- **Both increased in *ob/ob***
  - Glutathione
  - Glycolysis/Gluconeogenesis
  - Carbon metabolism
  - Pyruvate metabolism
- **Both decreased in *ob/ob***
  - Steroid hormone biosynthesis
  - Spliceosome
  - Retinol
  - Linoleic acid
  - Arachidonic acid
- **Protein increased, transcript decreased in *ob/ob***
  - Proteasome
- **Protein decreased, transcript increased in *ob/ob***
  - Lysosome

B **Skeletal muscle**

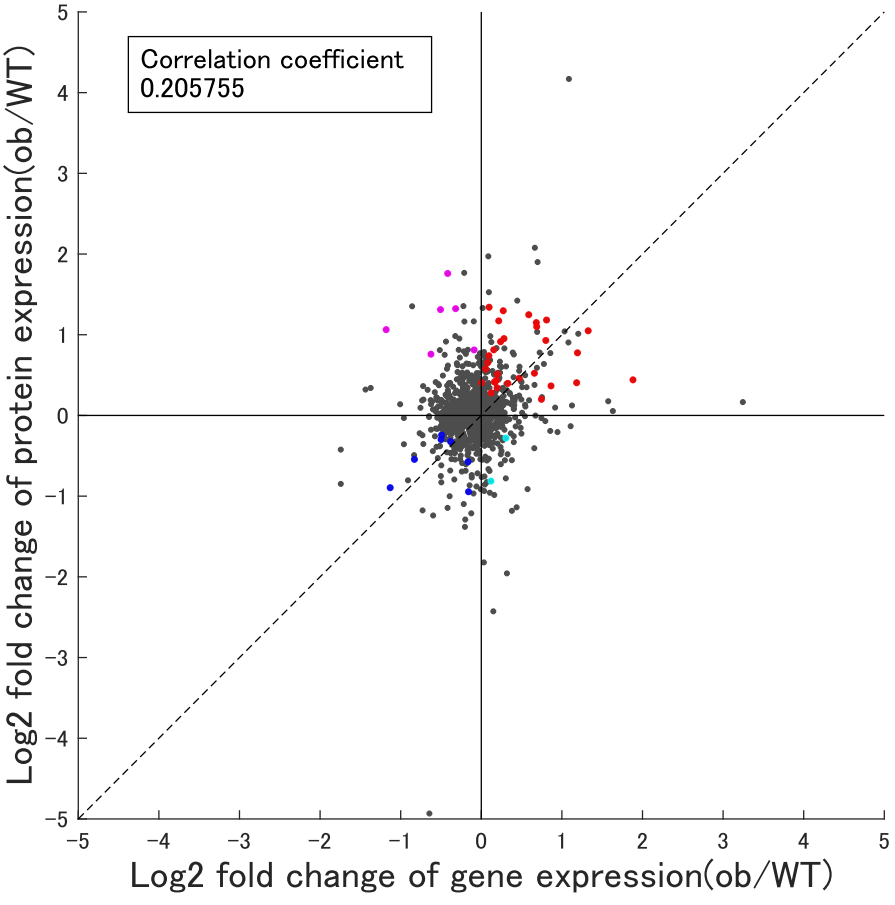

Differentially expressed molecules in each category

- **Both increased in *ob/ob***
  - Ctsb, Gstm2, Gstp1, Casq2, Myoz2, Decr1, Lmcd1, Acat1, Slc25a20, Acaa2, Acadm, Klhl40, Acaca, Hspb7, Myl2, Fhl1, Hadhb, Mybpc1, Myl4 Cyb5r3, Myh7, Csrp3, Myh2, Gyg, Mybph, Suclg2, Pdlim3 Cryab, Neb
- **Both decreased in *ob/ob***
  - Edf1, Hsp90ab1, Myl1, Pgk1, Prxl2b, Serpinb6a, Gapdh
- **Protein increased, transcript decreased in *ob/ob***
  - Hmgcl, Pycrl, Psap, Acot1, Efl1, Txnl1
- **Protein decreased, transcript increased in *ob/ob***
  - Slirp, Col6a3

Figure S3. Integrative Analysis of Proteome and Transcriptome in Liver and Skeletal Muscle. Related to Figure 3.
(A, B) The $\log_2$ fold changes of measured molecules in the liver (A) and skeletal muscle (B) between WT and *ob*/*ob* mice. Each dot on a scatter plot was colored according to the variation of each molecule: red dots, increased molecules in *ob*/*ob* mice both at transcript and protein level; blue dots, decreased molecules in *ob*/*ob* mice both at transcript and protein level; magenta dots, molecules with increased at protein level and decreased at transcript level in *ob*/*ob* mice; cyan dots, molecules with decreased at protein level and increased at transcript level in *ob*/*ob* mice. In analysis of the liver, several representative pathways found by KEGG pathway enrichment analysis are displayed on the right of Figure S3A (see also Table S8). In skeletal muscle, names of gene are displayed on the right of Figure S3B.

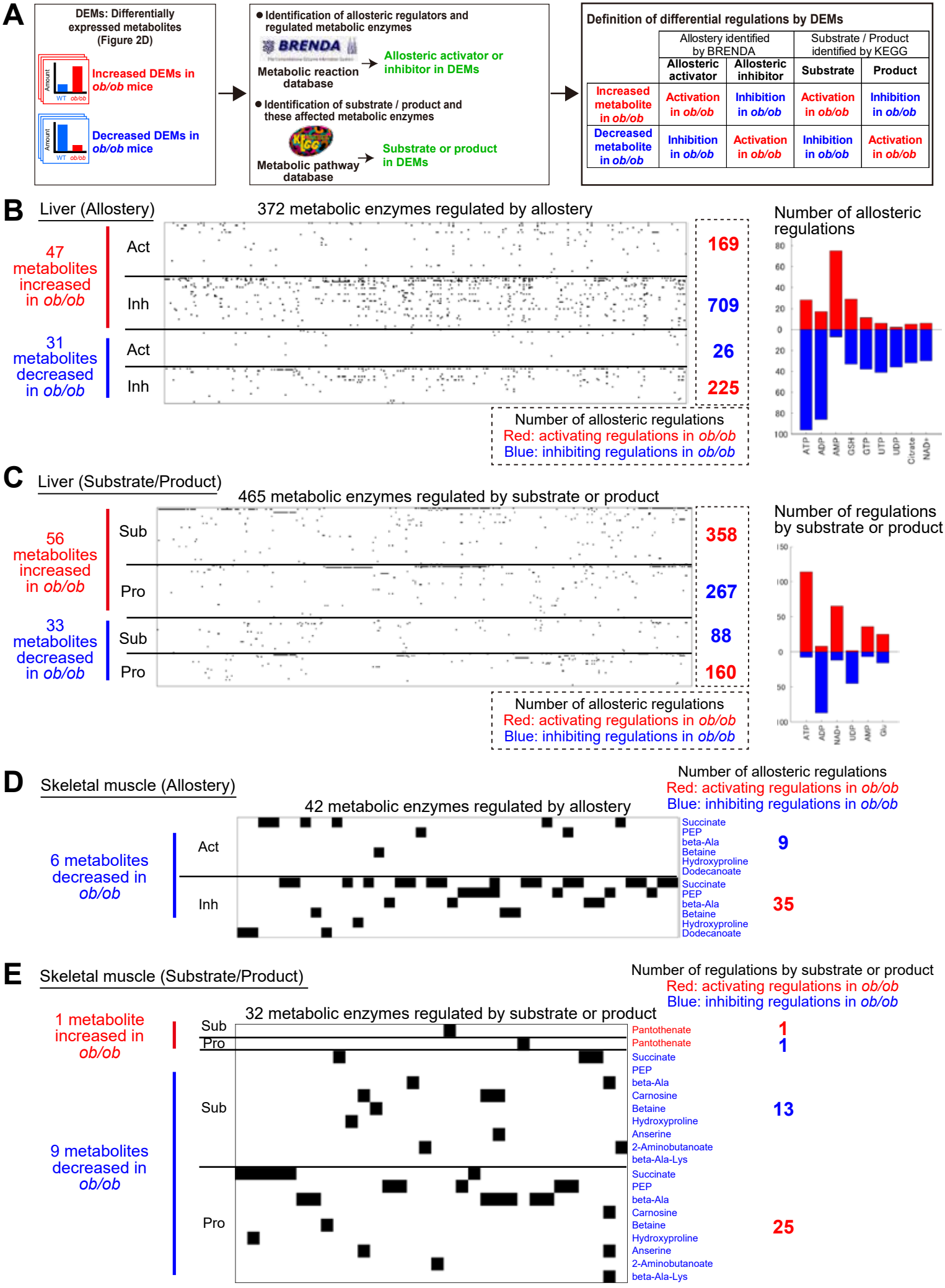
A
DEMs: Differentially expressed metabolites (Figure 2D)
Increased DEMs in ob/ob mice
Decreased DEMs in ob/ob mice
Identification of allosteric regulators and regulated metabolic enzymes
BRENDA
Metabolic reaction database
Allosteric activator or inhibitor in DEMs
Identification of substrate / product and these affected metabolic enzymes
KEGG
Metabolic pathway database
Substrate or product in DEMs
Definition of differential regulations by DEMs
Allostery identified by BRENDA
Substrate / Product identified by KEGG
Allosteric activator
Allosteric inhibitor
Substrate
Product
Increased metabolite in ob/ob
Activation in ob/ob
Inhibition in ob/ob
Activation in ob/ob
Inhibition in ob/ob
Decreased metabolite in ob/ob
Inhibition in ob/ob
Activation in ob/ob
Inhibition in ob/ob
Activation in ob/ob
B
Liver (Allostery)
372 metabolic enzymes regulated by allostery
47 metabolites increased in ob/ob
31 metabolites decreased in ob/ob
Act
Inh
Act
Inh
169
709
26
225
Number of allosteric regulations
Red: activating regulations in ob/ob
Blue: inhibiting regulations in ob/ob
Number of allosteric regulations
ATP
ADP
AMP
GSH
GTP
UTP
UDP
Citrate
NAD+
C
Liver (Substrate/Product)
465 metabolic enzymes regulated by substrate or product
56 metabolites increased in ob/ob
33 metabolites decreased in ob/ob
Sub
Pro
Sub
Pro
358
267
88
160
Number of allosteric regulations
Red: activating regulations in ob/ob
Blue: inhibiting regulations in ob/ob
Number of regulations by substrate or product
ATP
ADP
NAD+
UDP
AMP
Glu
D
Skeletal muscle (Allostery)
42 metabolic enzymes regulated by allostery
6 metabolites decreased in ob/ob
Act
Inh
Number of allosteric regulations
Red: activating regulations in ob/ob
Blue: inhibiting regulations in ob/ob
Succinate
PEP
beta-Ala
Betaine
Hydroxyproline
Dodecanoate
9
Succinate
PEP
beta-Ala
Betaine
Hydroxyproline
Dodecanoate
35
E
Skeletal muscle (Substrate/Product)
32 metabolic enzymes regulated by substrate or product
1 metabolite increased in ob/ob
9 metabolites decreased in ob/ob
Sub
Pro
Sub
Pro
Number of regulations by substrate or product
Red: activating regulations in ob/ob
Blue: inhibiting regulations in ob/ob
Pantothenate
1
Pantothenate
1
Succinate
PEP
beta-Ala
Carnosine
Betaine
Hydroxyproline
Anserine
2-Aminobutanoate
beta-Ala-Lys
13
Succinate
PEP
beta-Ala
Carnosine
Betaine
Hydroxyproline
Anserine
2-Aminobutanoate
beta-Ala-Lys
25

Figure S4. Identification of Allosteric Regulations and Regulation by Substrate or Product in Liver and Skeletal Muscle. Related to Figure 3.

(A) The procedure for identification of differential regulations for metabolic reactions by differentially expressed metabolites (DEMs). We identified allosteric regulations by the allosteric regulators among the DEMs to metabolic reactions using BRENDA (Jeske et al., 2019) and the substrates and products among the DEMs that can affect metabolic reactions using KEGG (Kanehisa et al., 2017). The differential regulations by the DEMs are classified into either activating or inhibiting regulations in *ob*/*ob* mice, which are determined by the combination of the direction of changes of the DEMs (increase or decrease) and of direction of regulation (activator or inhibitor).

(B) Allosteric regulations in the liver to metabolic enzymes by allosteric regulators (Left). The row labels represent each allosteric regulator that increased or decreased in *ob*/*ob* mice and are classified into either activator or inhibitor. The column labels show metabolic enzymes regulated by allostery. A black dot is provided at row *i* column *j* if a metabolic enzyme of column *j* is regulated by an allosteric regulator of row *i*. The number of allosteric regulations to metabolic reaction by the indicated allosteric regulator (Right). Only the regulations whose number is 30 or more are shown in bar plot.

(C) Regulations by substrate or product in the liver to metabolic enzymes by differentially expressed substrate or product (Left). The row labels represent each substrate or product that increased or decreased in *ob*/*ob* mice. The column labels show metabolic enzymes affected by differentially expressed substrate or product. A black dot is provided at row *i* column *j* if a metabolite of row *i* is a substrate or a product of a metabolic enzyme of column *j*. The number of regulations by the indicated substrate or product (Right). Only the regulations whose number is 30 or more are shown in bar plot.

(D) Allosteric regulations in skeletal muscle to metabolic enzymes by allosteric regulators.

(E) Regulations by substrate or product in skeletal muscle to metabolic enzymes by differentially expressed substrate or product.

Differentially expressed molecules in the trans-omic network

- **Insulin Signal**
  Insulin signaling molecules of differentially phosphorylated proteins (DPPs)
- **Transcription factor (TF)**
  Differentially regulated TFs (DRTFs): Differentially expressed TFs (DETFs) and differentially phosphorylated TFs (DPTFs)
- **Enzyme mRNA**
  DEGs encoding metabolic enzymes
- **Enzyme Protein**
  Differentially expressed metabolic enzymes (DEMEs): Differentially expressed proteins (DEPs) encoding metabolic enzymes
- **Metabolic Reaction**
  Differentially regulated metabolic reactions: Metabolic reactions regulated by DEMEs, differentially expressed metabolites (DEMs), or both
- **Metabolite**
  DEMs

Color : Differentially expressed molecules (Intra-layer nodes)

Red : Increased molecules in *ob/ob*
Blue : Decreased molecules in *ob/ob*

Trans-omic network for differentially regulated metabolic reactions

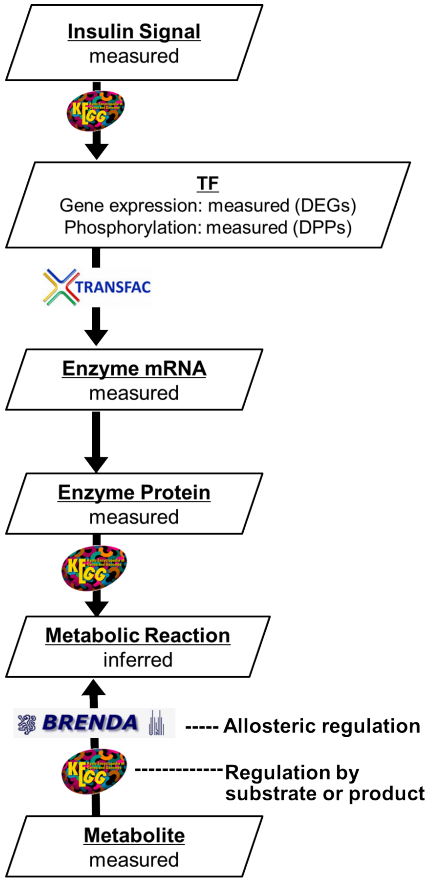

Differential regulations in the trans-omic network

Regulations between differentially expressed molecules in adjacent layers

Using database for identification of differential regulations

From Insulin Signal to TF(phosphorylation)
✓ KEGG

From TF to Enzyme mRNA
✓ TRANSFAC

From Enzyme Protein to Metabolic Reaction
✓ KEGG

From Metabolite to Metabolic Reaction
✓ BRENDA (for Allosteric regulation)
✓ KEGG (for Regulation by substrate or product)

Color : Differential regulations (Inter-layer edges)

Red : Activating regulations in *ob/ob*
Blue : Inhibiting regulations in *ob/ob*

Differential regulations in trans-omic network

			Regulated differentially expressed molecules in trans-omic network						
			TF(Phosphorylation)		Enzyme mRNA		Enzyme Protein		Metabolic Reaction
			Increased	Decreased	Increased	Decreased	Increased	Decreased	
Regulating differentially expressed molecules in trans-omic network	Insulin Signal (Activator)	Increased	Activating	-					
		Decreased	-	Inhibiting					
	Insulin Signal (Inhibitor)	Increased	-	Inhibiting					
		Decreased	Activating	-					
	TF	Activated			Activating	-			
		Inhibited			-	Inhibiting			
	Enzyme mRNA	Increased					Activating	-	
		Decreased					-	Inhibiting	
	Enzyme Protein	Increased							Activating
		Decreased							Inhibiting
	Metabolite (Allosteric activator)	Increased							Activating
		Decreased							Inhibiting
	Metabolite (Allosteric inhibitor)	Increased							Inhibiting
		Decreased							Activating
	Metabolite (Substrate)	Increased							Activating
		Decreased							Inhibiting
	Metabolite (Product)	Increased							Inhibiting
		Decreased							Activating

Figure S5. Contents of the Trans-Omic Network for Differentially Regulated Metabolic Reactions between WT and *ob*/*ob* Mice. Related to Figure 4.

The layers of the Insulin Signal, Transcription Factor (TF), Enzyme mRNA, Enzyme Protein, and Metabolite correspond to the indicated differentially expressed molecules. The Metabolic Reaction layer represents differentially regulated metabolic reactions, which are defined as metabolic reactions directly regulated by the differentially expressed molecules in the Enzyme Protein layer and those in the Metabolite layer. The upward and downward arrows indicate the differential regulations between differentially expressed molecules in each omic layer. The databases used to identify the differential regulations are shown on the arrows. The left panel of the diagram showed the definitions of the differentially expressed molecules included in each layer (upper) and the color annotations according to the classification of the differentially expressed molecules (lower). The right panel of the diagram shows the definition of differential regulations (upper), the database used to identify differential regulations (middle), and the color annotations according to the classification of differential regulations (lower), respectively. The lower table represents the classification of the differential regulations in trans-omic network. The differential regulations are classified into either activating or inhibiting regulations in *ob*/*ob* mice, which are determined by the combination of the direction of changes of differentially expressed molecules (increased or decreased) and of direction of regulation (activator or inhibitor).

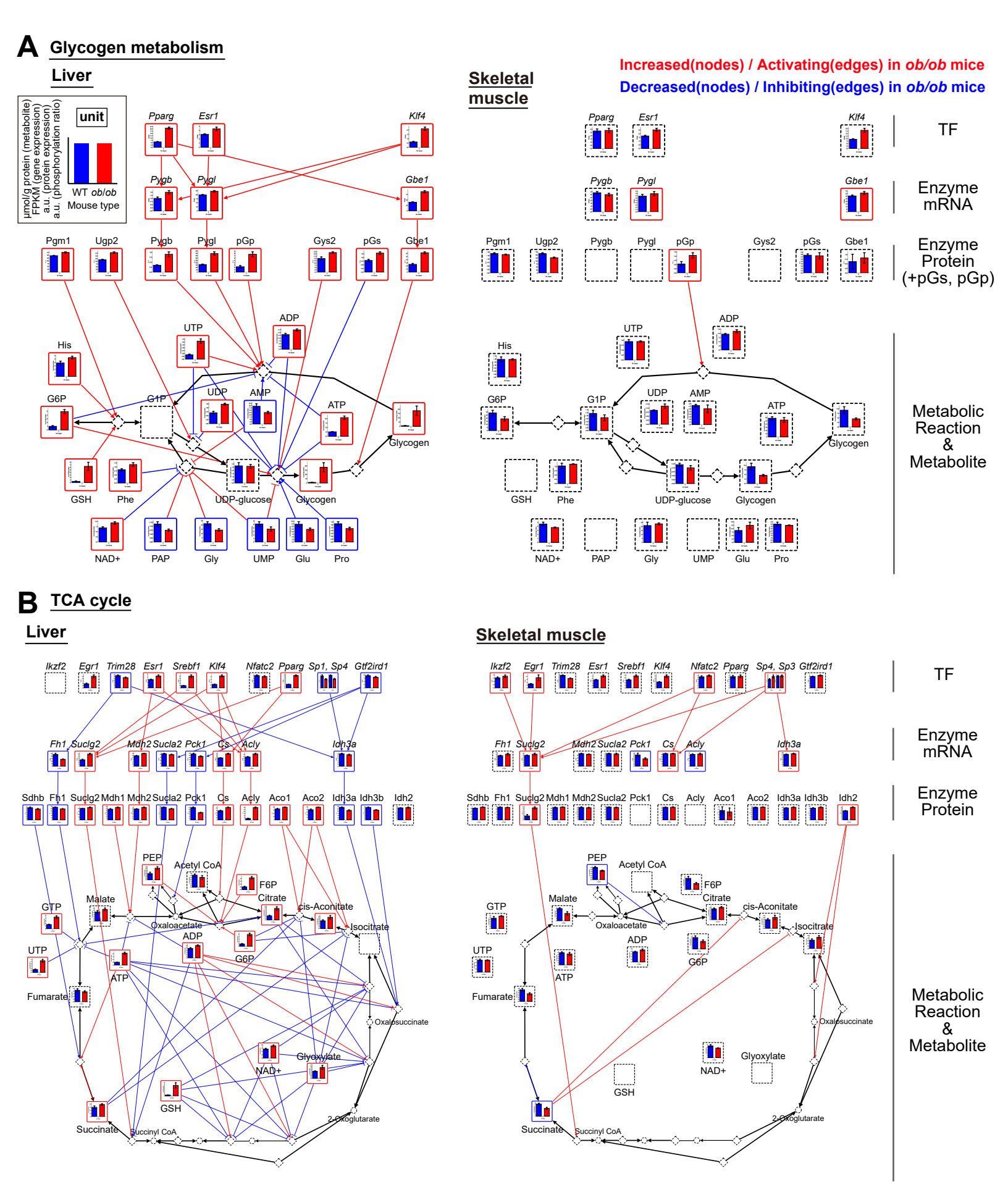
A
Glycogen metabolism
Liver
Skeletal muscle
Increased(nodes) / Activating(edges) in ob/ob mice
Decreased(nodes) / Inhibiting(edges) in ob/ob mice
μmol/g protein (metabolite)
FPKM (gene expression)
a.u. (protein expression)
a.u. (phosphorylation ratio)
unit
WT ob/ob
Mouse type
Pparg
Esr1
Klf4
Pygb
Pygl
Gbe1
Pgm1
Ugp2
pGp
Gys2
pGs
His
G6P
G1P
UTP
ADP
UDP
AMP
ATP
Glycogen
GSH
Phe
UDP-glucose
NAD+
PAP
Gly
UMP
Glu
Pro
TF
Enzyme mRNA
Enzyme Protein (+pGs, pGp)
Metabolic Reaction & Metabolite
B
TCA cycle
Liver
Skeletal muscle
Ikzf2
Egr1
Trim28
Srebf1
Nfatc2
Sp1, Sp4
Sp4, Sp3
Gtf2ird1
Fh1
Suclg2
Mdh2
Sucla2
Pck1
Cs
Acly
Idh3a
Sdhb
Mdh1
Aco1
Aco2
Idh3b
Idh2
PEP
Acetyl CoA
F6P
Citrate
cis-Aconitate
Isocitrate
Malate
GTP
Oxaloacetate
ADP
G6P
UTP
ATP
Fumarate
Oxalosuccinate
Glyoxylate
NAD+
GSH
Succinate
Succinyl CoA
2-Oxoglutarate
TF
Enzyme mRNA
Enzyme Protein
Metabolic Reaction & Metabolite

Figure S6. The Trans-Omic Network for Differentially Regulated Metabolic Reactions in Glycogen Metabolism and TCA cycle. Related to Figure 4.

(A, B) The trans-omic network for differentially regulated metabolic reactions in glycogen metabolism (A) and TCA cycle (B) in the liver and skeletal muscle. The information for glycogen metabolism and TCA cycle were obtained from “starch and sucrose metabolism” (mmu00500) or “TCA cycle” (mmu00020) in the KEGG database, respectively (Kanehisa et al., 2017). In Enzyme Protein layer of the trans-omic network for differentially regulated metabolic reactions in glycogen metabolism, we also added the information of phosphorylation of glycogen synthetase (pGs) and glycogen phosphorylase (pGp) (see also Figure 2A), which are key enzymes in the insulin signaling molecules that involved in the glycogen metabolism. Bar plots of measured molecules in WT and *ob*/*ob* mice are shown for corresponding nodes as the means and SEMs of mice replicate (number indicated in Transparent Methods). The colors of the frames indicate differentially expressed molecules increased in *ob*/*ob* mice (red) and those decreased in ob/ob mice (blue). The dashed frames indicate molecules that were not included in the trans-omic network of each organ. Diamond nodes indicate metabolic reactions. The colored edges indicate differential regulations: activating regulation in *ob*/*ob* mice (red) and inhibiting regulation in *ob*/*ob* mice (blue). From Metabolite to Metabolic Reaction, only allosteric regulations are colored. Black edges indicate the relationship between metabolic reactions and its substrate/product. The reversibility of metabolic reactions was obtained from the KEGG database (Kanehisa et al., 2017).

Glycogen is a glucose polymer stored in the liver and skeletal muscle, and the regulatory mechanism of glycogen metabolism is essential for blood glucose homeostasis. In the liver, glycogen and G6P significantly increased in *ob*/*ob* mice (Figure S6A left). The expression of enzyme proteins, such as Pgm1, Ugp2, Gys2, and Gbe1, which are responsible for a series of synthetic pathways from G6P to glycogen, increased in the liver of *ob*/*ob* mice. Pygb and Pygl, which catalyze the degradation of glycogen to G1P, also increased. Among the increased DEMEs in the liver of *ob*/*ob* mice, Pygb, Pygl, and Gbe1 showed the increased expression at the transcript level, and their gene expression was regulated by *Pparg*, *Esr1*, or *Klf4*. These results suggest that the turnover of glycogen synthesis and degradation increased in liver of *ob*/*ob* mice. A number of allosteric regulations by DEMs were also identified in the liver (8 activating and 14 inhibiting regulations in *ob*/*ob* mice). In contrast to glycogen metabolism in the liver, G6P [fold change (FC) (*ob*/*ob*/WT) = 0.66, q value = 0.13)] and glycogen [FC (*ob*/*ob*/WT) = 0.48, q value = 0.13] slightly decreased in skeletal muscle (Figure S6A right). Also, unlike the liver, there was no regulation in skeletal muscle from Enzyme Protein or Metabolite to the Metabolic Reaction, except for the activating regulation by phosphorylation of glycogen phosphorylase.

In the TCA cycle in the liver, citrate, cis-aconitate, and succinate increased in *ob*/*ob* mice (Figure S6B left). Malate [FC (*ob*/*ob*/WT) = 1.29, q value = 0.12] showed a slightly increased in the liver of *ob*/*ob* mice. In the regulations from Enzyme Protein to Metabolic Reaction in the liver, we identified the 9 activating and 6 inhibiting regulations in *ob*/*ob* mice. Cs, Acly, Aco1, and Aco2, which are responsible for metabolic reactions in the former half of the TCA cycle in the liver, increased in *ob*/*ob* mice, and indeed citrate and cis-Aconitate also increased in *ob*/*ob* mice. In addition, we identified many allosteric regulations by the increased DEMs in *ob*/*ob* mice (11 activating and 28 inhibiting regulations in ob/ob mice). Although no significant changes of amount of citrate and cis-Aconitate were detected between WT and *ob*/*ob* mice in skeletal muscle, citrate [FC (*ob*/*ob*/WT) = 1.16, q value = 0.18] and cis-Aconitate [FC (*ob*/*ob*/WT) = 1.27, q value = 0.24] shown slightly increases (Figure S6B right). We also identified Idh2, which is the increased DEME specifically in skeletal muscle. Furthermore, succinate and malate in the latter half of the TCA cycle showed a slightly increase in the liver of *ob*/*ob* mice, while those showed a slightly decrease in skeletal muscle of *ob*/*ob* mice (Figure S6B). Suclg2, a metabolic enzyme responsible for the conversion of succinyl-CoA to succinate, was the increased DEMEs common in both liver and skeletal muscle. The expression of *Suclg2* was upregulated at the transcript level both in the liver and skeletal muscle. *Suclg2* expression in the liver was regulated by *Pparg*, *Klf4*, and *Srebf1*, while that in skeletal muscle was regulated by *Ikzf1*, *Egr1*, and *Nfatc2*. In addition, succinate was identified as the increased DEM contributing to inhibiting regulations in the liver, while in skeletal muscle of *ob*/*ob* mice, it was identified as the decreased DEM contributing to activating regulations.

Fatty acid synthesis

Liver

Increased(nodes) / Activating(edges) in *ob/ob* mice

Decreased(nodes) / Inhibiting(edges) in *ob/ob* mice

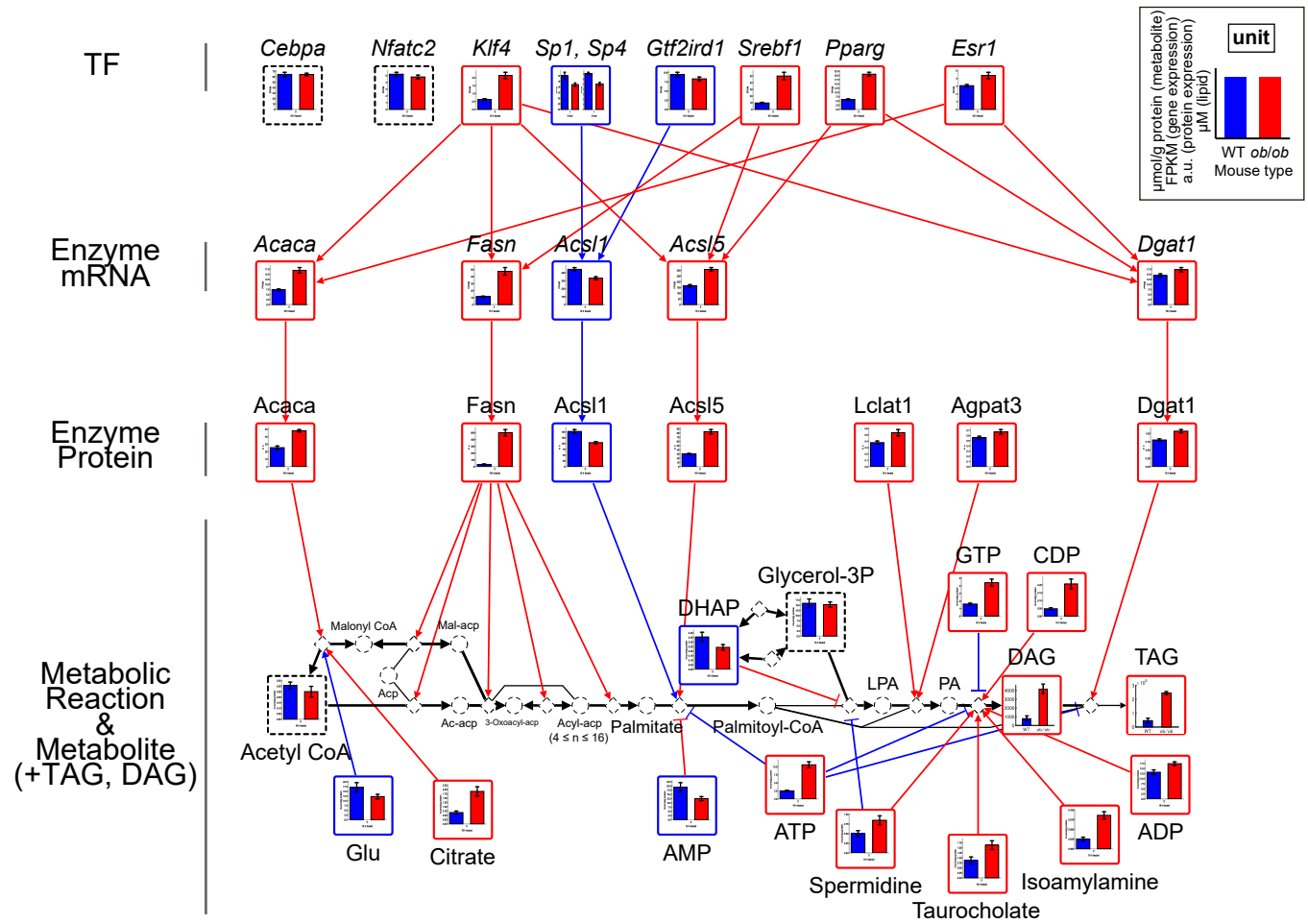

Skeletal muscle

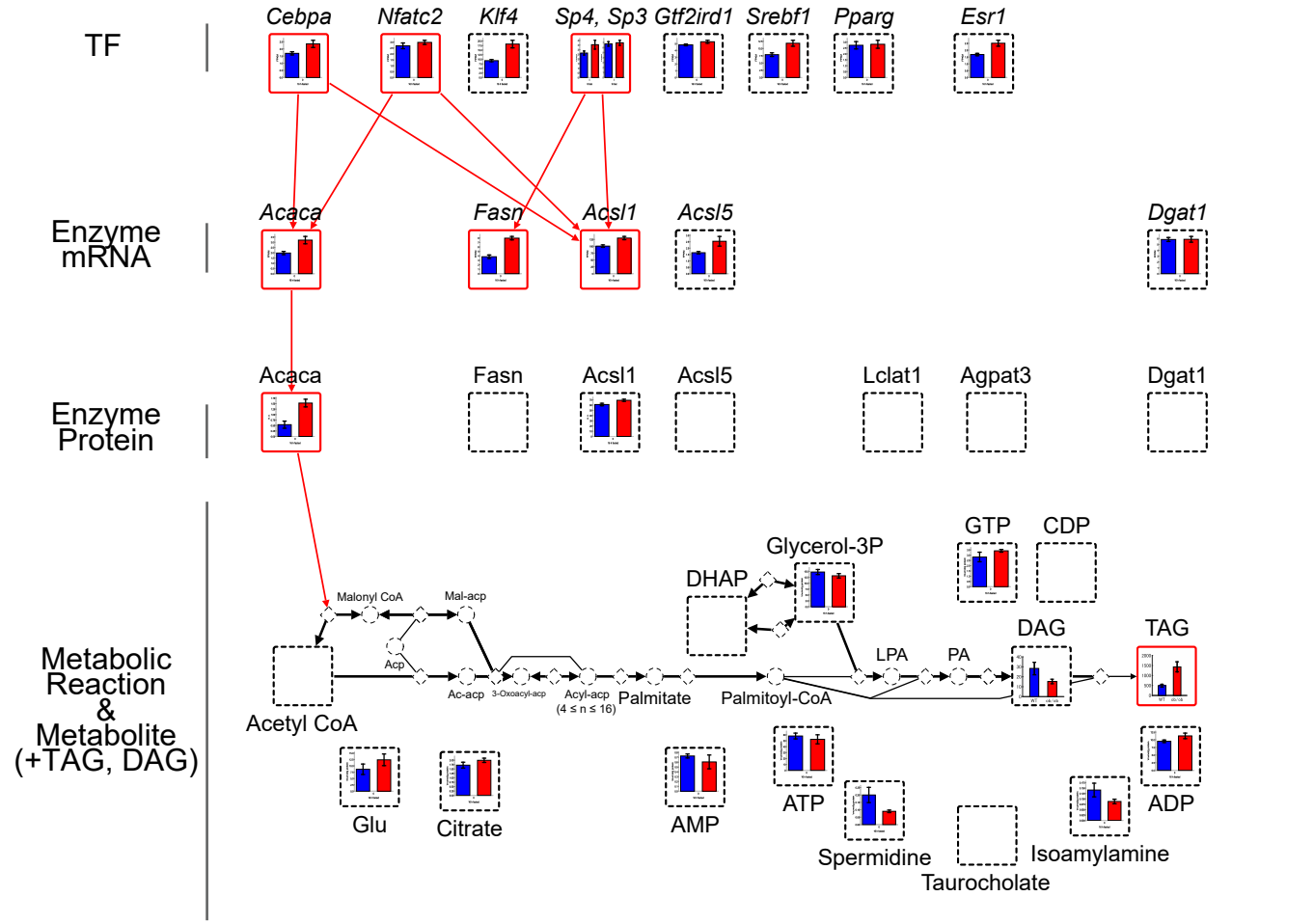

Figure S7. The Trans-Omic Network for Differentially Regulated Metabolic Reactions in Fatty Acid Synthesis. Related to Figure 4.

The trans-omic network for differentially regulated metabolic reactions in fatty acid synthesis in the liver and skeletal muscle. The information for fatty acid synthesis were obtained from “fatty acid biosynthesis” (mmu00061), “glycerolipid metabolism” (mmu00561) and “glycerophospholipid metabolism” (mmu00564) in the KEGG database (Kanehisa et al., 2017). Data are shown as the mean and SEM of mice replicate (number indicated in Transparent Methods).

We investigated the fatty acid synthesis pathway (Figure S7) and fatty acid degradation pathway (see Figures 7A and 7B) in the liver and skeletal muscle, because fatty acid metabolism is a key factor in controlling lipid metabolic homeostasis. We identified a significant increase in Triacylglycerol (TAG) both in the liver and skeletal muscle of *ob*/*ob* mice in fatty acid synthesis pathways (Figure S7). Diacylglycerol (DAG), a precursor of TAG, also increased in the liver of *ob*/*ob* mice (Figure S7 upper). In the liver, we identified six increased DEMEs. The gene expression of *Acaca*, *Fasn*, *Acsl5*, and *Dgat1* was regulated by the increased DRTFs such as *Srebf1*, *Pparg*, *Esr1*, and *Klf4*. In addition, we identified several allosteric regulations by the DEMs in *ob*/*ob* mice (8 activating and 5 inhibiting regulations). Taken together, these results suggest that activation of fatty acid synthesis in the liver of *ob*/*ob* mice. In skeletal muscle of *ob*/*ob* mice, there was only activating regulations by the increased DEME Acaca (Figure S7 lower). Also, we were not able to detect any allosteric regulations by DEMs in skeletal muscle of *ob*/*ob* mice. Given that Acaca and TAG increased in skeletal muscle of *ob*/*ob* mice, this result implies that the fatty acid synthesis in skeletal muscle was also activated in skeletal muscle as well as in the liver. Note, however, that many of activating regulations in *ob*/*ob* mice found in the liver was not detected in skeletal muscle (Figure S7). In summary, fatty acid synthesis (Figure S7) and fatty acid degradation (Figures 7A and 7B) are commonly activated both in the liver and skeletal muscle of *ob*/*ob* mice. This result implies that fatty acid turnover may increase in both organs in obese individuals fasted for 16 hours.

Arginine synthesis

Liver

Increased(nodes) / Activating(edges) in *ob/ob* mice

Decreased(nodes) / Inhibiting(edges) in *ob/ob* mice

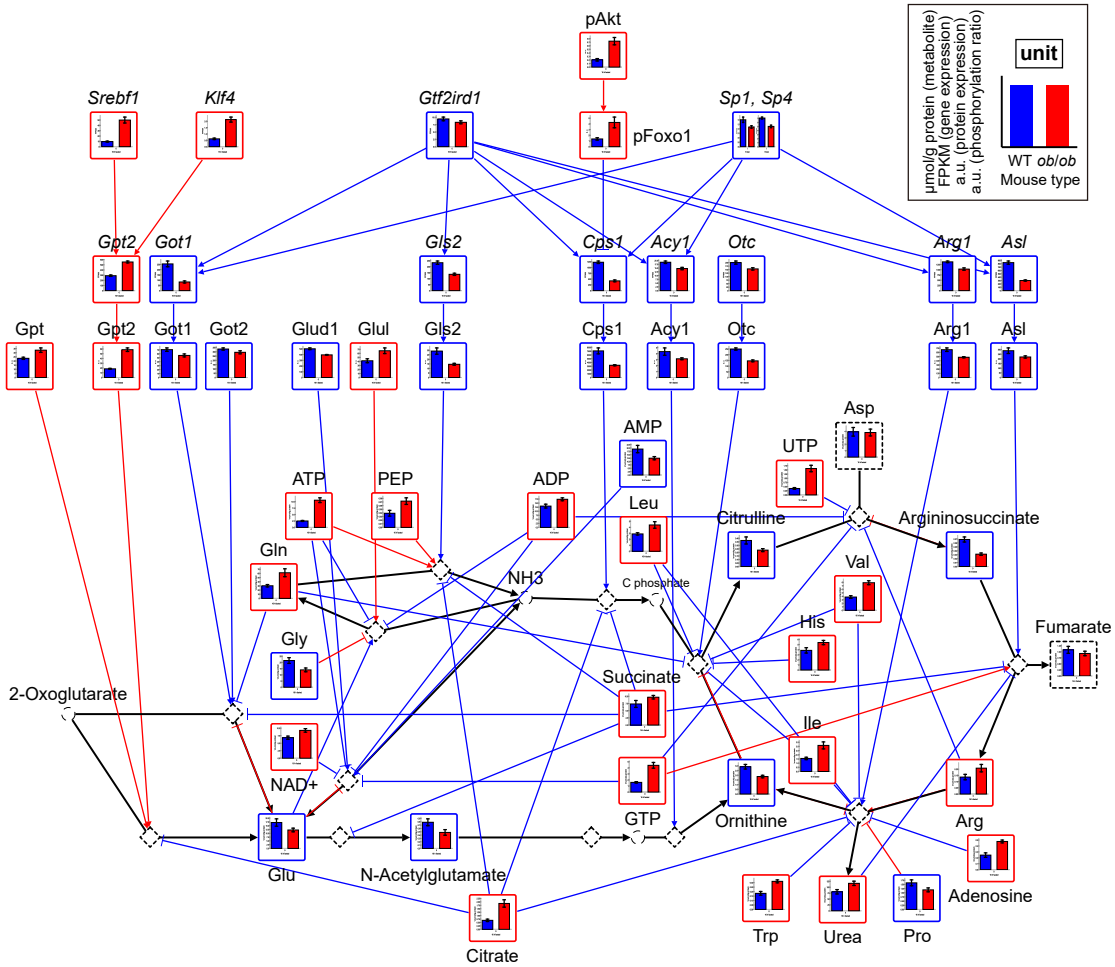

Skeletal muscle

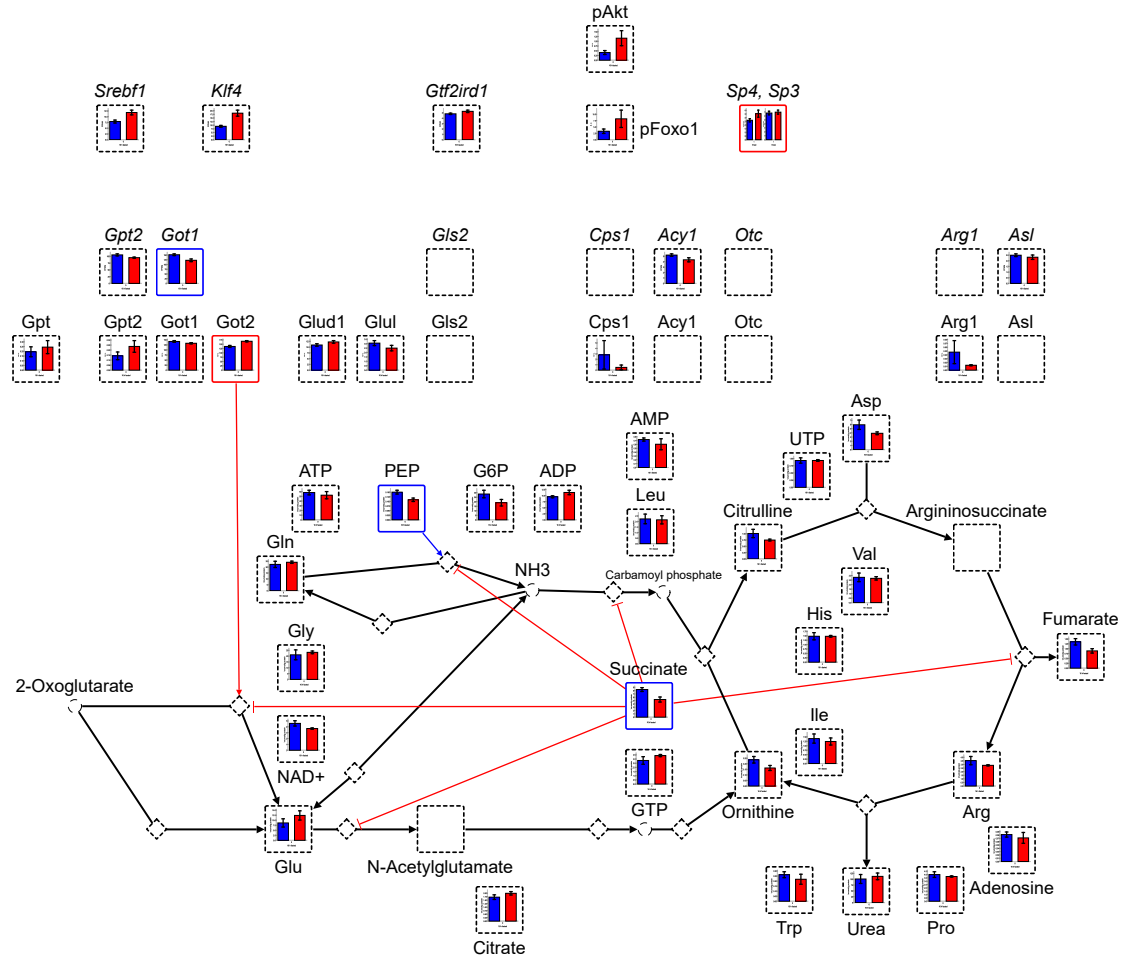

Figure S8. The Trans-Omic Network for Differentially Regulated Metabolic Reactions in Arginine Synthesis. Related to Figure 4.

The trans-omic network for differentially regulated metabolic reactions in arginine synthesis in the liver and skeletal muscle. The information for arginine synthesis were obtained from “arginine biosynthesis” (mmu00220) in the KEGG database (Kanehisa et al., 2017). Data are shown as the mean and SEM of mice replicate (number indicated in Transparent Methods).

Arginine is synthesized mainly through the urea cycle. We investigated the arginine synthesis pathway in the liver, because the expression of genes encoding the urea cycle-related enzymes Cps1 and Otc decrease in obese patients with NASH and in obese mice fed a high fat and cholesterol diet (Chiara et al., 2018; Rodríguez-Suárez et al., 2010). We investigated arginine synthesis pathway also in skeletal muscle. We identified several decreased DEMs in the liver of *ob*/*ob* mice such as Glu, N-acetylglutamate, argininosuccinate, citrulline, and ornithine (Figure S8 upper). Gln, Arg, and Urea were the increased DEMs in the liver of *ob*/*ob* mice. In the liver, except for Gpt, Gpt2, and Glul, 9 DEMEs significantly decreased. Of the 9 decreased DEMEs in *ob*/*ob* mice, seven of them, including Cps1, Gls2, Otc, Arg1, and Asl, were regulated through changes in gene expression, and gene expression of them are regulated by some DRTFs such as *Gtf2ird1*, *Sp1*, *Sp4*, and phosphorylated Foxo1. Inhibition of transcriptional activity of Foxo1 by phosphorylation increased in ob/ob mice was conducted by increased Akt activation by phosphorylation. In addition, we identified many allosteric regulations by the DEMs (8 activating and 26 inhibiting regulations). These results suggest that the arginine synthesis in the liver is inhibited in *ob*/*ob* mice through the regulations by Enzyme Protein, which is consistent with previous reports, and by Metabolite. We identified the only DEME in skeletal muscle of *ob*/*ob* mice was identified as Got2, which was increased in *ob*/*ob* mice (Figure S8 lower). We examined the differential regulations by the DEMs in skeletal muscle, and identified those by PEP and succinate. Although many metabolites were measured in skeletal muscle, they did not show any changes in *ob*/*ob* mice compared to WT mice. All differentially expressed molecules in skeletal muscle in this pathway (Got2, succinate, and PEP) showed the opposite changes to the liver (Figure S8).

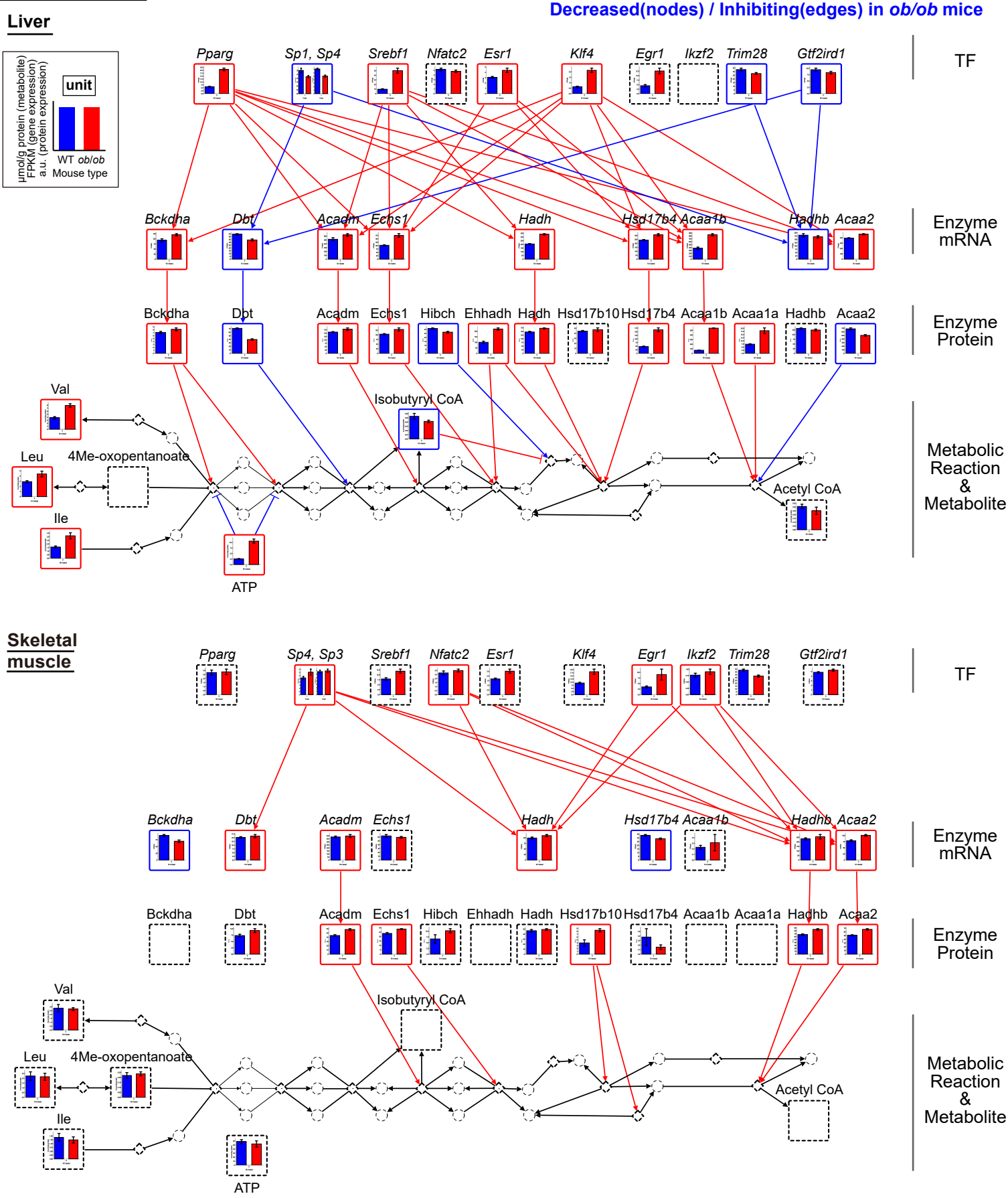
BCAA degradation
Liver
Increased(nodes) / Activating(edges) in ob/ob mice
Decreased(nodes) / Inhibiting(edges) in ob/ob mice
μmol/g protein (metabolite)
FPKM (gene expression)
a.u. (protein expression)
unit
WT ob/ob
Mouse type
Pparg
Sp1, Sp4
Srebf1
Nfatc2
Esr1
Klf4
Egr1
Ikzf2
Trim28
Gtf2ird1
TF
Bckdha
Dbt
Acadm
Echs1
Hadh
Hsd17b4
Acaa1b
Hadhb
Acaa2
Enzyme mRNA
Bckdha
Dbt
Acadm
Echs1
Hibch
Ehhadh
Hadh
Hsd17b10
Hsd17b4
Acaa1b
Acaa1a
Hadhb
Acaa2
Enzyme Protein
Val
Isobutyryl CoA
Leu
4Me-oxopentanoate
Ile
Acetyl CoA
ATP
Metabolic Reaction & Metabolite
Skeletal muscle
Pparg
Sp4, Sp3
Srebf1
Nfatc2
Esr1
Klf4
Egr1
Ikzf2
Trim28
Gtf2ird1
TF
Bckdha
Dbt
Acadm
Echs1
Hadh
Hsd17b4
Acaa1b
Hadhb
Acaa2
Enzyme mRNA
Bckdha
Dbt
Acadm
Echs1
Hibch
Ehhadh
Hadh
Hsd17b10
Hsd17b4
Acaa1b
Acaa1a
Hadhb
Acaa2
Enzyme Protein
Val
Isobutyryl CoA
Leu
4Me-oxopentanoate
Ile
Acetyl CoA
ATP
Metabolic Reaction & Metabolite

Figure S9. The Trans-Omic Network for Differentially Regulated Metabolic Reactions in BCAA Degradation. Related to Figure 4.

The trans-omic network for differentially regulated metabolic reactions in BCAA degradation in the liver and skeletal muscle. The information for BCAA degradation were obtained from “valine, leucine and isoleucine degradation” (mmu00280) in the KEGG database (Kanehisa et al., 2017). Data are shown as the mean and SEM of mice replicate (number indicated in Transparent Methods).

BCAAs, three branched-chain amino acids among the essential amino acids, in organs and in the blood are known to be involved in insulin resistance associated with obesity and type 2 diabetes in several context (Newgard et al., 2009; White and Newgard, 2019). BCAAs are catabolized for energy source in several organs including of the liver, skeletal muscle, and adipose tissues. In the BCAA degradation pathway in the liver of *ob*/*ob* mice, we found increases of all BCAAs Val, Leu, and Ile (Figure S9 upper). Of the eight DEMEs whose expression increased in the liver of *ob*/*ob* mice, the expression of six proteins, including Bckdha, Acadm, Echs1, and Acaa1b, changed also at the transcript level, and those expression were upregulated by the increased DRTFs such as *Srebf1*, *Pparg*, *Esr1*, and *Klf4*. In addition, the increases of Acadm and Hadhb and Acaa2, among the five increased DEMEs, were seen also at the transcript level in skeletal muscle of *ob*/*ob* mice (Figure S9 lower). The expression of these genes was upregulated by *Sp4*, *Sp3*, *Nfatc2*, *Egr1*, and *Ikzf2*. Moreover, we found that Acadm and Ecsh1 increased common in the liver and skeletal muscle of *ob*/*ob* mice (Figure S9). These results suggest that in BCAA degradation pathway, the activations by DEMEs occurs both in the liver and skeletal muscle of *ob*/*ob* mice.

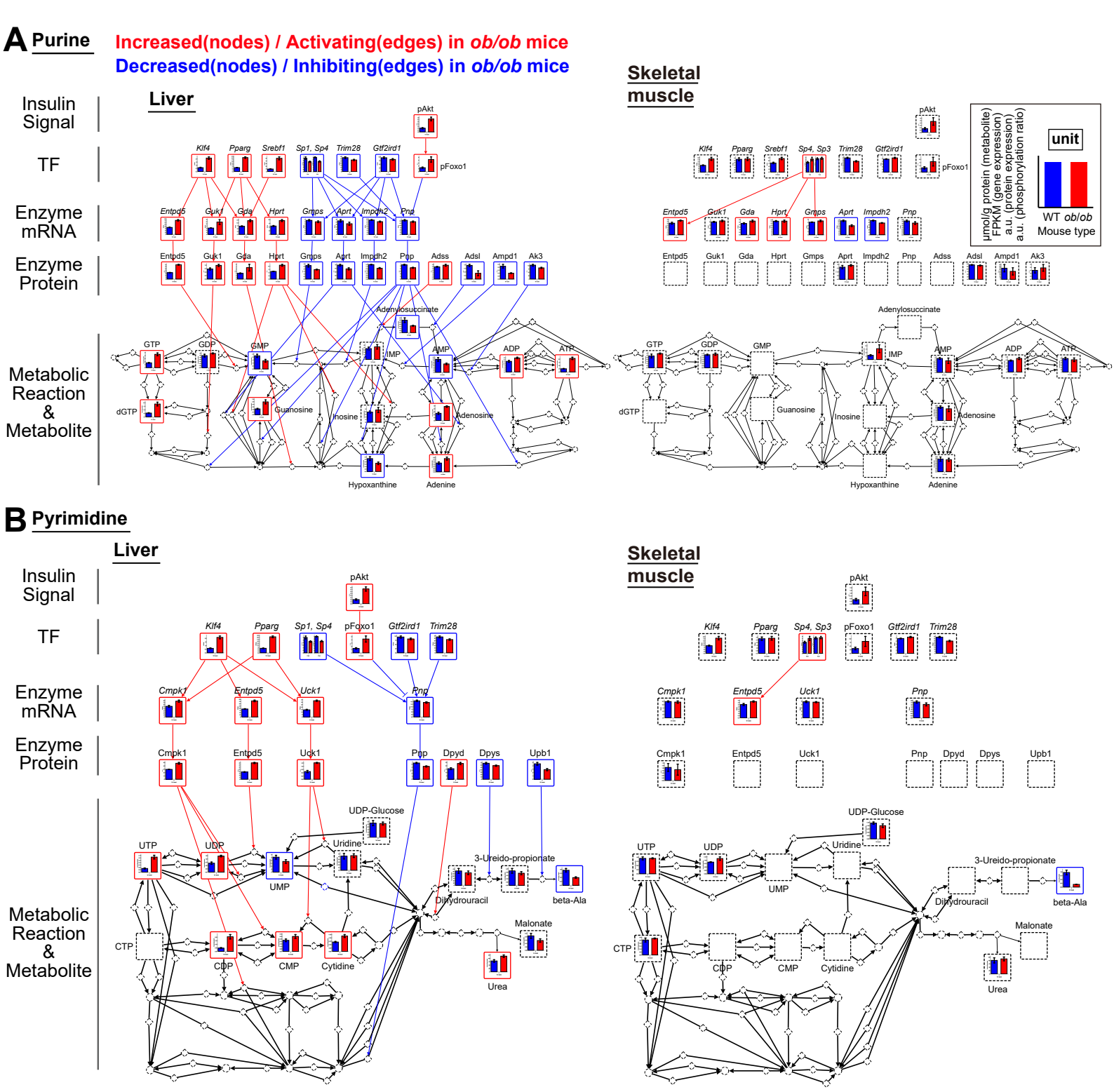
A Purine
Increased(nodes) / Activating(edges) in ob/ob mice
Decreased(nodes) / Inhibiting(edges) in ob/ob mice
Insulin Signal
TF
Enzyme mRNA
Enzyme Protein
Metabolic Reaction & Metabolite
Liver
Skeletal muscle
pAkt
pFoxo1
Klf4
Pparg
Srebf1
Sp1, Sp4
Sp4, Sp3
Trim28
Gtf2ird1
Entpd5
Guk1
Gda
Hprt
Gmps
Aprt
Impdh2
Pnp
Adss
Adsl
Ampd1
Ak3
Adenylosuccinate
GTP
GDP
GMP
IMP
AMP
ADP
ATP
dGTP
Guanosine
Inosine
Adenosine
Hypoxanthine
Adenine
μmol/g protein (metabolite)
FPKM (gene expression)
a.u. (protein expression)
a.u. (phosphorylation ratio)
unit
WT ob/ob
Mouse type
B Pyrimidine
Liver
Skeletal muscle
Cmpk1
Uck1
Dpyd
Dpys
Upb1
UTP
UDP
UMP
UDP-Glucose
Uridine
CTP
CDP
CMP
Cytidine
Dihydrouracil
3-Ureido-propionate
beta-Ala
Malonate
Urea

Figure S10. The Trans-Omic Network for Differentially Regulated Metabolic Reactions in Purine and Pyrimidine Metabolism. Related to Figure 4.

(A, B) The trans-omic network for differentially regulated metabolic reactions in purine metabolism (A) and pyrimidine metabolism (B) in the liver and skeletal muscle. The information for purine metabolism or pyrimidine metabolism were obtained from “purine metabolism” (mmu00230) or “pyrimidine metabolism” (mmu00240) in the KEGG database, respectively (Kanehisa et al., 2017). Data are shown as the mean and SEM of mice replicate (number indicated in Transparent Methods).

In purine metabolism, the increases in GTP and ATP and the decreases in GMP and AMP were seen in the liver of *ob*/*ob* mice (Figure S10A left). We found that the expression of Entpd5, Guk1, Gda, and Hqrt increased in the liver of *ob*/*ob* mice, and gene expression of them was regulated by *Srebf1* and *Pparg*. In addition, among the 12 DEMEs, seven of those decreased in the liver of *ob*/*ob* mice. The decreased DEMEs in *ob*/*ob* mice contained Pnp, which contributes to the metabolic reaction of diverse nucleotide intermediates and whose expression at the transcript level was regulated by the DRTFs such as *Sp1*, *Sp4*, *Trim28*, *Gtf2ird1*, and phosphorylated Foxo1. In skeletal muscle, many nucleotides did not change between WT and *ob*/*ob* mice, except for a slightly increase in IMP [(fold change (*ob*/*ob*/WT) = 2.59, q value = 0.17)] (Figure S10A right).

In the pyrimidine metabolism, the increases in UTP, UDP, CDP, and CMP and the decreases in UMPs were found in the liver of *ob*/*ob* mice (Figure S10B left). The expression of metabolic enzymes surrounding the derivatives of Uridine and Cytidine, such as Cmpk1, Entpd5, and Uck1, were shown to increase in the liver of *ob*/*ob* mice. In addition, the expression of Dpys and Upb1, which are responsible for the series of metabolic reactions from dihydrouracil to beta-alanine in the liver, decreased in the liver of *ob*/*ob* mice. In skeletal muscle, there was no differential regulation by the expression changes of metabolic enzymes, and except for Cmpk1, no molecules were detected at the protein level (Figure S10B right). The beta-alanine was identified as the only DEM that decreased in common with both organs of *ob*/*ob* mice (Figure S10B).

To summarize the changes in metabolite amount in *ob*/*ob* mice, we found that dynamic changes of nucleic acid molecule were seen in the liver, whereas in skeletal muscle, those showed little changes. Triphosphate with three phosphate groups attached to ribose, such as GTP and ATP as derivatives of purines and UTP as derivatives of pyrimidines, significantly increased in the liver of *ob*/*ob* mice. In contrast, monophosphates such as GMP, AMP, and UMP significantly decreased in the liver of *ob*/*ob* mice.

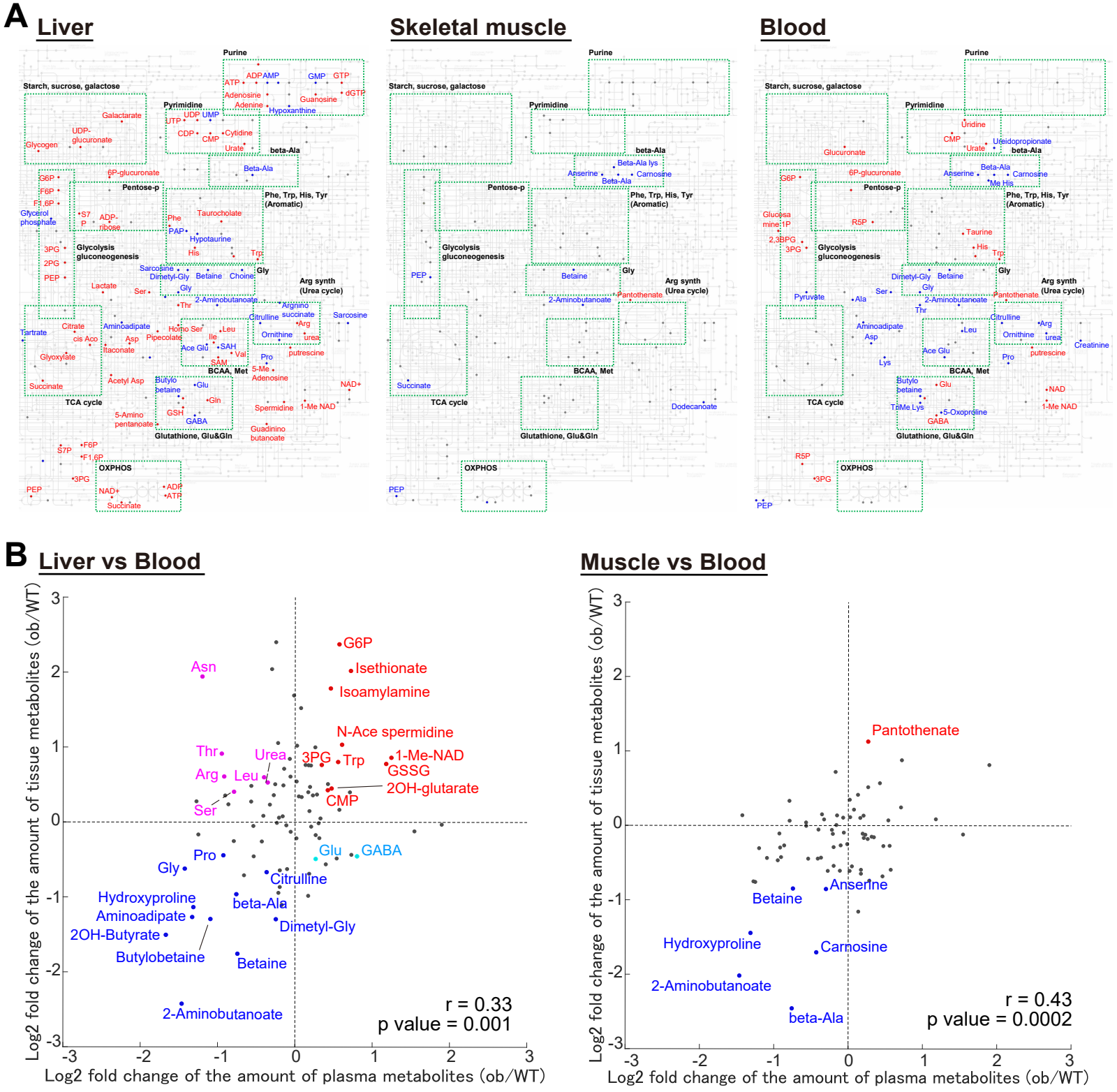

Figure S11. Differentially Expressed Metabolites in Liver, Skeletal Muscle, and Blood. Related to Figure 5.

(A) Information of metabolites of the liver, skeletal muscle, and blood projected on a global map of metabolic pathway (mmu01100) from the KEGG databases. Each dot on a global map was colored according to the variation of each metabolite: red dots, the increased DEMs in *ob*/*ob* mice; blue dots, the decreased DEMs in *ob*/*ob* mice; gray dots, those were measured in both WT and *ob*/*ob* mice but were not the DEMs.

(B) The $\log_2$ fold changes of metabolites measured in blood and each organ between WT and *ob*/*ob* mice. Each dot on a scatter plot was colored according to the variation of each metabolite: red dots, increased metabolites in *ob*/*ob* mice both in the organ and the blood; blue dots, decreased metabolites in *ob*/*ob* mice both in the organ and the blood; magenta dots, metabolites with increased in the organ and decreased in the blood in *ob*/*ob* mice; cyan dots, metabolites with decreased in the organ and increased in the blood in *ob*/*ob* mice.

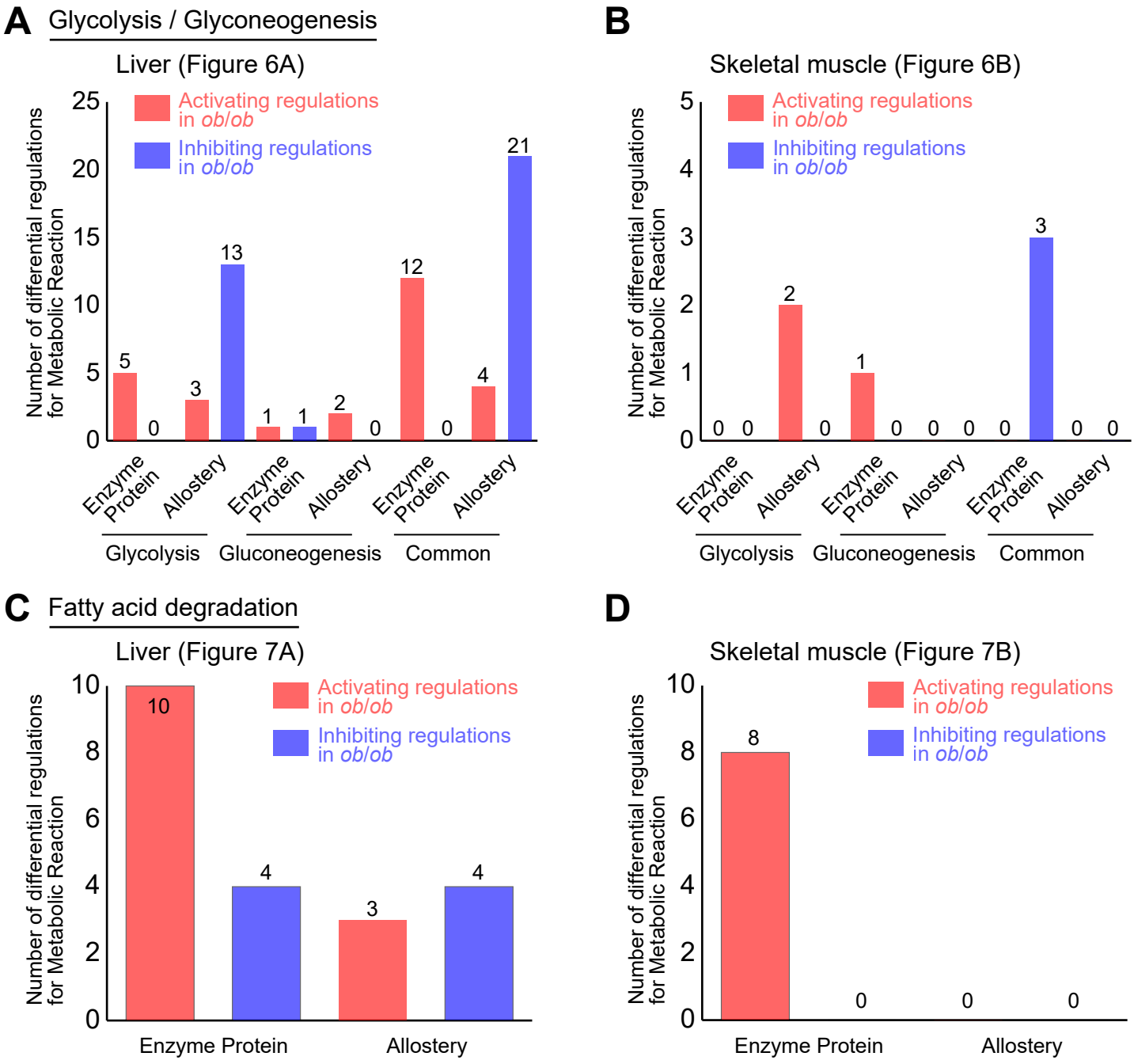

Figure S12. The Activating and Inhibiting Differential Regulations for Metabolic Reaction of Trans-Omic Subnetworks. Related to Figures 6 and 7.

The number of activating and inhibiting differential regulations of enzyme expression from Enzyme Protein layer and allosteric regulation from Metabolite layer in glycolysis/gluconeogenesis metabolic pathway in the liver (Figure 6A) (A) and skeletal muscle (Figure 6B) (B). The number of activating and inhibiting differential regulations of enzyme expression from Enzyme Protein layer and allosteric regulation from Metabolite layer in fatty acid degradation pathway in the liver (Figure 7A) (C) and skeletal muscle (Figure 7B) (D).

		Changes in our *ob*/*ob* mice	Changes in high-fat diet-fed mice (Soltis *et al*., 2017)
DETFs	*Srebf1*	Increase	Increase
	Pparg	Increase	Increase
	Klf4	Increase	Not change
	Esr1	Increase	Increase
	Zfx	Decrease	Decrease
	Gtf2ird1	Decrease	Decrease
	Trim28	Decrease	Decrease
	Onecut1	Decrease	Increase
	Sp4	Decrease	Not change
	Sp1	Decrease	Not change

Figure S13. Comparison of the Expression of DETFs in Liver of *ob*/*ob* Mice with those in Liver of High-Fat Diet-Fed Mice. Related to Figure 2 and Discussion.

The table represents the expression changes of genes encoding to DETFs of our *ob*/*ob* mice in liver and those of high-fat diet-fed mice by Soltis *et al* (Soltis et al., 2017).

TRANSPARENT METHODS

Mouse Studies

Mouse experiments were approved by the animal ethics committee of The University of Tokyo. Ten-weeks-old male C57BL/6J wild-type (WT) and *ob*/*ob* mice were purchased from Japan SLC Inc. Sixteen hours-fasted mice were sacrificed by cervical dislocation, and the liver (whole or left lateral lobe) and skeletal muscle (gastrocnemius muscle) were dissected and frozen in liquid nitrogen. The frozen liver and skeletal muscle were pulverized with dry ice to a fine powder with a blender and separated into tubes for omic analyses (transcriptomics, proteomics, metabolomics, and lipidomics), and Western blotting. The following number of mouse replicates for each analysis was used: n = 5 both in WT and *ob*/*ob* mice for the identification of phosphorylated molecules by Western blotting, n = 11 (WT mice) and n = 12 (*ob*/*ob* mice) for transcriptomics, n = 5 both in WT and *ob*/*ob* mice for proteomics, n = 5 both in WT and *ob*/*ob* mice for metabolomics, n = 3 both in WT and *ob*/*ob* mice for lipidomics (see also Figure 1). The blood of each WT and *ob*/*ob* mice (n = 5) was collected from tail vein to measure blood glucose levels and insulin levels (see Figure S1). For blood metabolome analysis (see Figure 5), the blood of each WT and *ob*/*ob* mice (n = 5) was collected from the retro-orbital sinus into tubes containing 0.5 mg of EDTA soon after cervical dislocation, and the plasma was isolated by centrifugation at 2,300 × *g* for 15 min at 4ºC. We used the same data of the liver except for Western blotting analysis and the blood as we reported in our previous study (Kokaji et al., 2020). The skeletal muscle data were obtained from the same animals as the liver data. For Western blotting analysis, other individuals of mice were used.

Western Blotting

Total proteins were extracted from the liver and skeletal muscle with methanol:chloroform:water (2.5:2.5:1) extraction. Ice-cold methanol was added to the liver and skeletal muscle at a concentration of 100 mg/mL of the weight of the liver and skeletal muscle, and the suspension (400 µL) was mixed with chloroform (400 µL) and water (160 µL), followed by centrifugation at 4,600 × *g* for 10 min at 4ºC. Removing the aqueous and

organic phases, 800 µL of ice-cold methanol was added to the interphase to precipitate proteins. The obtained pellet was suspended with 400 µL of lysis buffer [10 mM Tris-HCl (pH 6.8) in 1% SDS], followed by sonication. The protein lysate was centrifuged at 12,000 × *g* for 3 min at 4ºC to remove debris. The concentration of total protein of the obtained supernatant was determined by BCA assay. Antibodies were purchased from Cell Signaling Technology, as follows: pIrβ (Tyr1150/Tyr1151) (#3024), total Irs1 (#2382), total Erk1/2 (#9102), pErk1/2 (Thr202/Tyr204) (#9101), total cAMP responsive element binding protein (Creb) (#9197), pCreb (Ser133) (#9198), total eukaryotic translation initiation factor 4e (eif4e) (#9742), peif4e (Ser209) (#9741), total Akt (#9272), pAkt (Ser473) (#9271), total S6 (#2217), pS6 (Ser235/Ser236) (#2211), total Gsk3β (#9315), pGsk3β (Ser9) (#9336), total Gs (#3886), pGs (Ser641) (#3891), total Ampkα (#2532), pAmpkα (Thr172) (#2531), total p38 (#9221), pp38 (Thr180/Tyr182) (#9211), total Foxo1 (#9462), pFoxo1 (Ser256) (#9461), and pAs160 (Thr642) (#8881). Antibodies against total Irβ (sc-711) and total Gp (sc-46347) were from Santa Cruz Biotechnology, and pIrs1 (Tyr612) (09-432), total Irs2 (MABS15) and total As160 (ABS54) were from Millipore. pGp (Ser15) was made in-house as previously described (Noguchi et al., 2013). The protein (20 µg or 30 µg) was separated on SDS-PAGE and blotted with the antibody. Immunodetection was carried out using Immobilon Western Chemiluminescent HRP Substrate (Millipore) or SuperSignal West Pico PLUS Chemiluminescent Substrate (Thermo Fisher Scientific), and the signals of Western blot were detected using a luminoimage analyzer (Fusion System Solo 7S; M&S Instruments Inc.), and quantified with the Fiji software (ImageJ; National Institutes of Health) (Schindelin et al., 2012). Contrast and brightness adjustment and treatment were performed with Photoshop CS6 (Adobe).

RNA Sequencing

Total RNAs were extracted from the liver and skeletal muscle using RNeasy Mini Kit (QIAGEN) and QIAshredder (QIAGEN) and assessed for quantity using Nanodrop (Thermo Fisher Scientific) and for quality using the 2100 Bioanalyzer (Agilent Technologies). cDNA libraries were generated using SureSelect strand-specific RNA library preparation kit (Agilent Technologies). The obtained cDNAs were subjected to 100-bp

paired-end sequencing on an Illumina HiSeq2500 Platform (Illumina) (Matsumoto et al., 2014). Sequences were aligned to the mouse reference genome obtained from the Ensembl database (Flicek et al., 2014; Cunningham et al., 2015) (GRCm38/mm10, Ensembl release 97) using the STAR software package (v.2.5.3a) (Dobin et al., 2013). To assemble transcript models (Ensembl release 97) from aligned sequences and to estimate gene expression level, the RSEM tool (v.1.3.0) was used (Li and Dewey, 2011). Gene expression level was represented as fragments per kilobase of exon per million mapped fragments (FPKM).

Proteomic Analysis

The liver and skeletal muscle were lysed with 0.5 mL of a solution containing 50 mM Tris-HCl pH8.8, 2%SDS, and 7 M urea, and then subjected to ultrasonic treatment with a Bioruptor (Digaenode). The samples were diluted with an equal volume of water and centrifuged at 15,000 *g* for 15 min at 4°C to remove insoluble fraction. The protein concentration of the lysates was determined with the bicinchoninic acid assay (Thermo Fisher Scientific) and adjusted to 1 mg/mL. Cysteine residues were blocked by incubation of the samples with 2 mM tris(2-carboxyethyl)phosphine hydrochloride (Thermo Fisher Scientific) for 30 min at 37 °C followed by alkylation with 10 mM 2-iodoacetamide for 30 min at room temperature. The proteins (200 μg) were precipitated with acetone for 3 hours at −30 °C and the resulting pellet was dispersed in 50 mM Triethylammonium bicarbonate by ultrasonic treatment (three times for 30 s with intervals of 30 s) with a Bioruptor (Diagenode). The protein suspension was subjected to digestion with lysyl endopeptidase (Wako) for 16 hours at 37 °C. Resulting peptides were centrifuged at 15,000 *g* for 15 min at 4°C and subjected to C18-StageTip purification prior to MS analysis (Rappsilber et al., 2007).

All samples were analyzed with Q Exactive (Thermo Fisher Scientific) instrument equipped with a Dionex Ultimate 3000 high-performance liquid chromatography (HPLC) System (Dionex Corporation) via a nano-electrospray source with a column oven set at 42 °C (AMR Inc.). Peptides were injected to pre-column, L-column micro (Chemicals Evaluation and Research Institute) and separated by in-house made 20 cm column filled with 2 μm octadecyl silane particle (Chemicals Evaluation and Research Institute) with a linear gradient

of 5–35% B for 110 min, 35–90% B for 1 min, and 90% B for 10 min at a flow rate of 200 nL/min, where A is 0.1% formic acid and B is 0.1% formic acid and 100% acetonitrile. Data acquisition was performed in data-dependent acquisition mode. Scan ranges were set at *m/z* 375-1600 for MS spectra and *m/z* 200-2000 for MS/MS spectra, respectively. MS spectra were acquired at a resolution of 70,000 at *m/z* 400 after accumulation to a target value of 1×10^6 with the maximum ion injection times for 60 msec. Up to the top 10, most abundant ions with charge 2+ or 3+ from the survey scan were selected with an isolation window of 1.5 *m/z* and then fragmented with an automatically optimized collision energy. MS/MS spectra were acquired at a resolution of 17,500 at *m/z* 400 after accumulation to a target value of 5×10^4 with the maximum ion injection times for 120 msec.

Raw data obtained from MS analyses were processed using MaxQuant software (version 1.6.0.16). MaxQuant uses its own search engine, andromeda, to search directly against the mouse Ensembl database (GRCm38/mm10, Ensembl release 97). The search was conducted with the following parameter settings: LysC/P, which also cleaves at carboxyl side of lysine, also if a proline follows, was selected as the enzyme used, the allowed number of missed cleavages was set to two, and carbamidomethylation of cysteine were selected as fixed modifications. Oxidized methionine was searched as variable modifications. Other parameters depended on the default settings in MaxQuant, which are optimized by the developers and are appropriate for most experiments.

Metabolomic Analysis

Total metabolites and proteins were extracted from the liver and skeletal muscle with methanol:chloroform:water (2.5:2.5:1) extraction. Approximately 40 mg of the liver and skeletal muscle was suspended with 500 μL of ice-cold methanol containing internal standards [20 μM L-methionine sulfone (Wako), 2-Morpholinoethanesulfonic acid (Dojindo), and D-Camphor-10-sulfonic acid (Wako)] for normalization of peak intensities of mass spectrometry (MS) among runs, then with, 500 μL of chloroform, and finally with 200 μL of water. After centrifugation at 4,600 × *g* for 15 min at 4ºC, the aqueous layer was filtered through a 5 kDa cutoff

filter (Human Metabolome Technologies) to remove protein contamination. The filtrate (320 μL) was lyophilized and, before MS analysis, dissolved in 50 μL water containing reference compounds [200 μM each of trimesate (Wako) and 3-aminopyrrolidine (Sigma-Aldrich)]. Proteins were precipitated by the addition of 800 μL of ice-cold methanol to the interphase and organic layers and separated by centrifugation at 12,000 × *g* for 15 min at 4ºC. The resulting pellet was washed with 1 mL of ice-cold 80% (v/v) methanol and resuspended in 1 mL of sample buffer containing 1% SDS and 50 mM Tris-Cl pH8.8, followed by sonication. The concentration of total protein was determined by BCA assay and was used for normalization of metabolite concentration among samples. Metabolites in the blood were extracted with methanol:chloroform:water (2.5:2.5:1). The blood (40 μL) was extracted with the sequential addition of 400 μL of ice-cold methanol containing the internal standards, 400 μL of chloroform, and 120 μL of water. After centrifugation at 10,000 × *g* for 3 min at 4 ºC, the aqueous layer was filtered through a 5 kDa cutoff filter (Human Metabolome Technologies) to remove protein contamination. The filtrate (300 μL) was lyophilized and, before analysis by MS, dissolved in 50 μL water containing the reference compounds.

All CE-MS experiments were carried out using an Agilent 1600 Capillary Electrophoresis system (Agilent technologies), an Agilent 6230 TOF LC/MS system, an Agilent 1200 series isocratic pump, a G1603A Agilent CE-MS adapter kit, and a G1607A Agilent CE electrospray ionization (ESI)-MS sprayer kit. Briefly, to analyze cationic compounds, a fused silica capillary [50 μm internal Diameter (i.d.) × 100 cm] was used with 1 M formic acid as the electrolyte (Soga and Heiger, 2000). Methanol/water (50% v/v) containing 0.01 μM hexakis(2,2-difluoroethoxy)phosphazene was delivered as the sheath liquid at 10 μL/min. ESI-TOFMS was carried out in positive ion mode, and the capillary voltage was set to 4 kV. Automatic recalibration of each acquired spectrum was achieved using the masses of the reference standards ([^{13}C isotopic ion of a protonated methanol dimer ($2CH_3OH+H)]^+$, *m/z* 66.0631) and ([hexakis(2,2-difluoroethoxy)phosphazene +H]$^+$, *m/z* 622.0290). The metabolites were identified by comparing their m/z values and relative migration times to the metabolite standards. Quantification was performed by comparing peak areas to calibration curves generated using internal standardization techniques with methionine sulfone. The other conditions were identical to those

described previously (Soga et al., 2006). A commercially available COSMO(+) (chemically coated with cationic polymer) capillary (50 μm i.d. x 105 cm) (Nacalai Tesque, Kyoto, Japan) was used with a 50 mM ammonium acetate solution (pH 8.5) as the electrolyte to analyze anionic metabolites. Methanol/5 mM ammonium acetate (50% v/v) containing 0.01 μM hexakis(2,2-difluoroethoxy)phosphazene was delivered as the sheath liquid at 10 μL/min. ESI-TOFMS was carried out in negative ion mode, and the capillary voltage was set to 3.5 kV. Automatic recalibration of each acquired spectrum was achieved using the masses of the reference standards ([^{13}C isotopic ion of deprotonated acetate dimer ($2CH_3COOH-H)]^-$, *m/z* 120.0384) and ([hexakis(2,2-difluoroethoxy)phosphazene +deprotonated acetate ($CH_3COOH-H)]^-$, *m/z* 680.0355). D-Camphor-10-sulfonic acid was used as the internal standards for anion analysis. The other conditions were identical to those described previously (Soga et al., 2009). The acquired raw data were analyzed using our proprietary software (Sugimoto et al., 2010).

Glycogen Content Assay

Glycogen content assay was performed as previously described with some modifications (Noguchi et al., 2013). Approximately 20 mg of the liver and skeletal muscle was digested with 1.2 mL of 30% (w/v) potassium hydroxide solution for 1 hour at 95°C and neutralized with 61.2 μL of glacial acetic acid. The concentration of total protein of tissue digest was determined by BCA assay and adjusted to 1 μg protein/μL. Glycogen was extracted from the liver or skeletal muscle digest with Bligh and Dyer method to remove lipids. The tissue digest (50 μL) was mixed with 120 μL of ice-cold methanol, 50 μL of chloroform, 10 μL of 1% (w/v) linear polyacrylamide, and 70 μL of water. After incubation on ice for 30 min, the mixture was centrifuged at 12,000 × *g* to remove the aqueous layer. The glycogen was precipitated by the addition of 200 μL of methanol, separated by centrifugation at 12,000 × *g* for 30 min at 4ºC, washed with ice-cold 80% (v/v) methanol and dried thoroughly. The obtained glycogen pellets were suspended in 20 μL of 0.1 mg/mL amyloglucosidase (Sigma-Aldrich) in 50 mM sodium acetate buffer and incubated for 2 hours at 55ºC to digest glycogen.

According to the manufacturer's instruction, the glycogen-derived glucose concentration was determined using the Amplex Red Glucose/Glucose Oxidase Assay kit glucose assay (Thermo Fisher Scientific).

Lipidomic Analysis

The lipidomic profiling of the liver and skeletal muscle was performed by Metabolon, Inc. Lipids were extracted from samples using dichloromethane and methanol in a modified Bligh-Dyer extraction in the presence of internal standards with the lower, organic, phase being used for analysis. The extracts were concentrated under nitrogen and reconstituted in 0.25 mL of dichloromethane:methanol (50:50) containing 10 mM ammonium acetate. The extracts were placed in vials for infusion-MS analyses, performed on a SelexION equipped Sciex 5500 QTRAP using both positive and negative mode electrospray. Each sample was subjected to two analyses, with IMS-MS conditions optimized for lipid classes monitored in each analysis. The 5500 QTRAP was operated in MRM mode to monitor the transitions for over 1,100 lipids from up to 14 lipid classes. Individual lipid species were quantified based on the ratio of the signal intensity for target compounds to the signal intensity for an assigned internal standard of known concentration. Four-teen lipid class concentrations were calculated from the sum of all molecular species within a class.

Identification of Differentially Expressed Molecules between Wild-type Mice and *ob*/*ob* Mice

Molecules in the liver, skeletal muscle, and the blood, that were detected in less than 70% of replicates in either WT or *ob*/*ob* mice were removed from the analysis. The differences in the amounts of molecules between WT and *ob*/*ob* mice were determined by a statistical test using the following procedure. The significance of differences was tested by two-tailed Welch's t-test for each phosphorylation (ratio of phosphorylation to the total amount of molecule), protein expression, polar metabolite amount, and lipid amount, and by the edgeR package (version 3.29.1) of the R language (version 3.6.1) with default parameters for each gene expression. Molecules that showed a q value less than 0.1 for phosphorylation, protein expression, gene expression, polar metabolite amount, and lipid amount were defined as differentially expressed molecules in amount between

WT and *ob*/*ob* mice. The q values were calculated by Storey's procedure for gene expression, protein expression, and polar metabolite. The q values were calculated by Benjamini–Hochberg procedure for lipid and phosphorylation because of the small numbers of molecules (less than 100). The ratio of phosphorylation to the total amount of molecule was used to calculate fold change for all molecules.

Prediction of Transcription Factor Binding Motif and Inference of Differential Regulations between Differentially Regulated Transcription Factors and Differentially Expressed Genes

The flanking regions around the transcription start site of each DEG were extracted from GRCm38/mm10 (Ensembl, release 97) using Ensembl BioMart (Kinsella et al., 2011). The region from -1000 bp to +1000 bp of the major transcription start site was defined as the flanking region. The transcription factor (TF) binding motifs in each flanking region were predicted using TRANSFAC Pro, a TF binding motif database, and Match, a TF binding motif prediction tool (Matys et al., 2006; Kel et al., 2003). The threshold for each motif prediction was set using extended vertebrate_non_redundant_min_FP.prf, a TRANSFAC Pro parameter. Because some of the TFs known to involve the metabolic regulations of the liver or skeletal muscle are not included in this parameter set, we extracted the TF binding motifs of Pparα, Pparγ, Foxo1, Srebp1, and Chrebp1 from vertebrate_non_redundant.prf, and added these motifs and their parameters to vertebrate_non_redundant_min_FP.prf.

For the estimation of differential regulations between the regulating differentially regulated TFs (DRTFs) and the regulated DEGs, TF motif enrichment analysis was performed. The enrichment of the TF binding motif in the flanking regions of DEGs was determined by one-tailed Fisher's exact test. TF binding motifs with q value less than 0.05 were defined as significantly enriched. The q values were calculated by Benjamini–Hochberg procedure. The genes detected in more than 70% of the replicates in WT mice and *ob*/*ob* mice were used as a background. Of the TFs corresponding to enriched TF motifs, we identified those included in the DEGs as the differentially expressed TFs (DETFs) or in the DPPs as the differentially phosphorylated TFs (DPTFs), and defined them as the DRTFs. The differential regulations from the DRTFs to the DEGs were

determined based on the relationship between the TFs and the expression of the DEGs inferred from TF motif enrichment analysis. If a TF binding motif of DRTF was enriched in the flanking regions of the DEGs, the differential regulations between the DRTFs and the DEGs were inferred.

Construction of the Trans-Omic Network for Differentially Regulated Metabolic Reactions in Liver and Skeletal Muscle

The trans-omic networks for differentially regulated metabolic reactions in liver and skeletal muscle consisted of differentially expressed molecules in six omic layers — Insulin Signal, TF, Enzyme mRNA, Enzyme Protein, Metabolic Reaction, and Metabolite layers— and the differential regulations connecting the differentially expressed molecules across each omic layer (see Figure 4A). The Insulin Signal layer is the insulin signaling pathway constructed in our previous study (Kawata et al., 2018; Kokaji et al., 2020). The Insulin Signal layer included insulin signaling molecules that we measured by Western blotting. The TF layer consisted of all TFs corresponding to inferred TF motifs (Table S6). The Enzyme mRNA layer and Enzyme Protein layer consisted of the expression of genes and proteins of all metabolic enzymes in the pathways in Metabolism obtained from the KEGG database (Kanehisa et al., 2017). The Metabolic Reaction layer consisted of the metabolic reactions (based on EC number) corresponding to the metabolic enzymes. The Metabolite layer consisted of all metabolites detected by CE-MS.

Each omic layer of the trans-omic network included the corresponding differentially expressed molecules. The Insulin Signal layer included insulin signaling molecules in differentially phosphorylated proteins (DPPs) (Figure 2A). The TF layer included DRTFs, which are TFs corresponding to inferred TF motifs included in the DEGs as the DETFs (Figure 2F) or those included in the DPPs as the DPTFs (Figure 2A). To avoid overestimation, the TFs with downstream genes that were not enriched in increased or decreased genes in *ob*/*ob* mice were excluded from DRTFs. The Enzyme mRNA layer included metabolic enzymes encoded by DEGs (Figure 2B). The Enzyme Protein layer included the differentially expressed metabolic enzymes (DEMEs), which were defined as metabolic enzymes among the differentially expressed proteins (DEPs)

(Figure 2C). The Metabolic Reaction layer included differentially regulated metabolic reactions, which were defined as metabolic reactions regulated by the differentially expressed metabolites (DEMs), the DEMEs, or both. The Metabolite layer included the DEMs (Figures 2D).

To determine differential regulations between the regulating differentially expressed molecules and the regulated differentially expressed molecules, we used a process that we have used previously (Kokaji et al., 2020). The differential regulations were determined using the changed directions (increased or decreased) of the regulating differentially expressed molecule, and the types of the regulatory directions (activator or inhibitor) of the regulating differentially expressed molecule (see also Figure S5 lower table). We defined the activating regulations in *ob*/*ob* mice when the regulating molecule increased in *ob*/*ob* mice was an activator or that decreased in *ob*/*ob* mice was an inhibitor and the regulated molecule increased in *ob*/*ob* mice. On the other hand, we defined the inhibiting regulations in *ob*/*ob* mice when the regulating molecule decreased in *ob*/*ob* mice was an activator or that increased in *ob*/*ob* mice was an inhibitor and the regulated molecule decreased in *ob*/*ob* mice.

The differential regulations in the trans-omic network from the Insulin Signal layer to the TF layer were determined based on the kinase-substrate relationship in the insulin signaling pathway constructed in our previous phosphoproteomic study (Kawata et al., 2019). The insulin signaling pathway comprises several signaling pathways in the KEGG database (Kanehisa et al., 2017). The differential regulations in the trans-omic network from the TF layer to the Enzyme mRNA layer were determined based on the relationship between DRTFs and the expression of DEGs inferred from TF motif enrichment analysis. According to the KEGG database, the effects of the phosphorylation of DRTFs on the types of regulations were defined. The differential regulations in the trans-omic network from the Enzyme mRNA layer to the Enzyme Protein layer were determined based on the correspondence between the DEGs encoding metabolic enzymes and the DEMEs. The differential regulations in the trans-omic network from the Enzyme Protein layer to the Metabolic Reaction layer were determined by regulation of metabolic reactions by the corresponding metabolic enzymes according to the KEGG database (Kanehisa et al., 2017). The differential regulations in the trans-omic network from the

Metabolite layer to the Metabolic Reaction layer were of two types: regulation by allosteric regulator among the DEMs (allosteric regulation) and regulation by the substrate or product among the DEMs. Allosteric regulations were determined by the regulation of metabolic reactions by allosteric regulators according to the BRENDA database (Jeske et al., 2019). The allosteric regulations reported for mammals (Bos taurus, Felis catus, Homo sapiens, “Macaca,” “Mammalia,” “Monkey,” Mus booduga, Mus musculus, Rattus norvegicus, Rattus rattus, Rattus sp., Sus scrofa, “dolphin,” and “hamster”) were used. According to the KEGG database, regulations by substrate or product were determined by the regulation of metabolic reaction by its substrate or product (Kanehisa et al., 2017). Because the reversibility of metabolic reactions was not determined, metabolic reactions were presumed to be regulated by both the substrate and product.

Implementation

Statistical tests and trans-omic network analysis were performed using MATLAB 2019a (The Mathworks Inc.). Visualization of trans-omic network in Graph Modeling Language (GML) formats was performed using Python 2.7 and VANTED (Junker et al., 2006).

SUPLEMENTAL REFERENCES

Chiara, F.D., Heebøll, S., Marrone, G., Montoliu, C., Hamilton-Dutoit, S., Ferrandez, A., Andreola, F., Rombouts, K., Grønbæk, H., Felipo, V., et al. (2018). Urea cycle dysregulation in non-alcoholic fatty liver disease. Journal of Hepatology *69*, 905–915.

Cunningham, F., Amode, M.R., Barrell, D., Beal, K., Billis, K., Brent, S., Carvalho-Silva, D., Clapham, P., Coates, G., Fitzgerald, S., et al. (2015). Ensembl 2015. Nucleic Acids Res *43*, D662–D669.

Dobin, A., Davis, C.A., Schlesinger, F., Drenkow, J., Zaleski, C., Jha, S., Batut, P., Chaisson, M., and Gingeras, T.R. (2013). STAR: ultrafast universal RNA-seq aligner. Bioinformatics *29*, 15–21.

Flicek, P., Amode, M.R., Barrell, D., Beal, K., Billis, K., Brent, S., Carvalho-Silva, D., Clapham, P., Coates, G., Fitzgerald, S., et al. (2014). Ensembl 2014. Nucleic Acids Res *42*, D749–D755.

Kinsella, R.J., Kähäri, A., Haider, S., Zamora, J., Proctor, G., Spudich, G., Almeida-King, J., Staines, D., Derwent, P., Kerhornou, A., et al. (2011). Ensembl BioMarts: a hub for data retrieval across taxonomic space. Database (Oxford) *2011*.

Li, B., and Dewey, C.N. (2011). RSEM: accurate transcript quantification from RNA-Seq data with or without a reference genome. BMC Bioinformatics *12*, 323.

Matsumoto, K., Suzuki, A., Wakaguri, H., Sugano, S., and Suzuki, Y. (2014). Construction of mate pair full-length cDNAs libraries and characterization of transcriptional start sites and termination sites. Nucleic Acids Res *42*, e125–e125.

Newgard, C.B., An, J., Bain, J.R., Muehlbauer, M.J., Stevens, R.D., Lien, L.F., Haqq, A.M., Shah, S.H., Arlotto, M., Slentz, C.A., et al. (2009). A Branched-Chain Amino Acid-Related Metabolic Signature that Differentiates Obese and Lean Humans and Contributes to Insulin Resistance. Cell Metabolism *9*, 311–326.

Noguchi, R., Kubota, H., Yugi, K., Toyoshima, Y., Komori, Y., Soga, T., and Kuroda, S. (2013). The selective control of glycolysis, gluconeogenesis and glycogenesis by temporal insulin patterns. Molecular Systems Biology *9*, 664.

Rappsilber, J., Mann, M., and Ishihama, Y. (2007). Protocol for micro-purification, enrichment, pre-fractionation and storage of peptides for proteomics using StageTips. Nature Protocols *2*, 1896–1906.

Rodríguez-Suárez, E., Duce, A.M., Caballería, J., Arrieta, F.M., Fernández, E., Gómara, C., Alkorta, N., Ariz, U., Martínez-Chantar, M.L., Lu, S.C., et al. (2010). Non-alcoholic fatty liver disease proteomics. PROTEOMICS – Clinical Applications *4*, 362–371.

Schindelin, J., Arganda-Carreras, I., Frise, E., Kaynig, V., Longair, M., Pietzsch, T., Preibisch, S., Rueden, C., Saalfeld, S., Schmid, B., et al. (2012). Fiji: an open-source platform for biological-image analysis. Nature Methods *9*, 676–682.

Soga, T., and Heiger, D.N. (2000). Amino Acid Analysis by Capillary Electrophoresis Electrospray Ionization Mass Spectrometry. Anal. Chem. *72*, 1236–1241.

Soga, T., Baran, R., Suematsu, M., Ueno, Y., Ikeda, S., Sakurakawa, T., Kakazu, Y., Ishikawa, T., Robert, M., Nishioka, T., et al. (2006). Differential Metabolomics Reveals Ophthalmic Acid as an Oxidative Stress Biomarker Indicating Hepatic Glutathione Consumption. J. Biol. Chem. *281*, 16768–16776.

Soga, T., Igarashi, K., Ito, C., Mizobuchi, K., Zimmermann, H.-P., and Tomita, M. (2009). Metabolomic Profiling of Anionic Metabolites by Capillary Electrophoresis Mass Spectrometry. Anal. Chem. *81*, 6165–6174.

Sugimoto, M., Wong, D.T., Hirayama, A., Soga, T., and Tomita, M. (2010). Capillary electrophoresis mass spectrometry-based saliva metabolomics identified oral, breast and pancreatic cancer-specific profiles. Metabolomics *6*, 78–95.

White, P.J., and Newgard, C.B. (2019). Branched-chain amino acids in disease. Science *363*, 582–583.